

Copyright
by
Timothy William Haller
2021

The Dissertation Committee for Timothy William Haller
certifies that this is the approved version of the following dissertation:

**Thermometry in High Pressure Gases using Spontaneous
Raman Scattering**

Committee:

Philip Varghese, Supervisor

Noel Clemens

Matthew Hall

Sean Kearney

Laxminarayan Raja

**Thermometry in High Pressure Gases using Spontaneous
Raman Scattering**

by

Timothy William Haller

DISSERTATION

Presented to the Faculty of the Graduate School of
The University of Texas at Austin
in Partial Fulfillment
of the Requirements
for the Degree of

DOCTOR OF PHILOSOPHY

THE UNIVERSITY OF TEXAS AT AUSTIN

May 2021

To my parents Dr. Christine and Doug Haller,
and my fiancée Anna Bennett.

Acknowledgments

There are many to thank for helping me on my journey for this PhD. I would first like to thank my advisor, Prof. Philip Varghese. He has been teaching me since my first day of graduate school and has guided me along this journey, providing invaluable advice, suggestions, and support. Prof. Philip Varghese taught me the importance of attention to detail and critical thinking regarding experimental design, data analysis, and technical writing. I am very grateful for his instruction and guidance. I would like to thank Prof. Noel Clemens for his insight and advice regarding my experiments and for serving on my committee. I would also like to thank Prof. Matthew Hall, Dr. Sean Kearney, and Prof. Laxminarayan Raja for their time and effort spent serving on my dissertation committee.

I am grateful to the graduate students and post-docs who I had the good fortune of working alongside and interacting with regularly: Dr. Chris Combs, Dr. Dominik Ebi, Dr. Benton Greene, Dr. Kyle Higdon, Dr. William Hoey, Dr. Utsav KC, Dr. Yasvanth Poondla, Dr. Rakesh Ranjan, Dr. Heath Reising, Dr. Leon Vanstone., and Dr. Stephen Voelkel. Each of them assisted me in some capacity, whether brainstorming solutions to technical problems, navigating the PhD process, or commiserating on the challenges of being a graduate student. I must give a special thanks to Dr. Heath Reising, who showed me how to set up, align, conduct, and analyze a Raman spectroscopy experiment.

I am grateful for the assistance from the staff of the Department of Aerospace Engineering and Engineering Mechanics. Dr. Jeremy Jagodzinski was very helpful in

setting up the experiment and providing input on technical challenges and safety issues. I thank Geetha Rajagopal for promptly placing purchase orders, communicating with suppliers, keeping me informed and helping me however possible. I appreciate the assistance of Pablo Cortez, Jeffrey Ramsey, and Scott Messec who helped me with many aspects of my experiments.

I am thankful to Sandia National Laboratories for funding from grant #1888931 under the Academic Alliance Program. I would also like to thank the Cockrell School of Engineering and Mr. and Mrs. Jack and Maxine Zarrow for financial support through the Jack and Maxine Zarrow Endowed Graduate Fellowship in Engineering.

I thank my family for their support and love throughout my whole graduate school experience. Finally, I thank my fiancée Anna Bennett for everything she did to help me reach this point. She provided never-ending support by always being there with a sympathetic ear as well as offering superb scientific and engineering input. I truly could not have done this without her.

Thermometry in High Pressure Gases using Spontaneous Raman Scattering

Timothy William Haller, Ph.D.
The University of Texas at Austin, 2021

Supervisor: Philip Varghese

Spontaneous Raman scattering from nitrogen is studied in high pressure gases. Collision frequency increases with increasing gas density, causing spectral lines to broaden due to pressure broadening and mix when the lines are strongly overlapped. Because spontaneous Raman thermometry is accomplished by fitting a simulated spectrum to an experimental spectrum, spectral models that neglect these collision-induced effects will lead to erroneous temperature inference. This work investigates the influence of high density on ro-vibrational spontaneous Raman scattering, which must be understood to obtain accurate thermometry in high pressure gases. The temperature profile through a flame front was measured at 1 atm, 3 atm, and 5 atm using spontaneous Raman scattering from nitrogen. The pressure broadening was measured for the anisotropic tensor component of spontaneous Raman scattering from room temperature nitrogen over the pressure range of 10 atm to 70 atm for three gas compositions: pure nitrogen, air, and nitrogen in argon. The unmixed line model was found to give good fits to the O and S branches for all pressures, which indicates that line mixing effects are not significant in the O and S branches over this pressure range.

Using indirect experimental evidence, line mixing effects in the anisotropic component of the Q branch were inferred to be below the threshold set by the experimental spectral resolution at pressures up to 70 atm at room temperature. Assuming that the anisotropic Q branch lines mix like the isotropic lines was found to result in a small systematic error in the inferred temperature at flame temperatures, with the error increasing slowly with pressure. The bias can be removed by modeling the anisotropic spectrum separately from the isotropic spectrum. Line mixing effects should be included in the modeling of the isotropic component of the Raman spectrum, but can probably be neglected in the anisotropic component of the ro-vibrational spontaneous Raman spectrum of nitrogen.

Table of Contents

List of Tables	xi
List of Figures	xii
Chapter 1. Introduction	1
1.1 Motivation	2
1.2 Literature Survey	6
1.3 Dissertation Overview	7
Chapter 2. Background Theory	9
2.1 Line Mixing	19
Chapter 3. Elevated Pressure Thermometry	27
3.1 Experimental Setup	28
3.2 Elevated Pressure Results	33
3.3 Flame Front Temperature Profile	40
3.4 Temperature Measurement Verification	43
3.4.1 Experimental Setup	44
3.4.2 Temperature Measurement Results	46
Chapter 4. Measurements of Pressure Broadening in the Anisotropic Tensor Component	50
4.1 Experimental Setup	51
4.2 Procedure	55
4.2.1 Experimental	55
4.2.2 Data Analysis	57
4.3 Pressure Broadening in the Anisotropic Component	60

Chapter 5. High Pressure Modeling of the Q Branch	74
5.1 Line Mixing in the Q Branch	75
5.1.1 Isotropic Simulations	76
5.1.2 Anisotropic Q branch	79
5.2 Effect on High Pressure Thermometry	82
5.2.1 Consequences for Elevated Pressure Thermometry	87
Chapter 6. Conclusions	93
6.1 Future Work	96
Appendices	98
Appendix A. Calculation of Line Mixed Raman Spectra	99
Appendix B. Standard Operating Procedure	103
B.1 Purpose	103
B.2 Personnel	103
B.3 Hazards	104
B.3.1 Laser	104
B.3.2 Electrical	104
B.3.3 Pressure	105
B.4 Hazard Controls	105
B.4.1 Laser	105
B.4.2 Electrical	106
B.4.3 Pressure	107
B.5 Normal Operation	108

List of Tables

2.1	Spectroscopic notation for rotational transitions.	10
2.2	Space-averages of polarizability components for ro-vibrational Stokes scattering from diatomic molecules [1].	13
2.3	Molecular constants for nitrogen in cm^{-1} [81, 82].	17
2.4	MEG model parameters from Lavorel et al. [68].	24
2.5	Integrands for matrix cross sections for anisotropic Raman scattering [73].	25
3.1	Summary of experimental conditions and calculated equivalence ratios.	46
3.2	Summary of temperature verification experimental results.	47
4.1	Experimental nitrogen anisotropic line broadening coefficients, FWHM ($\text{cm}^{-1}/\text{atm}$)	70

List of Figures

2.1	Sketch of the coordinate system for (a) side scattering and (b) forward scattering. The $\hat{\mathbf{S}}$ vector indicates the scattering direction.	14
3.1	Photograph of the elevated pressure combustion facility and the Raman scattering experimental setup.	29
3.2	Photograph of the laser in the elevated pressure combustion chamber.	30
3.3	Diagram of the f/1.8 imaging spectrograph from Kaiser Optical Systems collecting spontaneous Raman signal in a side-scattering configuration.	32
3.4	Photograph of the flame in the combustion chamber at 1 atm.	33
3.5	(a) Schematic showing the burner translation direction and measurement region, and (b) photographs of the burner assembly	34
3.6	Comparison between nitrogen Stokes Raman spectra at 1 atm and 5 atm at room temperature. (a) Recorded spectra in the region of the Q branch scaled to unit maximum intensity. (b) Spectra over an extended frequency range with vertical scale magnified to show the rotational structure from O and S branches of the $^{14}\text{N}_2$ isotopologue and the Q branch of the $^{15}\text{N}^{14}\text{N}$ isotopologue.	36
3.7	Comparison between nitrogen Stokes Raman spectra at 1 atm and 5 atm at flame temperature. (a) Recorded spectra scaled to unit maximum intensity showing the multiple vibrational modes populated in the Q branch at flame temperature as well as the Raman signal from CO. (b) Spectra in the region of the S branch with vertical scale magnified to show the rotational structure of $^{14}\text{N}_2$	37
3.8	Temperature fit to nitrogen Raman spectrum recorded at 1 atm, resulting in an inferred temperature of 1850 K. The right panel shows a magnified vertical scale to show the rotational structure of $^{14}\text{N}_2$	38
3.9	Temperature fit to nitrogen Raman spectrum recorded at 5 atm, resulting in an inferred temperature of 2008 K. The right panel shows a magnified vertical scale to show the rotational structure of $^{14}\text{N}_2$	39
3.10	Scanned temperature profiles at three pressures: 1 atm, 3 atm, and 5 atm	41
3.11	Photograph of the verification burner with a lean flame and the setup of the spontaneous Raman scattering experiment.	45
3.12	Temperature versus equivalence ratio for the verification burner	48
4.1	Isometric view of the pressure chamber.	52

4.2	Piping and Instrumentation Diagram. 1, Gas Cylinder; 2, Needle Valve; 3, Solenoid Control Valve; 4, Check Valve; 5, Pressure Chamber; 6, Pressure Transducer; 7, Pneumatic Control Valve; 8, Ball Valve; 9, Pressure Relief Valve.	53
4.3	Schematic diagram of the forward scattering experiment.	56
4.4	Comparison between nitrogen Raman spectra recorded in pure nitrogen at 10 atm and 70.1 atm. (a) Recorded spectra in the Q branch region scaled to unit maximum intensity. (b) Spectra over an extended frequency range with vertical scale magnified 100 times to show rotational structure from O and S branches of the dominant $^{14}\text{N}_2$ isotopologue and the Q branch of the $^{15}\text{N}^{14}\text{N}$ isotopologue.	58
4.5	Fits to anisotropic component of nitrogen Raman spectra recorded in 100 % nitrogen.	62
4.6	(a) The root mean square of the residual errors for the fits to anisotropic Raman spectra of nitrogen (left axis) and the mean signal-to-noise ratio (right axis) plotted as a function of the total pressure. (b) Same data plotted as a function of nitrogen partial pressure. The symbols shown in the legend also apply to (a)	63
4.7	Lorentzian widths obtained from fits to anisotropic nitrogen Raman spectra recorded in (a) 100 % N_2 , (b) 100 % air, and (c) 20 % N_2 + 80 % Ar. A linear regression is applied to the results for every M , with a common intercept at 0 atm. A vertical dashed line bounds the minimum experiment pressure used for the linear regression. The intercept represents the instrument contribution to the Lorentzian width, and it is compared to the Lorentzian width obtained from fits to neon lamp spectral lines.	65
4.8	Fits to 6 neon spectral lines recorded using a neon lamp. These fits were used to determine the instrument lineshape parameters.	67
4.9	(a) Comparison between experimental nitrogen self-broadening line broadening coefficients from anisotropic linewidth fits and theoretical MEG model calculations and (b) a comparison of experimental anisotropic line broadening coefficients for nitrogen in nitrogen, nitrogen in air, and nitrogen in argon. The black line in (a) represents the estimated nitrogen self-broadening anisotropic line broadening coefficients at every M value, which is the mean ratio between the experimental line broadening coefficients and the MEG model coefficients, applied to every M value.	69
4.10	Comparison of anisotropic ro-vibrational self-broadening coefficients for N_2 measured in this work with S branch linewidths inferred from time domain measurements using hybrid fs/ps of purely rotational transition using RCARS from Miller et al. and Kliewer et al. [77, 94].	72
5.1	Simulations of the isotropic component of spontaneous Raman scattering from nitrogen at 300 K without line mixing.	77

5.2	Simulations of the isotropic component of spontaneous Raman scattering from nitrogen at 300 K with line mixing.	78
5.3	Simulations of the isotropic component of spontaneous Raman scattering from nitrogen at 300 K and 70 atm with and without line mixing.	80
5.4	Comparison between experimental isotropic spectra and a mixed isotropic simulation generated using the MEG model at (a,b) 37.1 atm and (c,d) 70.1 atmosphere. The vertical scale is expanded by 100 in (b,d). . . .	81
5.5	Simulated high temperature and pressure (1800 K, 70 atm) Raman spectrum of nitrogen with anisotropic contribution unmixed and the isotropic Q branch mixed. In (c,d) a small amount of shot noise and random readout noise has been added to the simulated experimental spectrum. The simulated spectrum is compared to a model spectrum which assumes that the anisotropic Q branch lines are mixed exactly like the isotropic lines. The dashed vertical lines indicate the frequency range over which the sum of the squared residual is used to infer the best match between simulated data and a model spectrum.	85
5.6	Variation of the sum of the squared residual error with temperature when using a library of model spectra that assume the anisotropic Q branch lines broaden and mix like the isotropic Q branch lines. (a) Without noise added to the simulated spectrum, corresponding to Figures 5.5a and 5.5b. (b) With noise added to the simulated spectrum, corresponding to Figures 5.5c and 5.5d.	86
5.7	Simulations of the isotropic component of the nitrogen spontaneous Raman spectrum at 5 atm and 2008 K, with and without line mixing. The instrument lineshape function from the experimental Raman spectrum recorded in a 5 atm flame has been applied to these simulations. Because of this relatively broad instrument function, differences between these simulations are nearly undetectable.	90
5.8	Temperature fit to nitrogen Raman spectrum recorded in a partially premixed flame at 5 atm, resulting in an inferred temperature of 2008 K. The model used for this fit did not include line mixing and applied the same lineshape function to every spectral line.	91

Chapter 1

Introduction

Light propagating through a volume of space will be absorbed, scattered or transmitted by the atoms or molecules present. Absorption may occur if the energy of the incident photons matches the separation of two energy levels of the atoms or molecules. Scattered light that has the same wavelength as the incident light (elastic scattering) is called Rayleigh scattering (when the scattering particles are much smaller than the wavelength of light), which is named after Lord Rayleigh who first formulated a classical theory for this phenomenon in 1871 [1]. Scattered light that is shifted in wavelength from the incident light (inelastic scattering) is called Raman scattering, which is named after C. V. Raman who first experimentally observed inelastic scattering (aided by his student K. S. Krishnan) and published spectra showing this effect in 1928 [1]. The 1930 Nobel Prize in Physics was awarded to C. V. Raman for "his work on the scattering of light and for the discovery of the effect named after him."

The wavelength shift in Raman scattering is established by the rotational, vibrational, and electronic properties of the scattering molecules, which offers powerful diagnostic potential. However, Raman scattering is very weak. Generally Raman scattering intensity is 1000 times weaker than Rayleigh scattering intensity, and Rayleigh scattering is 1000 times weaker than the incident light intensity [2]. The development of high power lasers and sensitive photodetectors has unlocked much of

this diagnostic potential.

This chapter discusses the motivation for this research work, which investigates the feasibility of spontaneous Raman thermometry in gas turbine engine applications and the effects of high pressure on this diagnostic technique. A literature survey and an overview of this dissertation are also included in this chapter.

1.1 Motivation

In gas turbine engines, the turbine inlet temperature is an important design parameter. Combustion products must be diluted and cooled so that the product mixture exiting the combustor and entering the turbine does not exceed the turbine inlet temperature [3]. Increasing the turbine inlet temperature increases the thrust (or power) output of a gas turbine engine [4, 5]. Currently, gas turbines operate with inlet turbine temperatures that are significantly higher than the melting point of turbine blade materials [6]. This is accomplished through film cooling, in which relatively cool air extracted from the compressor is injected from inside turbine blades to the blade surfaces, forming a coolant film that protects the blades [6, 7, 8, 9]. Cooling air may also be used to internally cool the turbine blades [6]. However, bleeding this cooling air from the compressor results in a loss of power and a slight decrease in efficiency, though these losses are much smaller than the gains from the increased turbine inlet temperature [3, 5]. Therefore, it is important to optimize the turbine cooling to maximize the engine's performance.

The temperature distribution in the gas exiting the combustion chamber and entering the turbine is not perfectly uniform, varying by up to $\pm 10\%$ of the mean value in aircraft gas turbine engines [5]. The flowfield in this region of the engine is

turbulent and complex [10, 11]. Local hot spots present in the post-combustion flow reduce turbine blade lifetime and create risk for blade failure. If the predicted blade metal temperature is off by just 30 K, the blade lifetime may be reduced by half [6, 9]. Therefore, it is important to reliably characterize gas temperature in this region of the engine. Measuring the turbine blade surface temperature is possible using optical pyrometry [12] or pressure sensitive paint [13, 14]. Blade temperature measurements do provide valuable insight into the effectiveness of the film cooling, but they do not directly measure the gas temperature entering the turbine or detect hot spots in the post-combustion flow. The motivation to maximize turbine inlet temperatures necessitates accurate measurements of the post-combustion, pre-turbine temperature profile to prevent turbine blade degradation and failure.

The post-combustor, pre-turbine region of a gas turbine engine is a challenging environment to accurately measure the gas temperature. Thin-filament pyrometry has been utilized for this temperature measurement in an atmospheric combustion rig simulating a model aero-engine combustor [15]. While thin-filament pyrometry is simple and cost-effective, this technique does have several sources of measurement error and uncertainty, including the insertion of a probe into the flow, the aging behavior of the fibers, and the radiation correction needed to account for the temperature difference between the gas temperature and fiber surface temperature [16]. In contrast, laser diagnostics can provide nonintrusive, remote measurements of temperature with high spatial resolution [17]. Reliable temperature measurements in harsh environments are attainable using laser diagnostics, including laser absorption spectroscopy [18, 19, 20], laser induced fluorescence (LIF) or planar laser induced fluorescence (PLIF) [21, 22, 23], thermographic phosphors [24, 25, 26], Rayleigh scattering [27, 28, 29, 30], spontaneous Raman scattering [31, 32], and coherent anti-Stokes Raman scattering

(CARS) [33, 34, 35, 36, 37, 38, 39, 40].

Many of these techniques have been implemented in gas turbine model combustors [41, 42, 43, 44, 45, 46, 47, 48]. However, those studies investigated the gas turbine combustor and the accompanying combustion physics. To the best of our knowledge very few of these laser diagnostic techniques have been used to measure the post-combustor, pre-turbine temperature in a gas turbine engine test rig. Recently, Scherman et al. [49] used spontaneous rotational Raman spectroscopy to measure temperature in a test facility consisting of a combustor simulator attached to a high pressure turbine, though the maximum pressure inside the test rig for these experiments was 1.5 bar [49], far lower than pressures typically found in gas turbine engines [3, 4, 5]. Nonetheless, this study demonstrates that laser diagnostics are capable of probing the post-combustor, pre-turbine region of a gas turbine engine.

Each of these laser diagnostics has drawbacks that may limit its usefulness and feasibility for pre-turbine gas thermometry. For example, absorption is a path integrated method which is not ideal for detecting local hot-spots; PLIF requires quenching calibrations that add uncertainties; thermographic phosphors have a limited range of temperature sensitivity; Rayleigh scattering requires knowledge of the effective Rayleigh cross-section of the gas mixture; spontaneous Raman scattering suffers from weak signal strength; and CARS overlaps multiple laser beams, which may be challenging with restricted optical access and significant beam steering. Additionally, the high pressure environment of gas turbine engines complicates all spectroscopic techniques because as the gas density increases, the collisional frequency increases, and spectral lines broaden, shift, and mix [50]. Despite these challenges, the importance of pre-turbine temperature measurements merits thorough investi-

gations into the feasibility of laser-based thermometry in this region of gas turbine engines.

Spontaneous Raman scattering is the inelastic scattering of light from molecules, which enables one to make quantitative measurements of species concentration and temperature in complex reacting flow environments [17]. Raman scattering offers all the advantages of laser diagnostic techniques: non-intrusive, in-situ, and high spatial resolution in hostile conditions. Because the spontaneous Raman scattering signal is linearly proportional to laser power it simplifies data analysis. Additionally, it does not need corrections for collisional quenching. Therefore, Raman scattering measurements are direct measurements of temperature or species concentration, which reduces the associated uncertainty. Nitrogen is a well-suited as a probe molecule for this application because nitrogen is abundant in air-breathing gas turbine engines. It is often present in combustion applications at high concentrations in both pre-flame and post-flame gases. Therefore, nitrogen serves as a good indicator of gas temperature. Spontaneous Raman scattering from nitrogen is capable of reliably measuring the pre-turbine temperature profile in gas turbine engines.

Two disadvantages of laser diagnostics are the need for optical access and beam-steering effects due to the presence of large density gradients found in high-temperature applications. Spontaneous Raman scattering reduces the influence of these shortcomings by only requiring one beam and one optical port in principle. Note that one optical port is possible only in the near-backscattering configuration. Forward and side scattering require two optical ports.

Unfortunately Raman scattering is very weak. This is the primary downside of spontaneous Raman scattering, making high-speed thermometry challenging and

often limiting this technique to point measurements. To maximize signal collection, a large collection solid angle is always desirable with spontaneous Raman scattering, but this can be prohibited by the window sizes found in high pressure combustion chambers. However, because the spontaneous Raman scattering signal scales linearly with number density, this technique is well-suited for high pressure environments. Multiple-pass cells can be used to increase laser intensity in the measurement volume, increasing the spontaneous Raman signal [51, 52]. High-speed spontaneous Raman thermometry is achievable with pulse-burst lasers [53, 54]. High-speed 2D spontaneous Raman measurements of species concentration is also possible [55]. While these methods to boost the spontaneous Raman signal require expensive equipment and are not necessarily feasible in a gas turbine test rig, they demonstrate that the challenge of weak Raman signal can be overcome.

Spontaneous Raman scattering from nitrogen and the anticipated challenges of using this technique to measure temperature in a gas turbine engine are the subject of this dissertation, focusing in particular on the high pressure environment of this application which complicates the analysis of experimental spectra and may affect the accuracy of spontaneous Raman thermometry. The next section provides a theoretical overview of spontaneous Raman scattering that relates to the work presented in this dissertation.

1.2 Literature Survey

Previous studies have investigated Raman scattering in high pressure gases, including spontaneous Raman [56, 57], stimulated Raman [58, 59, 60], inverse Raman [61], and coherent anti-Stokes Raman scattering (CARS) [62, 63, 64]. The Modified

Exponential Gap (MEG) line mixing model [61, 65], which relies on experimentally determined parameters and line broadening coefficients [66, 67, 68], has been developed for high pressure applications. The non-Markovian energy corrected sudden model has been developed for rotational Raman [69, 70] and compared to measurements in the isotropic Raman Q branch [71]. Theoretical studies indicate that the relaxation cross-sections for polarized isotropic Raman scattering are different than those for depolarized anisotropic Raman scattering [72, 73, 74]. Although the anisotropic tensor component of ro-vibrational spontaneous Raman scattering is much weaker than the isotropic component, high-fidelity simulations that include both components can be utilized for accurate temperature measurements [51] and measurements of thermal non-equilibrium [31, 75]. Spontaneous Raman has been used for temperature measurements in flames at elevated pressure [41] and high pressure [43]. Nitrogen Raman linewidths have been measured using rotational CARS [76, 77], inverse Raman spectroscopy [66], and stimulated Raman spectroscopy [68, 58]. However, to the best of our knowledge, no studies have recorded ro-vibrational spontaneous Raman spectra at high enough densities and with sufficient spectral resolution to measure pressure-broadened linewidths of the anisotropic tensor component or assess the significance of line mixing effects in the anisotropic component as it relates to spontaneous Raman thermometry.

1.3 Dissertation Overview

This dissertation studies the effects of high pressure on ro-vibrational spontaneous Raman scattering and the impact on spontaneous Raman thermometry. Chapter 2 is a summary of the theoretical background. Chapter 3 presents spontaneous Raman experiments in an elevated pressure combustion facility. These experiments

demonstrate spontaneous Raman thermometry in a combustion chamber by measuring the temperature profile through a flame front at pressures up to 5 atm. Chapter 3 also examines the accuracy and precision of this temperature measurement technique at atmospheric pressure. Chapter 4 presents spontaneous Raman spectra measured in room temperature gases up to pressures of 70 atm. These high pressure spectra are used to measure the pressure broadening coefficients of the anisotropic component of the Raman spectrum by fitting the O and S branches. Chapter 5 investigates the modeling of the spontaneous Raman Q branch at high pressure conditions, in particular focusing on whether line mixing effects should be included in the modeling of the anisotropic component of the Q branch. This chapter also presents estimates of the systematic error in the inferred temperature at flame temperatures resulting from the assumption that the anisotropic component of the Q branch mixes identically to the isotropic component. Finally, Chapter 6 discusses the conclusions of this dissertation and provides recommendations for future work.

Chapter 2

Background Theory

This chapter presents theory relevant to the understanding of this dissertation, but this chapter should not be taken as a comprehensive theoretical framework. Linne's book [2] is a good resource for the fundamentals of spectroscopic measurement techniques, including Raman scattering. Long's book [1] provides an in-depth background on the theory of Raman scattering and the history of this technique. Eckbreth's book [17] also discusses Raman scattering and its specific combustion related applications. Hartmann, Boulet, and Robert's book [50] is an exceptional resource for collisional effects in gas phase spectroscopy, detailing theoretical and experimental knowledge on this subject.

The work in this dissertation uses rotational-vibrational Stokes spontaneous Raman scattering. Scattered light that has a lower frequency than the incident light is said to be Stokes shifted, while scattered light with a higher frequency than the incident light is said to be anti-Stokes shifted. The vibrational state will be represented by the vibrational quantum number, v , and the rotational state will be represented by the total angular momentum quantum number, J . This work involves spontaneous Raman scattering exclusively from nitrogen. Because nitrogen exists in a singlet ground electronic state, the total angular momentum is equal to the nuclear angular momentum, so no distinction needs to be made between the total angular momentum quantum number (J) and the nuclear angular momentum quantum number (N).

Therefore, J will be used to designate the rotational state, as is common practice in the literature [52].

For spontaneous Raman scattering, only rotational transitions of $\Delta J = 0, \pm 2$ are allowed. Rotational lines with transitions of $\Delta J = -2$ belong to the O branch, and rotational lines with transitions of $\Delta J = +2$ belong to the S branch. Lines with transitions of $\Delta J = 0$ belong to the Q branch, though for purely rotational Raman scattering ($\Delta v = 0$) this is really just Rayleigh scattering. This notation is summarized in Table 2.1. For completeness, the criteria for P and R branch transitions ($\Delta J \pm 1$) are also included in Table 2.1, but again, these transitions are forbidden in spontaneous Raman scattering [1].

Table 2.1: Spectroscopic notation for rotational transitions.

Branch	O	P	Q	R	S
ΔJ	-2	-1	0	1	2

For the harmonic oscillator approximation, only $\Delta v = \pm 1$ is allowed. For the anharmonic oscillator, overtones, $\Delta v > \pm 1$, are also allowed. However, overtones are often much weaker than the fundamental transition ($\Delta v = \pm 1$) [1], and are neglected in this work. The anharmonicity will also spectrally shift the "hot bands", which are the spectral features (including associated rotational structure) resulting from vibrational transitions of molecules with an initial vibrational state above the lowest vibrational level, e.g. $v' \leftarrow v'' : 2 \leftarrow 1$. The "hot band" terminology comes from the fact that higher vibrational levels are populated as the temperature increases [2].

In the classical description of the scattering process, the oscillating electric

field of incident monochromatic light, \vec{E} , induces a dipole moment, $\vec{\mu}$, according to

$$\vec{\mu} = \vec{\alpha} \cdot \vec{E} \quad (2.1)$$

where $\vec{\alpha}$ is the polarizability tensor of the molecule. The polarizability tensor for a particular normal vibrational mode can be written as a Taylor series expansion with respect to the coordinate of motion, Q , truncating the series to neglect powers of Q higher than 1:

$$\alpha_{ij} = (\alpha_{ij})_0 + \left(\frac{\partial \alpha_{ij}}{\partial Q} \right)_0 Q \quad (2.2)$$

where $(\alpha_{ij})_0$ is called the "equilibrium polarizability tensor" [2]. The "derived polarizability tensor" is the partial derivative in 2.2 defined as

$$\alpha' \equiv \left(\frac{\partial \alpha_{ij}}{\partial Q} \right)_0 \quad (2.3)$$

Assuming that the vibration can be described by simple harmonic motion, then the coordinate of motion can be written as

$$Q = Q_0 \cos \omega_v t \quad (2.4)$$

where ω_v is some natural frequency of the molecule. The incident electric field can also be assumed to be harmonic:

$$\vec{E} = \vec{E}_0 \cos \omega_0 t \quad (2.5)$$

where ω_0 is the frequency of the input light. Combining the previous equations, the induced dipole moment is then given by

$$\vec{\mu} = \vec{\alpha}_0 \cdot \vec{E}_0 \cos \omega_0 t + \frac{Q_0}{2} \vec{\alpha}' \cdot \vec{E}_0 [\cos(\omega_0 - \omega_v) t + \cos(\omega_0 + \omega_v) t] \quad (2.6)$$

The first term on the right hand side of Equation 2.6 represents scattered light at the incident frequency, ω_0 , which is Rayleigh scattering. The second term represents

scattered light at frequencies shifted from the incident frequency by the molecular frequency, ω_v , which is Raman scattering. The scattered light that is Stokes shifted has a lower frequency than the incident light ($\omega_0 - \omega_v$), and the scattered light with a higher frequency ($\omega_0 + \omega_v$) is anti-Stokes shifted.

Long [1] states that the polarizability tensor may be represented by a pair of invariant values: the mean polarizability, a , and the anisotropy, γ , which are written in terms of the polarizability tensor components as:

$$a \equiv \frac{1}{3}(\alpha_{xx} + \alpha_{yy} + \alpha_{zz}) \quad (2.7)$$

$$\gamma^2 \equiv \frac{1}{2} [(\alpha_{xx} - \alpha_{yy})^2 + (\alpha_{yy} - \alpha_{zz})^2 + (\alpha_{zz} - \alpha_{xx})^2 + 6(\alpha_{xy}^2 + \alpha_{yz}^2 + \alpha_{zx}^2)] \quad (2.8)$$

Because gas phase molecules are randomly oriented, the polarizabilities must be averaged over all orientations. The radiant intensity of an oscillating dipole is a function of the square of the induced dipole moment [1], so the space-averages of the squared polarizability components must be calculated. Long [1] gives the space averages of the squared polarizabilities for diatomic molecules written in terms of the invariants:

$$\langle \alpha_{ii}^2 \rangle = \frac{45a^2 + 4\gamma^2}{45} \quad (2.9)$$

$$\langle \alpha_{ij}^2 \rangle = \frac{\gamma^2}{15} \quad (2.10)$$

Note that the polarizability tensor is symmetric ($\alpha_{ij} = \alpha_{ji}$), so the space-averaged squared polarizability tensor is also symmetric [1]:

$$\langle \alpha_{xx}^2 \rangle = \langle \alpha_{yy}^2 \rangle = \langle \alpha_{zz}^2 \rangle = \langle \alpha_{ii}^2 \rangle \quad (2.11)$$

$$\langle \alpha_{yx}^2 \rangle = \langle \alpha_{yz}^2 \rangle = \langle \alpha_{zx}^2 \rangle = \langle \alpha_{ij}^2 \rangle = \langle \alpha_{ji}^2 \rangle \quad (2.12)$$

The polarizability tensor invariants, a and γ , can each be written as a Taylor series expansion similar to Equation 2.2. Doing so gives polarizability equilibrium in-

variant values, a_0 and γ_0 , and polarizability invariant derivatives, a' and γ' . The polarizability equilibrium values lead to Rayleigh scattering and rotational Raman scattering, while the polarizability derivatives lead to vibrational and rotational-vibrational Raman scattering. Table 2.2 lists the expressions for the space-averaged polarizability components for ro-vibrational Stokes Raman scattering [1]. The Placzek-Teller coefficients, $b_{J',J''}$, are algebraic functions of rotational level, and the functions for the Placzek-Teller coefficients are provided by Long [1]. Note that for high-fidelity spontaneous Raman simulations, higher order corrections are needed to include rotation-vibration interaction [78]. The Herman-Wallis factors are used to account for this effect [79].

Table 2.2: Space-averages of polarizability components for ro-vibrational Stokes scattering from diatomic molecules [1].

Branch	Upper state $v'J'$	Lower state $v''J''$	$\langle (\alpha'_{ii})^2_{v',J':v'',J''} \rangle$	$\langle (\alpha'_{ij})^2_{v',J':v'',J''} \rangle$
O	$v + 1, J - 2$	v, J	$\frac{4}{45}b_{J-2,J}(\gamma')^2$	$\frac{1}{15}b_{J-2,J}(\gamma')^2$
Q	$v + 1, J$	v, J	$(a')^2 + \frac{4}{45}b_{J,J}(\gamma')^2$	$\frac{1}{15}b_{J,J}(\gamma')^2$
S	$v + 1, J + 2$	v, J	$\frac{4}{45}b_{J+2,J}(\gamma')^2$	$\frac{1}{15}b_{J+2,J}(\gamma')^2$

The ro-vibrational spontaneous Raman spectrum consists of an isotropic component and an anisotropic component. The isotropic component arises from the mean of the derived polarizability tensor, a' , while the anisotropic component arises from the anisotropy of the polarizability derivative, γ' . The expressions listed in Table 2.2 show that the O and S branches are purely anisotropic; they are only dependent on γ' . However, the Q branch is dependent on both a' and γ' , so the Q branch has an isotropic contribution and an anisotropic contribution. Because a' and γ' have similar magnitudes for nitrogen [79], this indicates that for nitrogen, the Raman signal of the

Q branch is much stronger than the ro-vibrational O and S branches. Theoretically, the isotropic component of the spectrum and the anisotropic component do not interfere or interact, and thus they can be considered separately [73]. Isotropic Raman scattering is strongly polarized, while anisotropic scattering is strongly depolarized. For a vanishingly small collection solid angle in the 90° side scattering configuration, the depolarization ratios of the isotropic component and the anisotropic component are 0 and 0.75 respectively [1].

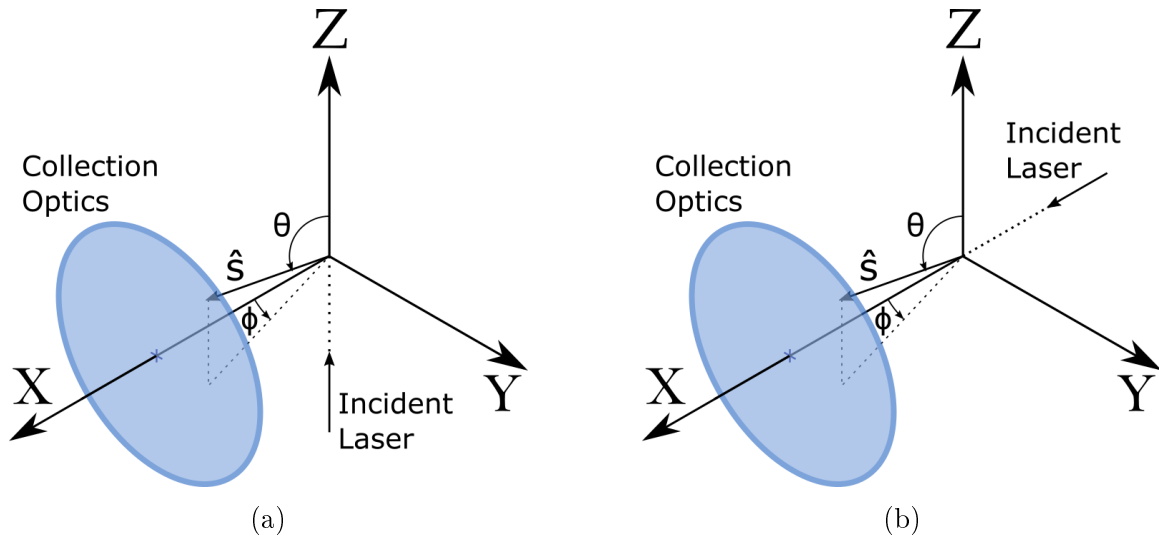


Figure 2.1: Sketch of the coordinate system for (a) side scattering and (b) forward scattering. The \hat{s} vector indicates the scattering direction.

Let us define a space-fixed Cartesian coordinate system with axes of \hat{e}_x , \hat{e}_y , and \hat{e}_z and the scattering volume at the origin. For a 90° side scattering experiment with the incident laser propagating along the \hat{e}_z axis in the $+\hat{e}_z$ direction, the collection optics will be aligned along the $+\hat{e}_x$ axis, as shown in Figure 2.1a. For this geometry with small collection solid angle, the laser beam must be linearly polarized with the electric field aligned in the \hat{e}_y direction to get a signal. The scattering plane is defined as the plane containing the incident radiation and the scattered radiation, so

in this configuration the scattering plane is the x - z plane. The square of the induced dipole moment for scattered light that is polarized parallel and perpendicular to the scattering plane are given by [78] as

$$\langle \mu_{\parallel}^2 \rangle = \left[\langle \alpha'_{ij} \rangle^2 (\cos^2 \phi \cos^2 \theta + \sin^2 \theta) + \langle \alpha'_{ii} \rangle^2 \sin^2 \phi \cos^2 \theta \right] E_y^2 \quad (2.13)$$

$$\langle \mu_{\perp}^2 \rangle = \left[\langle \alpha'_{ij} \rangle^2 \sin^2 \phi + \langle \alpha'_{ii} \rangle^2 \cos^2 \phi \right] E_y^2 \quad (2.14)$$

where the angles θ and ϕ define the scattering direction in polar coordinates, with θ measured from the \hat{e}_z axis and ϕ measured from the \hat{e}_x axis as shown in Figure 2.1. Equations 2.13 and 2.14 will be identical for a forward scattering experiment, assuming the incident laser now propagates along the \hat{e}_x axis in the $+\hat{e}_x$ direction with the laser again linearly polarized with the electric field aligned in the \hat{e}_y direction, keeping the collection optics aligned along the $+\hat{e}_x$ axis. A sketch of this forward scattering configuration is shown in Figure 2.1b. However, high-fidelity ro-vibrational spontaneous Raman simulations require accounting for the finite solid angle of the collection lens and the polarization sensitivity of the collection optics. If the laser is not purely linearly polarized, scattering due to both components of the laser electric field should also be included. In a multiple-pass cell setup, the polarization direction changes slightly with each pass, and this should be included when the collection solid angle is large [52]. When these factors are included and integrated over a finite collection angle, the squares of the induced dipole moment will not be identical for the side and forward scattering configurations.

The intensity of the spontaneous Raman signal of a particular ro-vibrational Stokes transition for a single molecular species is given by [1]:

$$I(v, J, \Delta v, \Delta J) = \frac{G}{T} [\tilde{\nu}_0 - \tilde{\nu}_k(\Delta v, \Delta J)]^4 g_s(J) \frac{(2J+1) e^{-\frac{hcE_v(v)}{kT}} e^{-\frac{hcE_r(v,J)}{kT}}}{Q(T)} \Phi(\Delta v, \Delta J) \quad (2.15)$$

assuming the molecules are in thermal equilibrium at temperature T with state populations represented by a Boltzmann distribution. In Equation 2.15, G is a scaling constant that accounts for incident laser intensity and number density, $\tilde{\nu}_0$ is the frequency of the laser, $\tilde{\nu}_k$ is the frequency of the molecular transition, g_s is the nuclear spin statistical weight, Q is the internal partition function, and Φ is the space-averaged polarizability tensor, including the angular dependence for a finite collection solid angle [1, 51, 78, 52]. The values for the polarizability tensor components are extracted from experimental measurements of transition cross-sections and depolarization ratios [80]. The expressions for polarizability tensor components for N_2 used in this work are given in Buldakov et al. [79]. The nuclear spin statistical weight for $^{14}\text{N}_2$ in the electronic ground state is $g_s = 3$ for odd J and $g_s = 6$ for even J [1]. Thus the odd J lines are half as strong as the even J lines for $^{14}\text{N}_2$. For the rare nitrogen isotopologue $^{15}\text{N}^{14}\text{N}$, which constitutes 0.725% of naturally occurring N_2 , the nuclear spin statistical weight is $g_s = 6$ for every J value because it is a heteronuclear diatomic molecule. The frequency of the molecular transition, $\tilde{\nu}_k$, corresponds to the energy difference between the initial and final state of the molecule. For this work, the diatomic molecule will be modeled as an anharmonic oscillator and non-rigid rotor with the energy of a particular vibrational and rotational state calculated as

$$\begin{aligned}
 E(v, J) = & \omega_e \left(v + \frac{1}{2} \right) - \omega_e x_e \left(v + \frac{1}{2} \right)^2 + \omega_e y_e \left(v + \frac{1}{2} \right)^3 + \omega_e z_e \left(v + \frac{1}{2} \right)^4 \\
 & + \left[B_e - \alpha_e \left(v + \frac{1}{2} \right) + \gamma_e \left(v + \frac{1}{2} \right)^2 \right] J(J+1) - D_e J^2 (J+1)^2
 \end{aligned} \tag{2.16}$$

where the molecular constants are listed in Table 2.3 [81, 82]. As described in [78], the vibrational constants for $^{15}\text{N}^{14}\text{N}$ were calculated by scaling the vibrational constants of $^{14}\text{N}_2$. The scaling factor is ρ^n where ρ is the square root of the ratio of the reduced

mass of $^{14}\text{N}_2$ to the reduced mass of $^{15}\text{N}^{14}\text{N}$ and n is the order of the term associated with the molecular constant [83].

Table 2.3: Molecular constants for nitrogen in cm^{-1} [81, 82].

	$^{14}\text{N}_2$	$^{15}\text{N}^{14}\text{N}$
ω_e	2358.57	2318.93
$\omega_e x_e$	14.324	13.847
$\omega_e y_e$	-2.26×10^{-3}	-2.15×10^{-3}
$\omega_e z_e$	-2.4×10^{-4}	-2.24×10^{-4}
B_e	1.99824	1.93185
α_e	1.7318×10^{-2}	1.6466×10^{-2}
γ_e	-3.3×10^{-3}	-2.22×10^{-5}
D_e	-5.71×10^{-6}	-5.35×10^{-6}

Equation 2.15 specifies the integrated intensity of each ro-vibrational spontaneous Raman line, i.e. the area under the spectrally broadened lineshape. For the experimental conditions in this work, Doppler broadening is negligible relative to collision broadening, which is also referred to as pressure broadening. The experimentally recorded lineshape function was taken to be a convolution of a Lorentzian function and a trapezoidal function. The trapezoidal function represents one contribution to line broadening due to the instrument. The Lorentzian lineshape function represents the other instrument line broadening contribution, as well as the molecular line broadening, which changes with gas density. This choice of lineshape function was found to minimize systematic error between simulated and experimental spectra [51, 78]. Because the convolution of two Lorentzian functions is another Lorentzian whose halfwidths is the sum of the individual Lorentzian halfwidths, the Lorentzian

function can be described by a single halfwidth parameter. The trapezoidal function is described by two parameters: the halfwidths of the trapezoid base and tip respectively. Thus three parameters are required to define the trapezoid-Lorentzian lineshape function.

Using Equation 2.15, a high-fidelity spontaneous Raman scattering simulation code was developed at The University of Texas at Austin for ro-vibrational Stokes scattering from nitrogen [51, 78]. This model can be fit to an experimental spectrum using a Levenberg-Marquandt algorithm to minimize the square error, to obtain a point measurement of the gas temperature. If thermal non-equilibrium is present, this fitting technique can be used to extract independent rotational and vibrational temperatures from a single spontaneous Raman measurement recorded at high dispersion [84, 75].

Implementing this technique in high pressure combustion chambers such as optically accessible gas turbine engine test rigs could provide accurate nonintrusive, temperature measurements with high spatial resolution in realistic gas turbine operating conditions. However, the high pressure environment complicates spontaneous Raman thermometry because as the gas density increases, the collision frequency increases, causing spectral lines to broaden and mix [50]. Line mixing can change the observed relative peak intensity of individual rotation or vibration-rotation transitions. Because thermometry is accomplished by relating relative intensities to relative state populations through a Boltzmann factor, spectral models that neglect line mixing could lead to erroneous temperature inference when line mixing effects are significant. The accuracy of spontaneous Raman thermometry depends on the fidelity of Raman simulations. Therefore, it is imperative that these density effects

be carefully characterized before utilizing spontaneous Raman thermometry in high pressure gases. The next section provides some general background theory on line mixing and the Modified Exponential Gap (MEG) line mixing model. Hartmann, Boulet, and Robert's book [50] is an excellent reference for in-depth discussions of line mixing theory. The literature cited within that book and in this dissertation provides additional information.

2.1 Line Mixing

At low enough pressures, the spectral lines are isolated and the pressure broadening of individual spectral lines does not affect their integrated intensities even if they are partially overlapped in the wings of the lines. Line mixing at high pressures invariably occurs when the lines are strongly overlapped, but the mixing effect is not merely the effect of overlap, but is a transfer of integrated intensity between the spectral features that are associated with individual rotation or vibration-rotation transitions at low pressure. As described by Gordon [73] the spectrum can no longer be interpreted as the sum of individual contributions from lines associated with distinct vibration-rotation transitions and must be computed by diagonalizing a matrix whose elements reflect the collisional coupling of the ro-vibrational states.

As mentioned above, the isotropic component of ro-vibrational spontaneous Raman scattering can be treated separately from the anisotropic component. For ro-vibrational scattering, the Q branch lines for a particular vibrational transition are closely spaced and only slightly offset from one another due to rotation-vibration interaction. Therefore, the Q branch lines are strongly overlapped and line mixing effects are significant within the isotropic component of the Q branch. The primary

contribution to line mixing effects in the Q branch arises from vibrationally elastic and rotationally inelastic collisions; vibrational dephasing effects are assumed to be small [61].

The impact approximation assumes that all times of interest are much greater than the collision duration [50], which implicitly assumes that velocities in successive collisions are treated as uncorrelated [73]. Gordon [73] provides criteria to assess the validity of the impact approximation. It is valid for the conditions studied in this work. When the impact approximation holds, the spectral intensity as a function of frequency, $I(\omega)$, can be related to collisions through a general expression [73, 61, 85, 86] as

$$I(\omega) = \text{Im} [c \mathbf{d} \cdot (-\omega \mathbf{I} + \boldsymbol{\omega}_0 + i\mathbf{\Pi})^{-1} \cdot \mathbf{P} \cdot \mathbf{d}] \quad (2.17)$$

where \mathbf{d} is a vector of transition dipole amplitudes, \mathbf{P} is a diagonal matrix of populations, $\mathbf{\Pi}$ is a matrix of collisional transfer rates, $\boldsymbol{\omega}_0$ is a diagonal matrix of transition frequencies, \mathbf{I} is the identity matrix, and c is a constant. Equation 2.17 has the same general form for many types of molecular spectra [85] including absorption [73, 86], inverse Raman [61], and CARS [65, 67], and Equation 2.17 is also applicable to spontaneous Raman. The matrix $\mathbf{\Pi}$ describes the transfer of intensity between spectral lines due to collisions. The elements of this matrix are determined by the rate of collisions, i.e. the gas density, and the cross section for a change of rotational state [86], so matrix $\mathbf{\Pi}$ can be expressed as

$$\mathbf{\Pi} = \rho \langle v \cdot \sigma \rangle \quad (2.18)$$

where v in this equation is the relative speed in the collision, ρ is the gas density, σ is a matrix of cross sections, and the brackets in this equation represent averaging over

a relative speed distribution function [86, 61]. The matrix of cross sections for the isotropic component of the Q branch of Raman scattering is given by [73] as

$$\langle v \cdot \sigma \rangle = \int_0^\infty 2\pi b db \langle v [\delta_{fi} - P_{fi} \exp(-i\eta_{vib})] \rangle \quad (2.19)$$

where v in this equation is the relative speed in the collision, b is the impact parameter, P_{fi} is the probability that a collision transfers the rotation frequency from line i to line f , η_{vib} is the vibrational phase shift in the collision, and the brackets represent averaging over a relative speed distribution function. Equation 2.19 simplifies when vibrational dephasing is negligible ($\eta_{vib} \rightarrow 0$).

A Raman spectrum with line mixing can be calculated by following the approach described by Koszykowski et al. [65] for CARS spectra. The G matrix can be defined as

$$\mathbf{G}(\omega) = -\omega \mathbf{I} + \boldsymbol{\omega}_0 + i\rho \langle v \cdot \sigma \rangle \quad (2.20)$$

which can be used to rewrite Equation 2.17 as

$$I(\omega) = \text{Im} [c \mathbf{d} \cdot \mathbf{G}(\omega)^{-1} \cdot \mathbf{P} \cdot \mathbf{d}] \quad (2.21)$$

The imaginary part of the diagonal elements of the G matrix represents the half-widths of isolated lines, i.e. without line mixing. The off-diagonal elements represent the collisional coupling of ro-vibrational states. At low pressures, only the diagonal elements of the G matrix contribute, and $I(\omega)$ reduces to a sum of isolated Lorentzian lines [65]. Equation 2.17 requires an inversion of the G matrix for every frequency included in the simulation. This costly computation can be avoided using a diagonalization approach which requires only one matrix inversion, as first described by Gordon and McGinnis [85] and detailed by Koszykowski et al. [65]. First, a matrix

\mathbf{K} is defined to be a subset of the G matrix as

$$\mathbf{K} = \mathbf{G}(\omega) + \omega \mathbf{I} = \omega_0 + i\rho \langle v \cdot \sigma \rangle \quad (2.22)$$

so that the matrix \mathbf{K} is constant for all simulation frequencies. Let λ_n be the n th eigenvalue of matrix \mathbf{K} and \mathbf{A} be the matrix of the eigenvectors of \mathbf{K} . The eigenvector matrix \mathbf{A} can be used to diagonalize \mathbf{K} . Through substitution and rearrangement of terms, this diagonalization can be used to rewrite Equation 2.21 as

$$I(\omega) = c \sum_n \text{Im} \left[\frac{[(\mathbf{d}\mathbf{A}) \cdot (\mathbf{A}^{-1}\mathbf{P}\mathbf{d})]_n}{-\omega + \lambda_n} \right] \quad (2.23)$$

which calculates the mixed ro-vibrational Raman spectrum for a single vibrational transition. To include multiple vibrational transitions in a simulated ro-vibrational spectrum, Equation 2.23 can be recalculated and summed for each vibrational level. Note that because the matrix \mathbf{K} is a function of the transition frequencies, ω_0 , the eigenvector matrix, \mathbf{A} , and the eigenvalues, λ_n , must be recalculated for every vibrational level. Appendix A contains a detailed derivation of Equation 2.23.

The Modified Exponential Gap (MEG) model can be used to calculate the off-diagonal elements of the G matrix, and this model was found to show good agreement with experimental inverse Raman spectra [61]. The expression for the off-diagonal elements of the collisional matrix for the J -increasing transitions ($i < j$) is given by Koszykowski et al. [61] as

$$\rho \langle v \cdot \sigma \rangle_{ji} = \gamma_{ji} = \alpha P \left(\frac{1 + 1.5 E_i/kT\delta}{1 + 1.5 E_i/kT} \right) \exp \left(\frac{-\beta \Delta E_{ij}}{kT} \right) \quad (2.24)$$

where α , β , and δ in Equation 2.24 are parameters, P is the pressure, E_i is the initial state rotational energy, ΔE_{ij} is the difference in energy between the initial and final states, and k is the Boltzmann constant. To extend the MEG model to

high temperatures, a preexponential factor for the off-diagonal G matrix elements was proposed first by Rahn and Palmer [66] and then improved to be more suitable for temperatures above 1500 K by Farrow et al. [67]. This preexponential factor is given by [67] as

$$f(T) = \frac{1 - \exp(-m)}{1 - \exp(-mT/T_0)} \left(\frac{T_0}{T}\right)^{0.5} \quad (2.25)$$

where m is a parameter and T_0 is a reference temperature of $T_0 = 295$ K [67]. Equation 2.24 is multiplied by the preexponential factor given by Equation 2.25 to obtain the off-diagonal elements for the J -increasing transitions. The off-diagonal G matrix elements for the J -decreasing transitions are calculated from detailed balance, given by [61] as

$$\gamma_{ij} = \frac{2J_i + 1}{2J_j + 1} \gamma_{ji} \exp\left(\frac{\Delta E_{ij}}{kT}\right) \quad (2.26)$$

where J_i is the rotational quantum number of state i and γ_{ji} is given by Equation 2.24 multiplied by the the preexponential factor given by Equation 2.25. Because $^{14}\text{N}_2$ is a homonuclear diatomic, spin symmetry restrictions prohibit transitions between even and odd rotational states. Therefore, the off-diagonal elements of the G matrix corresponding to transitions between even and odd rotational states must be set to zero for $^{14}\text{N}_2$. The nitrogen isotopologue $^{15}\text{N}^{14}\text{N}$ does not have these spin symmetry restrictions because it is a heteronuclear diatomic.

With the matrix \mathbf{K} defined by Equation 2.22, the diagonal elements of \mathbf{K} are given by [65] as

$$\mathbf{K}_{jj} = (\boldsymbol{\omega}_0)_{jj} - i \frac{\Gamma_j}{2} \quad (2.27)$$

where Γ_j is the collision broadening portion of the linewidth (FWHM). When vibrational dephasing is negligible, the collision broadening portion of the linewidth is

determined by the total rate of perturbing collisions [66, 61], so

$$\frac{\Gamma_j}{2} = \sum_{i \neq j} \gamma_{ij} . \quad (2.28)$$

The high-temperature MEG model parameters used for all MEG model calculations in this dissertation are the m -MEG parameters found in Lavorel et al. [68]. The values for these parameters are listed in Table 2.4. With these parameters, the above MEG model equations, and the calculation method given by Equation 2.23, the isotropic component of the ro-vibrational spontaneous Raman spectrum can be simulated with line mixing.

Table 2.4: MEG model parameters from Lavorel et al. [68].

α (cm ⁻¹ atm ⁻¹)	β	δ	m
26.46×10^{-3}	1.850	1.199	0.1381

The relaxation cross sections for isotropic Raman scattering, given by Equation 2.19, are not the same as the cross sections for anisotropic Raman scattering [72, 73]. Line mixing causes anisotropic lines to exchange intensity among all three branches of the ro-vibrational anisotropic Raman spectrum (O, Q, and S). Therefore, equations analogous to Equation 2.19 are required to calculate the cross sections for anisotropic scattering, including cross sections for mixing within each branch of the anisotropic spectrum and mixing between the branches. The integrands of these equations for cross sections for the anisotropic spectrum are provided by Gordon [73] and listed in Table 2.5. Each column in Table 2.5 lists the integrands for the cross sections describing the mixing for that column's branch with the three anisotropic branches (the rows of Table 2.5).

Table 2.5: Integrands for matrix cross sections for anisotropic Raman scattering [73].

	O	Q	S
O	$\delta_{fi} - P_{fi} \cos^4\left(\frac{\alpha}{2}\right) e^{-2i\eta}$	$-\frac{\sqrt{6}}{4} P_{fi} \sin^2(\alpha) e^{-2i\eta}$	$-P_{fi} \sin^4\left(\frac{\alpha}{2}\right) e^{-2i\eta}$
Q	$-\frac{\sqrt{6}}{4} P_{fi} \sin^2(\alpha)$	$\delta_{fi} - \frac{1}{2} P_{fi} (3 \cos^2(\alpha) - 1)$	$-\frac{\sqrt{6}}{4} P_{fi} \sin^2(\alpha)$
S	$-P_{fi} \sin^4\left(\frac{\alpha}{2}\right) e^{2i\eta}$	$-\frac{\sqrt{6}}{4} P_{fi} \sin^2(\alpha) e^{2i\eta}$	$\delta_{fi} - P_{fi} \cos^4\left(\frac{\alpha}{2}\right) e^{2i\eta}$

In Table 2.5, α represents the rotational reorientation induced by collisions and η represents rotational dephasing. Neither of these effects can be reasonably neglected and they are both dependent on the individual rotational states. Therefore, modeling line mixing in the anisotropic spectrum is substantially more challenging than for the isotropic spectrum. Table 2.5 shows that line mixing effects in the anisotropic component are not identical to line mixing effects in the isotropic component, even in the Q branch. However, it is common to make this simplifying assumption when simulating Raman spectra with line mixing. Ultimately, this assumption is highly unlikely to impact CARS thermometry because the anisotropic contribution to CARS spectra is significantly weaker than the anisotropic contribution to spontaneous Raman spectra. This is because the CARS matrix elements scale as the square of the susceptibility, so if the anisotropic contribution to the spontaneous Raman signal is 1%, then the anisotropic contribution to the CARS signal is 0.01%.

The significance of line mixing effects in the anisotropic component of rovibrational spontaneous Raman scattering is not well understood. Ignoring or misrepresenting mixing effects in the anisotropic spectrum could lead to erroneous temperature measurements from spontaneous Raman thermometry in high pressure gases. We believe that fitting high-fidelity spontaneous Raman simulations to the entire rovibrational spectrum improves the accuracy of the measurement. However, this will

not be true for measurements in high pressure gases if the Raman simulations do not capture the collision-induced effects of the entire ro-vibrational spectrum. Therefore, this work studies the influence of high pressure on ro-vibrational spontaneous Raman scattering, focusing in particular on the anisotropic component and the impact on the accuracy of spontaneous Raman thermometry in high pressure gases.

Chapter 3

Elevated Pressure Thermometry

This chapter presents experimental measurements of temperature in elevated pressure using spontaneous Raman scattering from nitrogen. Accurate temperature measurements of temperature profiles, particularly in near-wall regions, provide valuable insights for the gas turbine engine design process. Two advantages of spontaneous Raman thermometry relevant to this application are good spatial resolution and accuracy at high temperatures [17]. In these experiments, these advantages are demonstrated by making time-averaged measurements of a temperature profile through the flame front of a partially premixed flame using spontaneous Raman scattering. These temperature measurements were achieved despite interference from stray laser reflections in an elevated pressure combustion chamber. This achievement shows that spontaneous Raman thermometry is possible in a near-wall region, where interference from laser reflections is expected to be significant. Additionally, the accuracy of these temperature measurements was assessed by using spontaneous Raman scattering to measure the temperature above a burner with reference temperatures established by coherent anti-Stokes Raman scattering (CARS). Lastly, the experiments presented

Portions of this chapter previously appeared in the following publication:

Haller, T. W., Reising, H. H., Clemens, N. T., and Varghese, P. L., "High-pressure spontaneous Raman scattering based temperature measurements," *33rd AIAA Aerodynamic Measurement Technology and Ground Testing Conference*, ser. 2017-3898, 2017. DOI: 10.2514/6.2017-3898.

The dissertator contributed to this publication through design and conduct of the research, data analysis and interpretation, and writing of the manuscript.

in this chapter also provide a preliminary investigation into a primary complication that arises when considering the implementation of spontaneous Raman thermometry in a gas turbine engine: the high pressure environment. The ro-vibrational spontaneous Raman spectrum of nitrogen was recorded at pressures up to 5 atm. While this elevated pressure does not cover the full range of pressures found in gas turbine engines, these experiments provide an initial assessment of the feasibility of using spontaneous Raman scattering to measure temperature profiles in gas turbine engine environments. The results in this chapter were presented in [87].

3.1 Experimental Setup

These experiments were conducted in the elevated pressure combustion facility on the Pickle Research Campus at The University of Texas at Austin [88]. This facility was designed to operate at pressures up to 10 atm, but at the time of these experiments, this facility had not yet been hydrostatically tested over the full pressure range. Hence, the maximum pressure available for these experiments was limited to 5 atm. Figure 3.1 shows a photograph of the combustion facility and the Raman scattering experimental setup. The test section has three rectangular windows for optical access. The two large windows ($15.2\text{ cm} \times 6.1\text{ cm}$) are both oriented at an angle of 70° with respect to the smaller window ($10.1\text{ cm} \times 3.8\text{ cm}$). The windows are made of fused silica glass. The interior diameter of the test section is 20.3 cm. A continuous flow of cooling air is supplied by a large external, medium pressure gas tank with a maximum pressure of 10 atm. The cooling air co-flow enters the cylindrical combustion chamber through the bottom of the chamber, flowing upward and around any burner apparatus placed in the center of the combustion chamber, protecting the windows from hot combustion products. This elevated combustion chamber is

designed for a maximum thermal heating power of 300 kW [88]. For safety purposes, all experiments conducted in this facility were operated remotely and monitored with security cameras.

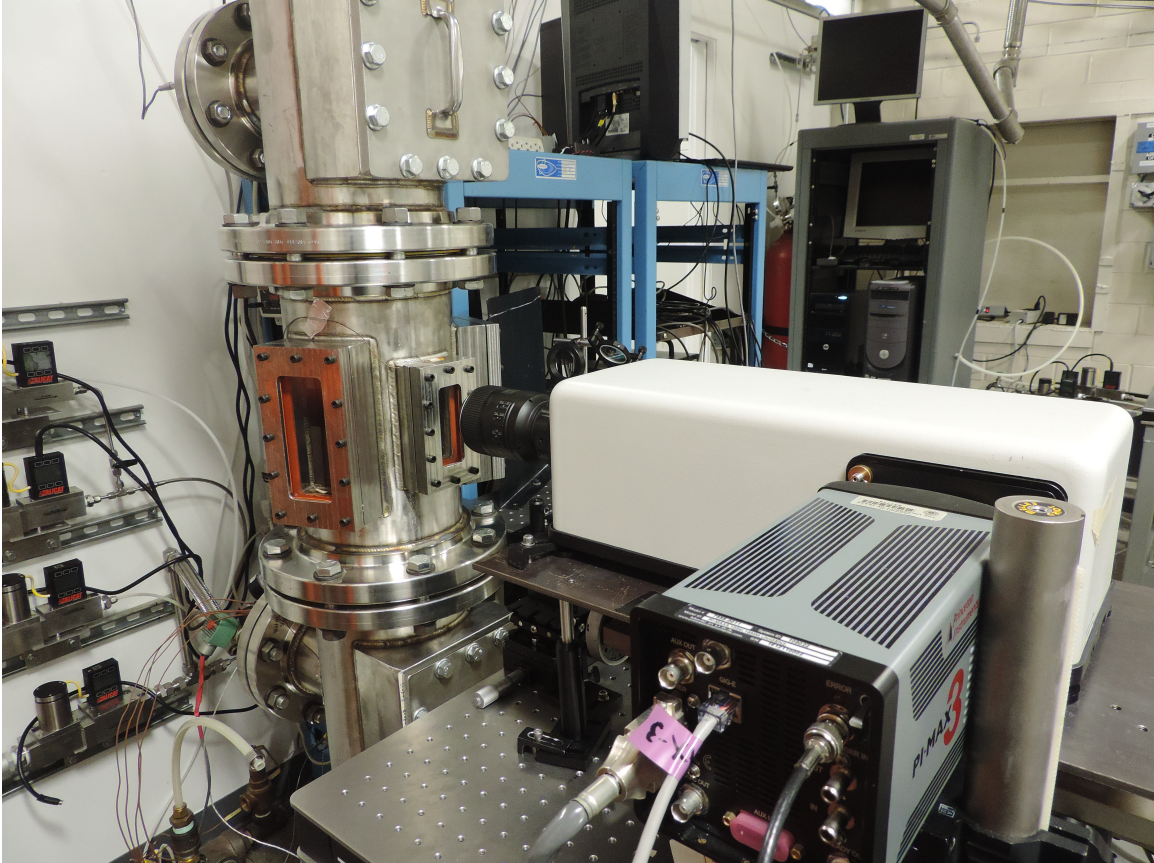


Figure 3.1: Photograph of the elevated pressure combustion facility and the Raman scattering experimental setup.

The laser source for the spontaneous Raman scattering measurements was a frequency doubled Nd:YLF laser (527 nm) with a pulse-energy of 12 mJ and a repetition rate of 5 kHz. A high-repetition rate laser is well-suited for time-averaged measurements because it maximizes the average power output. The low pulse-energy also significantly reduces the risk of window damage. For these experiments, the

laser was passed into and out of the test section through the two larger windows, and the Raman signal was collected in a side-scattering configuration through the small window. These windows do not have anti-reflection coatings. Because these windows are not parallel to each other, the reflections of the laser from the interior surfaces of the windows did not exit the combustion chamber through the opposite window. Instead, these laser reflections were directed into the stainless steel walls of the combustion chamber, resulting in specular and diffuse reflections that illuminated the entire chamber with laser light. The reflections from the laser can be partially seen in Figure 3.2, which shows a photograph of the laser in the combustion chamber.

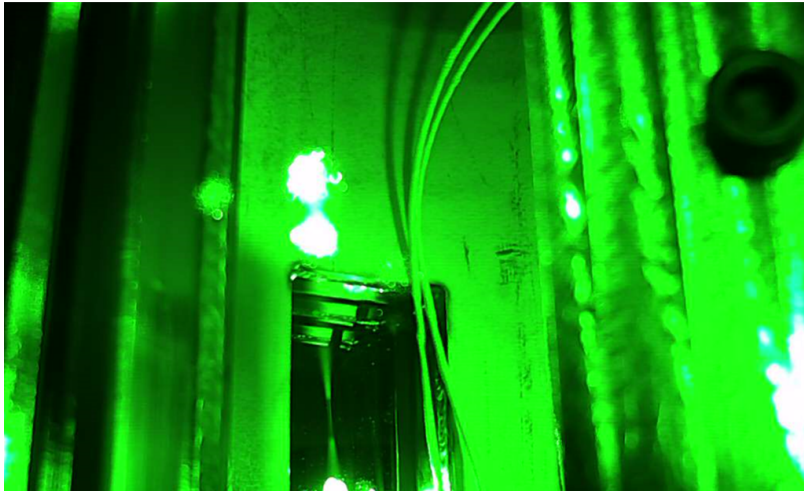


Figure 3.2: Photograph of the laser in the elevated pressure combustion chamber.

This reflected laser light had to be removed with a filter. A background subtraction approach can also be utilized to remove the reflected laser light from the Raman spectra, but this approach requires removing the nitrogen from the chamber to obtain a background image of the reflected laser light without the Raman signal. Removing the nitrogen for a background image was not possible in this combustion chamber because it was designed to be filled and pressurized with air from an in-house

compressor. Regardless, a similar challenge would likely be present in a realistic gas turbine engine test rig, where interference from laser reflections may be unavoidable due to limited optical access. So performing spontaneous Raman thermometry experiments in this combustion chamber presented similar challenges to those that might be found in a gas turbine engine application.

The laser was focused into the combustion chamber with a plano-convex lens with a focal length of 50 cm. The focusing lens was positioned so that the horizontal location of the laser focus approximately aligned with the vertical centerline of the small window. The Raman signal was collected through the small window with a 62 mm diameter Nikon lens, as seen in Figure 3.1. The collection lens was positioned so that the collection volume was centered on the focus of the laser. Using the small window to collect the spontaneous Raman signal had the disadvantage of reducing the maximum available collection solid angle. However, collecting the Raman signal perpendicular to the laser beam maximizes the strength of the side-scattered Raman signal [52]. This configuration also improves the spatial resolution by minimizing the collection volume, which is crucial for measuring a steep temperature gradient.

The collection lens focused the Raman signal into an f/1.8 imaging spectrograph from Kaiser Optical Systems, equipped with a PI-MAX 3 ICCD camera from Princeton Instruments that has 26 μm pixels. Figure 3.3 shows a detailed schematic of the imaging spectrograph operating in the side-scattering configuration. This spectrograph contains a filter section which uses two lenses and a holographic notch filter to remove light at the incident laser wavelength, which is reflected back out of the spectrograph. For all of the experiments presented in this chapter, the notch filter alone was sufficient to prevent the stray laser light from overwhelming the Raman

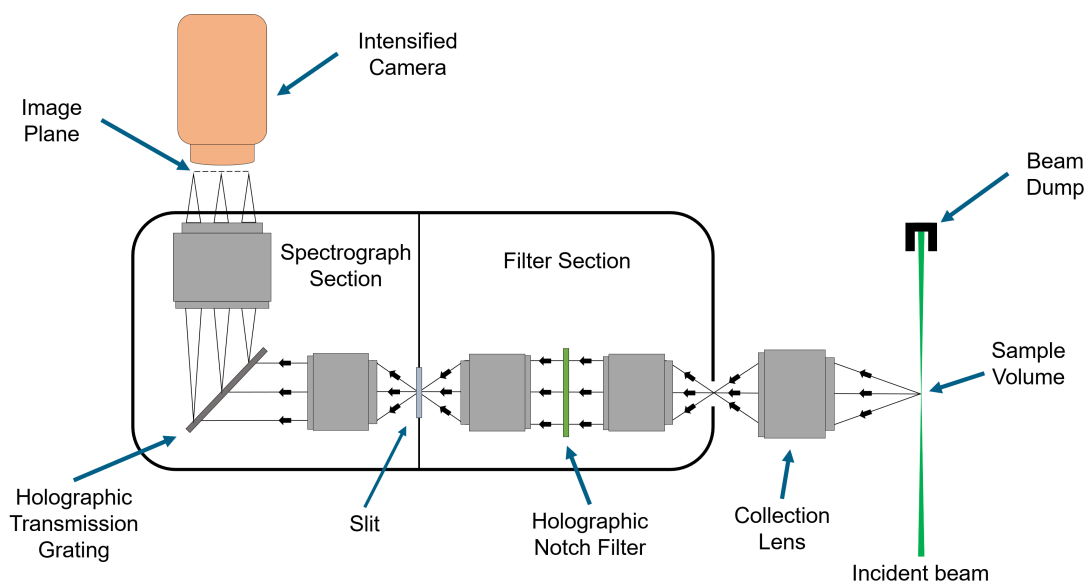


Figure 3.3: Diagram of the f/1.8 imaging spectrograph from Kaiser Optical Systems collecting spontaneous Raman signal in a side-scattering configuration.

signal; no additional filters were needed. The spectrograph was equipped with a high dispersion holographic transmission grating (HDG-607). For all of the experiments presented in this chapter, the slit size was 100 μm .

The burner for these experiments consisted of a 13 mm diameter stainless steel tube. This simple burner design was chosen to produce a flame with a strong radial temperature gradient. The experimental objective was to measure this temperature gradient. A supply of methane, hydrogen, and air was fed into the burner with the flowrates of each gas controlled by individual mass flow controllers. The flow from this burner exhausted into an air coflow, resulting in a partially premixed flame upon ignition. Figure 3.4 shows a photograph of the flame in the combustion chamber at a pressure of 1 atm. The laser was located 2 cm above the burner tube exit.

The burner was mounted on a translation stage which allowed for translation



Figure 3.4: Photograph of the flame in the combustion chamber at 1 atm.

of the burner along the axis of the laser beam. This translation stage was controlled remotely with software. A flashback arrestor was placed in the gas supply line just upstream of the burner, and an electric surface igniter was installed to ignite the flame. Figure 3.5a shows a schematic illustrating the translation of the burner and the measurement region. Figure 3.5b shows a photograph of the burner, translation stage, and surface igniter. The entire assembly was mounted to an aluminum sled that was slid into the combustion chamber.

3.2 Elevated Pressure Results

To examine the effects of elevated pressure ro-vibrational Stokes spontaneous Raman scattering from nitrogen, spectra were recorded in the combustion chamber at 1 atm and 5 atm, at room temperature and flame temperature. The fuel mixture for the flame temperature spectra was 70 % CH_4 and 30 % H_2 by volume. The equivalence ratio was 1.8 relative to the compressed air flow rate. The collection time for the room temperature spectra was 2 min. The collection time for the flame temperature spectrum at 1 atm was 6 min, and it was 2 min at 5 atm. The longer collection time for

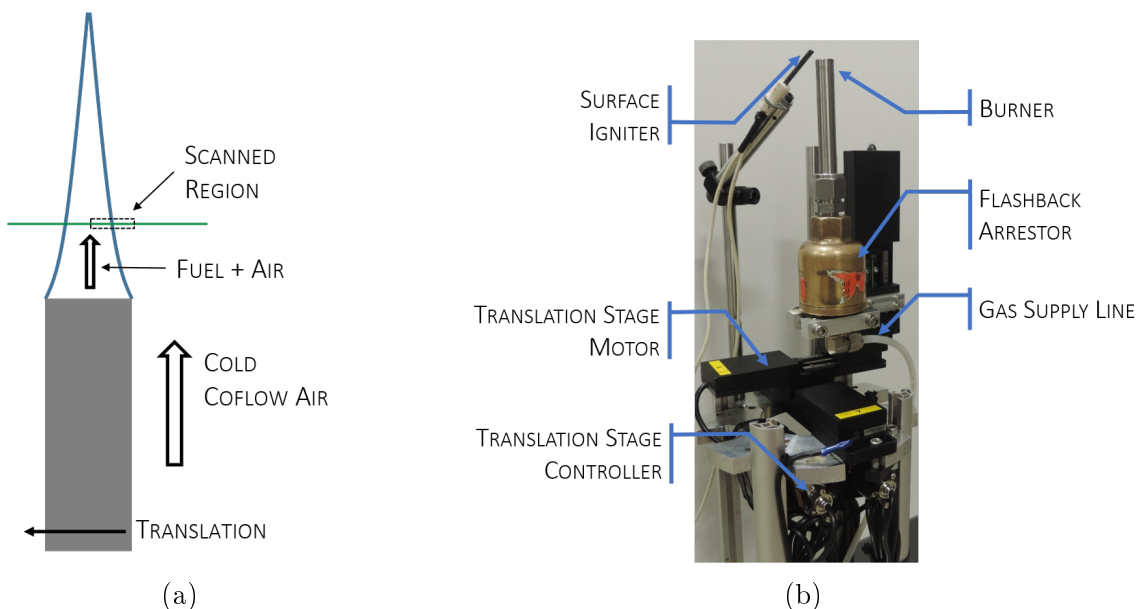


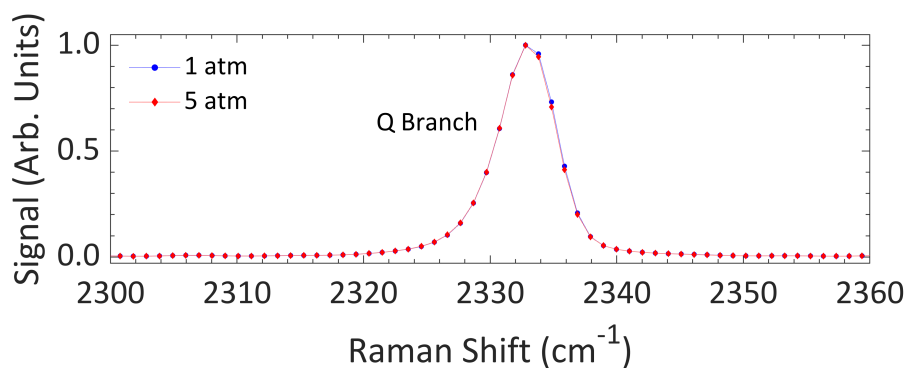
Figure 3.5: (a) Schematic showing the burner translation direction and measurement region, and (b) photographs of the burner assembly

the 1 atm, flame temperature spectrum was necessary due to the lower number density of nitrogen at this condition. These collection times were chosen so that resulting spectra are nearly noise-free and illustrate the details of the weaker rotational lines that make up the O and S branches.

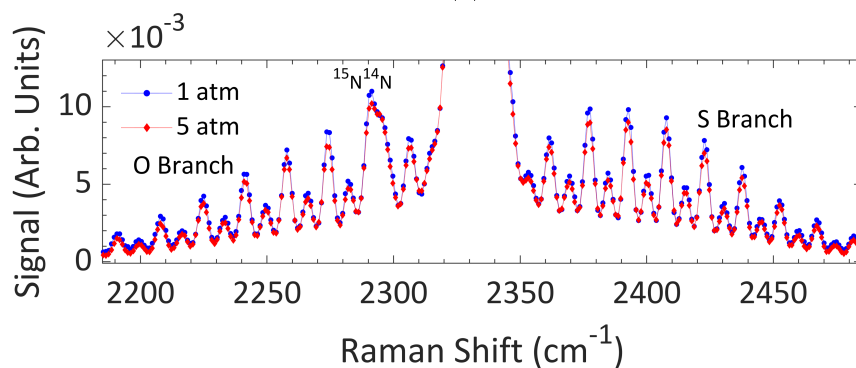
Figure 3.6 shows a comparison for spectra recorded at 1 atm and 5 atm at room temperature. The Q branch is very similar at 1 atm and 5 atm, as seen in Figure 3.6a. The vertical scale is magnified by a factor of 100 in Figure 3.6b to show the rotational structure of the O and S branches. There are slight differences between the O and S branches of the 1 atm and 5 atm spectra in Figure 3.6b. The peaks of the rotational lines of the 1 atm spectrum have a slightly higher intensity than the rotational peaks of the 5 atm spectrum. This small discrepancy can be attributed to pressure broadening in the O and S branches. As the spectral lines broaden with increasing

pressure, the peak intensity of the lines will drop. Although the differences in the spectra in Figure 3.6b are slight, this signature of pressure broadening is visible for every rotational line. From Figure 3.6b, we can conclude that pressure broadening is detectable in the O and S branches at 5 atm and room temperature despite substantial instrument broadening. This conclusion is important because the broadening is expected to linearly increase with increasing pressure [50]. Gas turbine engines operate at pressures higher than 5 atm, and because thrust specific fuel consumption decreases with increasing compressor pressure ratio [3], there is always motivation to design gas turbine engines to run at increased pressure. Therefore, pressure broadening is likely to have a significant effect on the O and S branches at gas turbine operating conditions.

Figure 3.7 shows a comparison for spectra recorded at 1 atm and 5 atm at flame temperature. The higher vibrational states are populated at flame temperature, which is evident in Figure 3.7a by the multiple hot band peaks present in the Q branch. Additionally, the Raman signal from CO can be seen in Figure 3.7a. In Figure 3.7b, the S branch lines of the 5 atm spectrum are very similar to the S branch lines of the 1 atm spectrum. Because pressure broadening scales with density, the broadening at flame temperature will be less than at room temperature for a given pressure. This explains why Figure 3.7b shows no discernable evidence of pressure broadening effects between the 1 atm and 5 atm spectra. Over this range of densities and with this spectral resolution, the linewidths of the anisotropic O and S branch lines are dominated by the instrument lineshape function, which of course does not depend on density. So any pressure broadening effects are not detectable at 5 atm and flame temperature with this spectral resolution.



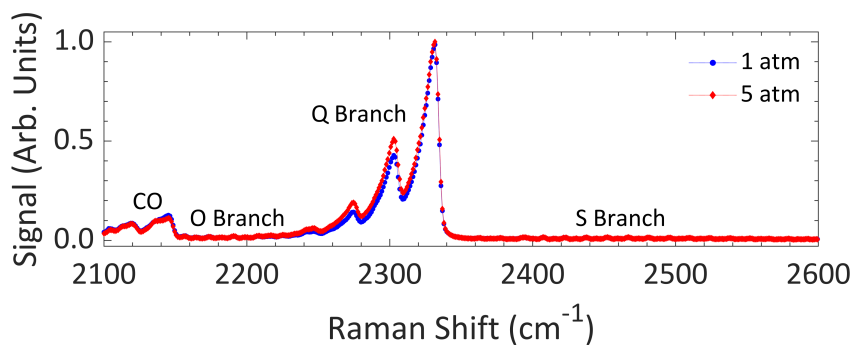
(a)



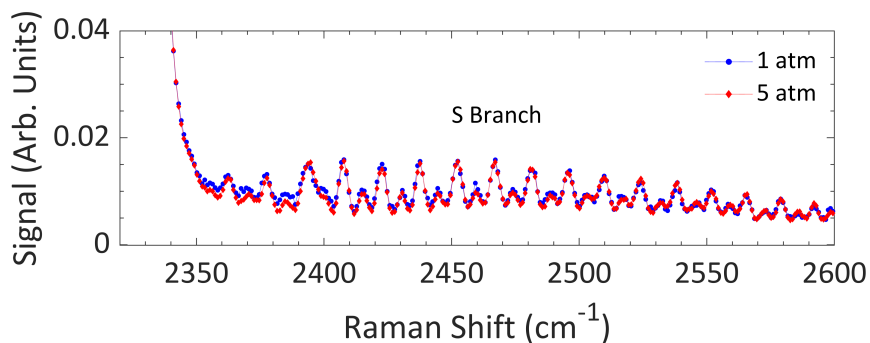
(b)

Figure 3.6: Comparison between nitrogen Stokes Raman spectra at 1 atm and 5 atm at room temperature. (a) Recorded spectra in the region of the Q branch scaled to unit maximum intensity. (b) Spectra over an extended frequency range with vertical scale magnified to show the rotational structure from O and S branches of the $^{14}\text{N}_2$ isotopologue and the Q branch of the $^{15}\text{N}^{14}\text{N}$ isotopologue.

In contrast, Figure 3.7a does show discernable differences in the Q branch between the 1 atm and 5 atm spectra. The peaks of the higher vibrational modes appear lower relative to the fundamental vibrational peak ($v_i = 0$) for the 1 atm spectrum compared to the 5 atm. Note that the spectra in Figure 3.7 are both scaled to unit maximum intensity. The differences in the Q branch are not due to density effects; they are due to temperature differences. The gas temperature was not the same for these two spectra, which means that the higher vibrational modes were



(a)



(b)

Figure 3.7: Comparison between nitrogen Stokes Raman spectra at 1 atm and 5 atm at flame temperature. (a) Recorded spectra scaled to unit maximum intensity showing the multiple vibrational modes populated in the Q branch at flame temperature as well as the Raman signal from CO. (b) Spectra in the region of the S branch with vertical scale magnified to show the rotational structure of $^{14}\text{N}_2$.

less populated for the lower temperature 1 atm spectrum, and therefore the peaks of the Q branch are lower relative to the fundamental vibrational peak for the 1 atm spectrum. This temperature difference can be confirmed by fitting these spectra for temperature. The Raman simulation does not include the contribution of CO to the spectrum, so the data points in the region of the CO Raman signal were removed from the experimental spectra before fitting for temperature. Figures 3.8 and 3.9 show temperature fits to the 1 atm and 5 atm spectrum respectively. The inferred temperature for the 1 atm spectrum was 1850 K, and the inferred temperature for the

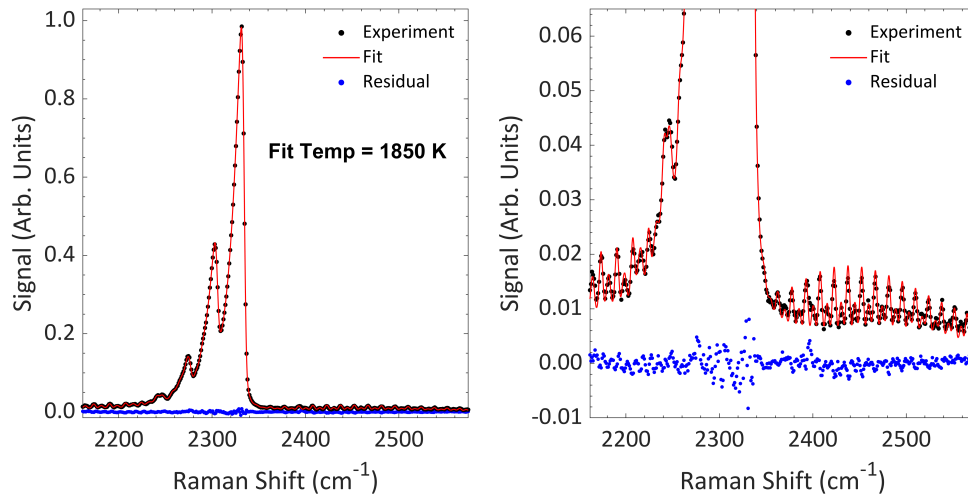


Figure 3.8: Temperature fit to nitrogen Raman spectrum recorded at 1 atm, resulting in an inferred temperature of 1850 K. The right panel shows a magnified vertical scale to show the rotational structure of $^{14}\text{N}_2$.

5 atm spectrum was 2008 K. While the adiabatic flame temperature does vary with pressure, this alone does not fully explain this temperature discrepancy because the adiabatic flame temperature at 1 atm and 5 atm is 2142 K and 2156 K respectively. This temperature discrepancy is likely caused by changes to the flame shape with the increased pressure, resulting in a measurement at a different location relative to the flame front for measurements at a fixed spatial location.

Figures 3.8 and 3.9 show good temperature fits to the 1 atm and 5 atm spectra. In both cases, there are no systematic deviations in the residuals, which indicates that the model simulates the details of the spontaneous Raman spectrum well for these conditions. The model used for these temperature fits uses a trapezoid-Lorentzian lineshape function, as described in [51]. The Lorentzian width is the same for every line. This assumption is acceptable for these experiments because the lineshape function is dominated by the instrument broadening to such an extent that the pres-

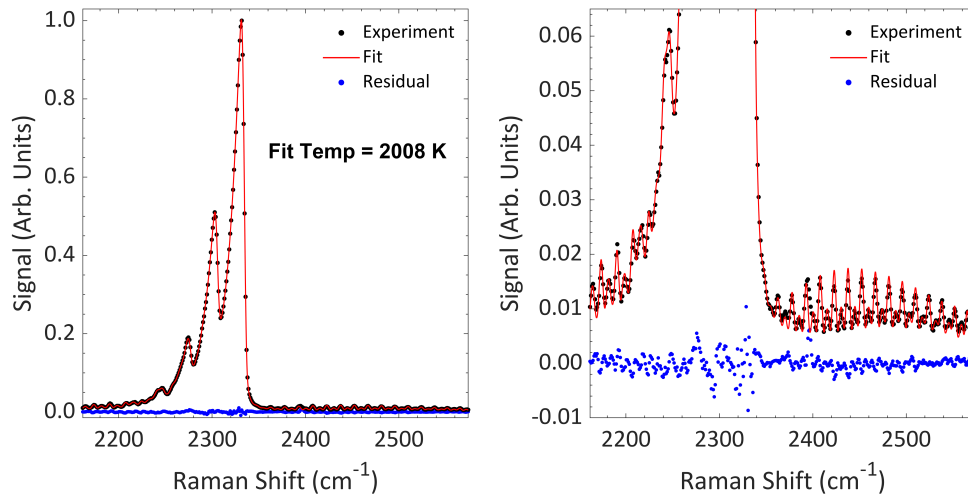


Figure 3.9: Temperature fit to nitrogen Raman spectrum recorded at 5 atm, resulting in an inferred temperature of 2008 K. The right panel shows a magnified vertical scale to show the rotational structure of ¹⁴N₂.

sure broadening, which does have a rotational-number dependence, is not detectable. Figure 3.6b does indicate that pressure broadening is barely detectable at 5 atm and room temperature, but the broadening effects appear to be minimal, and hence are not likely to significantly affect temperature fits at these conditions. At 5 atm and flame temperatures, the density is low enough that the instrument linewidth dominates the measured lineshape. Because the collision-induced effects, such as pressure broadening and line mixing, do not have a significant influence on the linewidths over the pressure range of 1 atm to 5 atm, the trapezoidal-Lorentzian lineshape model can be used for temperature fits to spontaneous Raman spectra recorded in this range of pressures.

3.3 Flame Front Temperature Profile

To demonstrate the feasibility of using spontaneous Raman scattering to probe a temperature gradient, the burner was translated along the beam path while keeping the Raman collection optics fixed. Figure 3.5 shows a schematic and photograph illustrating the burner setup, translation behavior, and the scanned region of the flame. Spontaneous Raman spectra were recorded every 0.5 mm through the flame front. For these measurements, the spatial resolution along the beam path was 0.2 mm. Spectra were recorded through the flame front at three chamber pressures: 1 atm, 3 atm, and 5 atm. At each measurement location, the Raman signal was integrated for a total of 600 000, 400 000, and 200 000 laser pulses for the 1 atm, 3 atm, and 5 atm experiments respectively. With a laser repetition rate of 5 kHz, this equates to collection times of 120 s, 80 s, and 40 s (total laser fluence of 7.2 kJ, 4.8 kJ, and 2.5 kJ) for the 1 atm, 3 atm, and 5 atm experiments respectively. The longer collection times were necessary at the lower pressures due to the reduced number density of nitrogen in the probe volume. At each measurement location, the Raman signal was integrated on chip until the intensity count approached the maximum value that can be stored on the chip, and then the signal was read off the chip and integrated in software. There were 60 readouts per measurement location for the 1 atm experiment and 80 readouts per measurement location for both the 3 atm and 5 atm experiments. Three runs of the experiment were conducted at 5 atm and 1 run each was conducted for the 1 atm and 3 atm conditions.

The recorded spontaneous Raman spectra were all fit for temperature. Figure 3.10 plots the fitted temperatures versus position for every experiment. Error bars of ± 15 K are included in Figure 3.10, which is the estimated uncertainty for

these temperature measurements. The determination of this uncertainty is discussed in detail in the next section. Due to time constraints and the difficulty accessing the interior of the elevated pressure combustion chamber, the position values in Figure 3.10 do not represent a distance relative to a specific burner axis. However, the objective of these experiments was not to study this specific flame and burner. Instead, the objective was to demonstrate that spontaneous Raman scattering can be used to measure a steep temperature gradient. The temperature profiles shown in Figure 3.10 illustrate that this objective was accomplished.

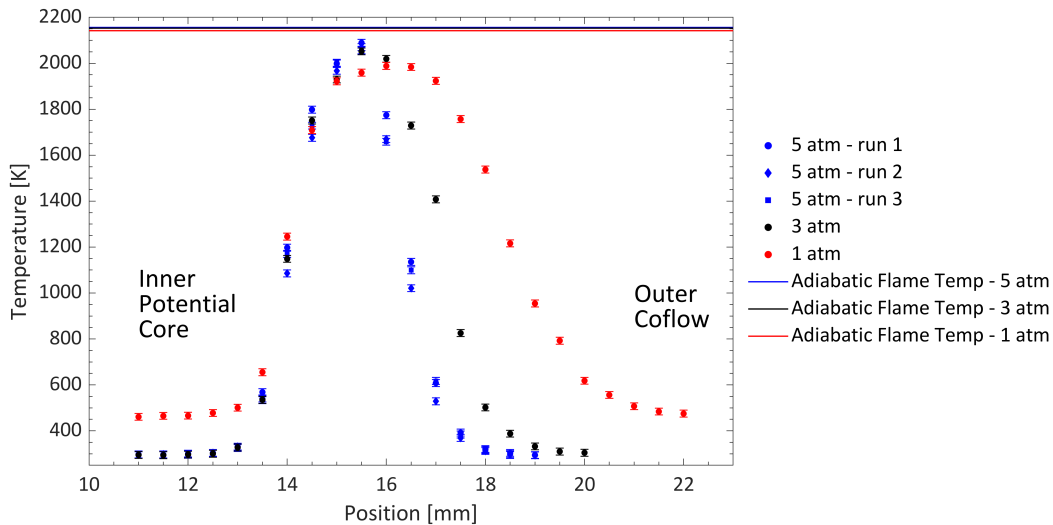


Figure 3.10: Scanned temperature profiles at three pressures: 1 atm, 3 atm, and 5 atm

The steepest temperature gradients occurred for the 5 atm experiments, with a measured gradient of approximately 800 K mm^{-1} through the flame front. For all three pressures the peak temperature was below the adiabatic flame temperature, which has a slight pressure dependence. The temperatures from the three runs with a chamber pressure of 5 atm show good agreement with each other, which is expected because the experimental conditions were identical for these three runs. The mea-

sured temperatures on both sides of the flame front for the 3 atm and 5 atm chamber pressures were approximately ambient room temperature. However, for the 1 atm case the temperature was about 200 K higher. This may be because the shape and size of the flame was not identical for the three chamber pressures, but the position of the laser relative to the burner was the same for all of these experiments. Hence the position of the temperature measurements relative to the reaction zone was not the same for the three chamber pressures.

These experiments have demonstrated that spontaneous Raman thermometry can measure the steep temperature gradient of a flame front in an enclosed, elevated pressure combustion chamber with significant laser reflections. Resolving steep temperature gradients would likely be an important measurement objective of spontaneous Raman thermometry in a gas turbine engine application. These experiments have shown that using spontaneous Raman scattering to measure temperature in a gas turbine engine test rig is at least possible. However, there are several challenges associated with a gas turbine engine application for spontaneous Raman thermometry that have not been investigated by the experiments in this chapter. First, these are time-averaged measurements. Time-resolved measurements would likely be more useful for the design processes of a gas turbine engine. A laser with high energy per pulse can be implemented to achieve single-shot spontaneous Raman temperature measurements [53, 54]. A high energy laser increases the risk of laser damage to the windows, but this risk could be mitigated with a temporal pulse-stretcher [52]. Second, although these experiments were conducted in the presence of strong interference from reflected laser light, this is not the same as measuring temperature in a near-wall region. Also, if optical access was limited to just one window, then there would be significantly more laser interference because the laser would not be able to

exit the chamber. If laser interference overwhelmed the spontaneous Raman signal, additional filters could be used to isolate the Raman signal from the laser light.

Lastly, these experiments were conducted over only a modest range of pressures where the single Lorentzian lineshape model can still represent the experimental spectra well. At 5 atm and room temperature, pressure broadening was barely detectable at the experimental spectral resolution. Because gas turbine engines run at much higher pressures, the influence of collision-induced effects including pressure broadening and line mixing on the spontaneous Raman spectrum is expected to be significant [50]. Additionally, if the instrument linewidth was narrower than for these experiments, the single Lorentzian lineshape model may no longer be sufficient. Therefore, further experiments are required to investigate the collision-induced effects on the ro-vibrational spontaneous Raman scattering from nitrogen over the entire range of pressures expected to be encountered in a gas turbine engine. This is the motivation for the experiments presented in the next chapter.

3.4 Temperature Measurement Verification

Before proceeding to high pressure experiments, investigating the accuracy and precision of spontaneous Raman thermometry at lower pressures will be beneficial for assessing the strengths and weaknesses of this technique. The approach to verify these temperature measurements was to use spontaneous Raman scattering to measure temperature on a well-characterized burner. By comparing the spontaneous Raman temperature measurements to reference temperatures for this burner, we can gain insight into the accuracy and precision of this technique.

3.4.1 Experimental Setup

The well-characterized burner consisted of an inner region through which a mixture of CH_4 and air flowed, surrounded by an outer coflow region through which N_2 flowed. Each gas was controlled by an individual mass flow controller. The laser and optics used for these spontaneous Raman scattering measurements were the same as in the experiments discussed above. A detailed description of the laser, spectrograph, and side-scattering configuration can be found in Section 3.1. Figure 3.11 shows a photograph of the verification burner with a lean flame and the Raman scattering experiment in place.

Temperature measurements were recorded on the burner centerline, 30 mm from the burner surface at 9 different equivalence ratios. Table 3.1 shows the methane and air flowrates of the 9 conditions along with the corresponding equivalence ratios. Each gas was supplied from a gas cylinder at room temperature. The flowrates were controlled using 100 slpm mass flow controllers. The mass flow controllers have an uncertainty of 0.8% of the reading plus 0.2% of the full scale. The uncertainties in the flowrates are included in Table 3.1. The corresponding uncertainties in the equivalence ratio due to the uncertainties in the flowrates are also included in Table 3.1. Perfectly premixed conditions were assumed for the equivalence ratio calculations.

Because the methane flowrate was small compared to the full scale of the mass flow controllers, the resulting uncertainty in the equivalence ratio was significant. We believe this uncertainty in setting the equivalence ratio of the flame dominates the overall uncertainty in the temperature measurement.

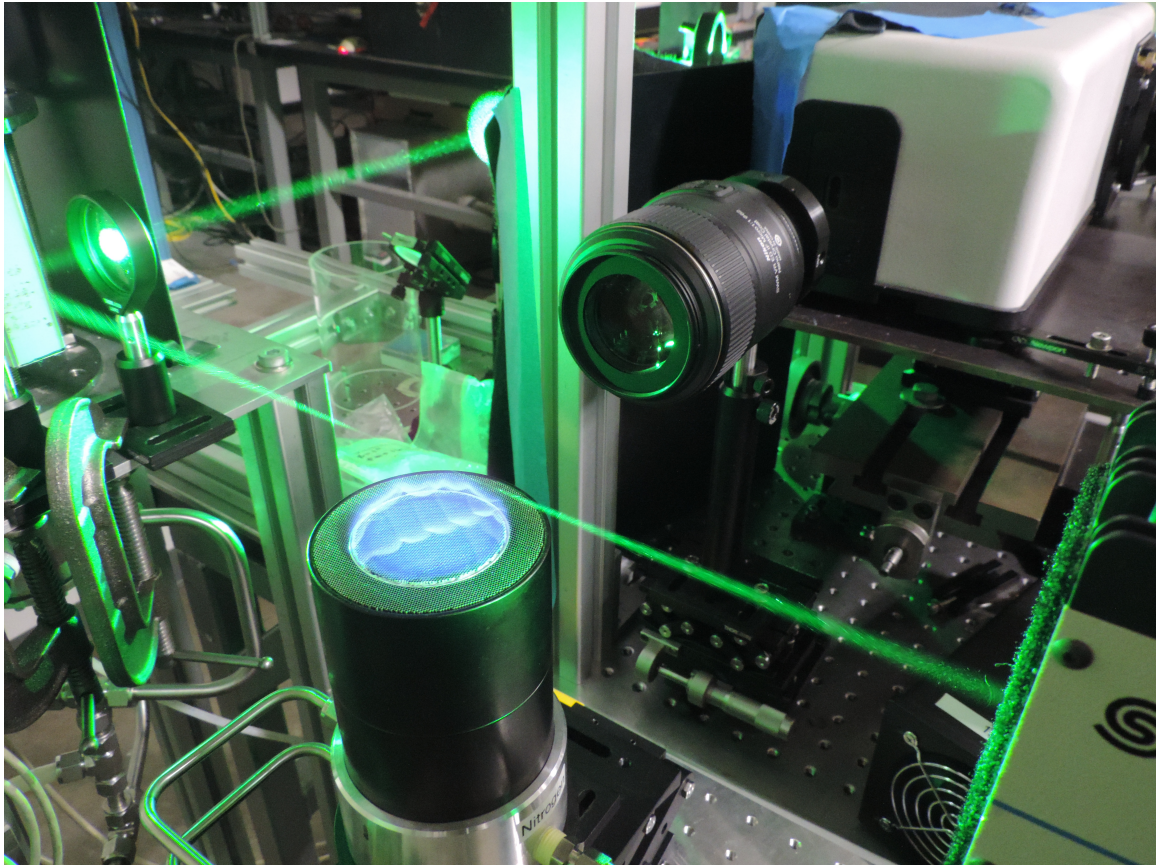


Figure 3.11: Photograph of the verification burner with a lean flame and the setup of the spontaneous Raman scattering experiment.

Table 3.1: Summary of experimental conditions and calculated equivalence ratios.

Condition	Air Flowrate (slpm)	CH ₄ Flowrate (slpm)	Equivalence Ratio
1	45.0 ± 0.6	3.89 ± 0.23	0.820 ± 0.059
2	45.0 ± 0.6	4.12 ± 0.23	0.868 ± 0.061
3	45.0 ± 0.6	4.34 ± 0.23	0.914 ± 0.062
4	45.0 ± 0.6	4.57 ± 0.24	0.963 ± 0.062
5	45.0 ± 0.6	4.79 ± 0.24	1.009 ± 0.064
6	45.0 ± 0.6	5.12 ± 0.24	1.079 ± 0.065
7	45.0 ± 0.6	5.46 ± 0.24	1.150 ± 0.067
8	40.9 ± 0.5	5.16 ± 0.24	1.196 ± 0.072
9	28.5 ± 0.4	3.83 ± 0.23	1.274 ± 0.098

3.4.2 Temperature Measurement Results

Five spontaneous Raman spectra were recorded for every flame condition, each with a collection time of 60 s. The spontaneous Raman spectra were then fit for temperature. Table 3.2 shows the mean temperature for each condition. The uncertainty in the measured temperatures in Table 3.2 represents the precision uncertainty (95 % confidence) based on the 5 repeated runs for each flame condition. Also included in Table 3.2 is the reference temperature for each condition. The reference temperature was established by N₂ coherent anti-Stokes Raman scattering (CARS), using methods described in Driscoll et al. [89]. From these CARS measurements, the temperature was found to be 35 K below the adiabatic flame temperature with an overall uncertainty of ±30 K [16].

To further visualize the comparison between the spontaneous Raman scattering measurements and the reference temperatures, the results in Table 3.2 are plotted in

Table 3.2: Summary of temperature verification experimental results.

Condition	Equivalence Ratio	Measured Temperature (K)	Reference Temperature (K) [16]
1	0.820 ± 0.059	2005 ± 11	1995 ± 30
2	0.868 ± 0.061	2058 ± 9	2062 ± 30
3	0.914 ± 0.062	2113 ± 7	2120 ± 30
4	0.963 ± 0.062	2161 ± 22	2169 ± 30
5	1.009 ± 0.064	2192 ± 13	2198 ± 30
6	1.079 ± 0.065	2177 ± 18	2192 ± 30
7	1.150 ± 0.067	2120 ± 13	2144 ± 30
8	1.196 ± 0.072	2081 ± 15	2109 ± 30
9	1.274 ± 0.098	2005 ± 16	2047 ± 30

Figure 3.12. The uncertainty in the temperature is plotted as vertical error bars while the horizontal error bars represent the uncertainty in the equivalence ratios. Cantera was used for the adiabatic flame temperature calculations. All the data presented in Table 3.2 and Figure 3.12 were recorded on the same day, minimizing fluctuations in room temperature and humidity. The measured temperatures agree with the reference temperatures to within the uncertainty for every equivalence ratio. For the lean experimental conditions, the measured temperatures are closer to the adiabatic temperature curve as compared to the rich experimental conditions, which suggests that the true equivalence ratios for the spontaneous Raman measurements were slightly higher than the intended run conditions.

From these results, we conclude that the spontaneous Raman scattering temperature measurements technique has a precision of approximately ± 15 K, which

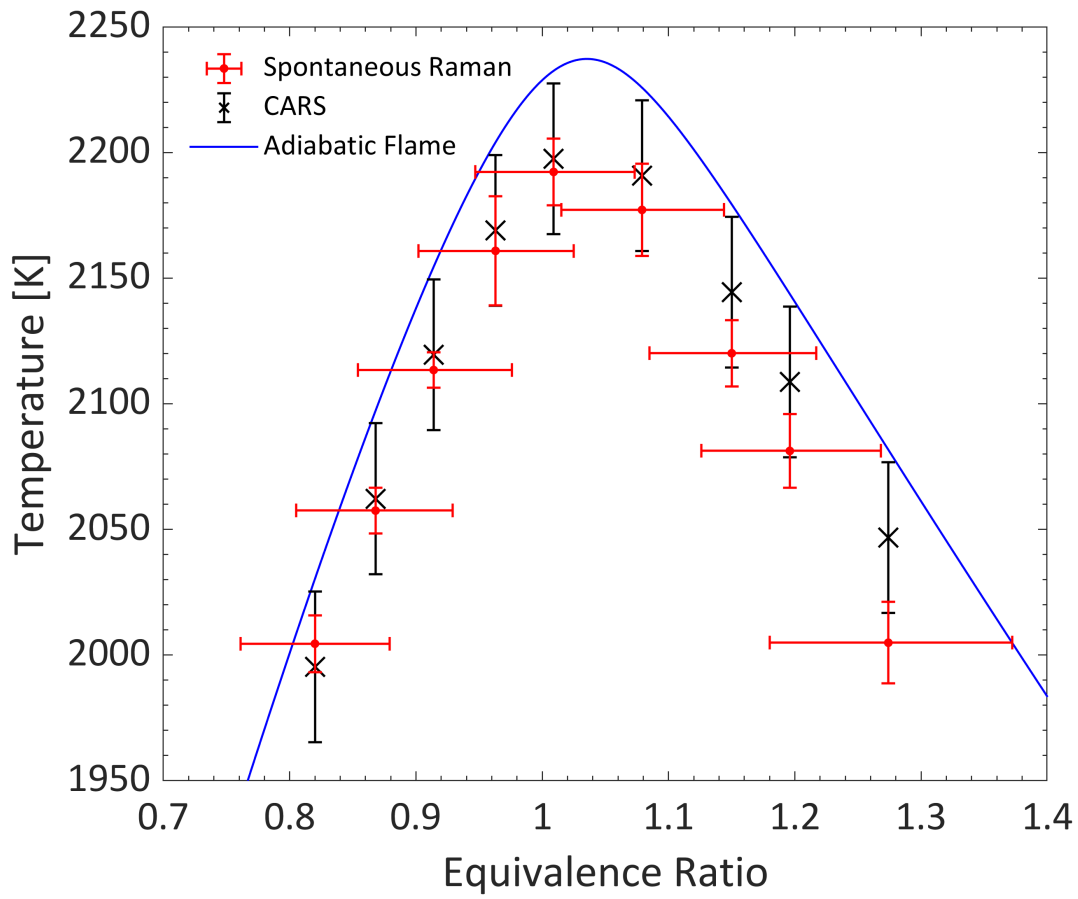


Figure 3.12: Temperature versus equivalence ratio for the verification burner

corresponds to $\pm 0.7\%$ at 2100 K. We also conclude that the accuracy of this spontaneous Raman thermometry is at least as good as the accuracy of the N₂ CARS temperature measurement technique used to establish the reference temperatures on this burner. The precision of the spontaneous Raman thermometry is most likely dominated by the signal-to-noise ratio in the Raman spectra, which can be improved by higher laser power, longer integration times, a multiple-pass cell, or higher number density. Therefore the precision uncertainty of ± 15 K could be improved if necessary, but it may also worsen if the Raman signal was weaker in a particular application. The accuracy of spontaneous Raman thermometry relies on the accuracy of the spontaneous Raman simulations because it is based on a direct fit of the model to the experimental ro-vibrational Raman spectrum. We believe this technique is very accurate because of the ability of the high-fidelity Raman simulations to represent the experimental spectra, at least at atmospheric pressure. However, as the collision-induced effects of rotational-number dependent pressure broadening and line mixing become more important with increasing gas density, the accuracy of this spontaneous Raman thermometry could be questioned because these atmospheric pressure Raman simulations do not include account for these collision-induced effects. Therefore, detailed experiments studying the influence of these collision-induced effects on the N₂ ro-vibrational spontaneous Raman spectrum are necessary to maintain the accuracy of spontaneous Raman thermometry in high pressure gases.

Chapter 4

Measurements of Pressure Broadening in the Anisotropic Tensor Component

This chapter presents an investigation of high density effects on ro-vibrational spontaneous Raman scattering, which must be understood to obtain accurate thermometry in high pressure gases using high-fidelity Raman simulations. Spontaneous Raman spectra from room temperature nitrogen were recorded over the pressure range of 10 atm to 70 atm for three gas compositions: pure nitrogen, air, and nitrogen in argon. The analysis of these spectra focused on the anisotropic tensor component of ro-vibrational spontaneous Raman scattering. The O and S branches consist entirely of the anisotropic component, while the Q branch has an isotropic contribution and an anisotropic contribution [1]. High pressure models have been developed for the isotropic component of Raman scattering, such as the Modified Exponential Gap (MEG) line mixing model [61, 65]. This model uses parameters and line broadening coefficients that have been measured by experiments [66, 67, 68]. However, theory indicates that broadening coefficients and relaxation cross-sections for isotropic Raman scattering are different than those for anisotropic Raman scattering

Portions of this chapter previously appeared in the following publication:

Haller, T. W. and Varghese, P. L., “Measurements of pressure broadening of N₂ in the anisotropic tensor component of spontaneous Raman spectra,” *Combustion and Flame*, vol. 224, pp. 166–176, 2021. DOI: 10.1016/j.combustflame.2020.11.045.

The dissertator contributed to this publication through design and conduct of the research, data analysis and interpretation, and writing of the manuscript.

[72, 73, 74]. Therefore, accurate spontaneous Raman thermometry in high pressure gases requires experiments to record ro-vibrational spontaneous Raman spectra at high enough densities and with sufficient spectral resolution to measure the pressure-broadened linewidths of the anisotropic tensor component. Sections 4.2 and 4.3 previously appeared in [90].

4.1 Experimental Setup

A pressure chamber was constructed using a commercially available 2 inch (approximately 51 mm) NPT pipe cross, with 3 sight windows each fused into an NPT housing, and 1 NPT plug with 3 access ports drilled into it. The commercially available sight windows were made of soda lime glass and had a clear aperture of 36 mm. The 3 sight windows provided good optical access into the chamber, allowing for spontaneous Raman experiments in the forward, side, or back scattering configurations. The maximum operating pressure of the chamber was set to about 70 atm (1 atm = 0.101 MPa), and the chamber was hydrostatically tested up to a pressure of 105 atm. The 3 access ports in the NPT plug were used for a gas fill line, a gas exit line, and a thermocouple port to measure the temperature of the gas at the center of the pressure chamber. Figure 4.1 shows an isometric view of the pressure chamber.

For safety purposes, the pressure chamber needed to be operated remotely. To do this, a gas transfer system was constructed that could fill the chamber with gas from two separate gas cylinders and empty the chamber without the user entering the room. The two gas cylinders were necessary to create a gas mixture with known mixture fractions in the pressure chamber. Figure 4.2 shows a diagram of this gas transfer system.

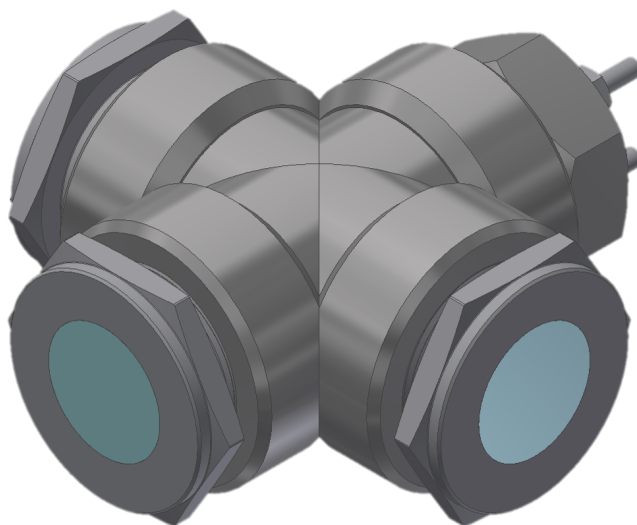


Figure 4.1: Isometric view of the pressure chamber.

Pneumatically activated valves were located immediately upstream and downstream of the pressure chamber. These control valves, operated by air supplied from a gas cylinder, sealed the supply and exit lines of the pressure chamber. There was no gas flow through the chamber while collecting a spontaneous Raman spectrum, which ensured there were no temperature gradients within the chamber. The pneumatic valve upstream of the pressure chamber was a normally-closed valve, and the pneumatic valve downstream of the chamber was a normally-open valve. This configuration guaranteed that the pressure chamber would be safely emptied if there was power failure in the system.

At high pressure differentials, such as those encountered in this gas transfer system, solenoid valves leak gas a small amount of gas through them. Therefore, the pneumatically activated valves were used to definitively seal the entry and exit of the chamber during experiments. However, as seen in Figure 4.2, a solenoid valve was included on the fill line from the two gas cylinders used to fill the chamber. If

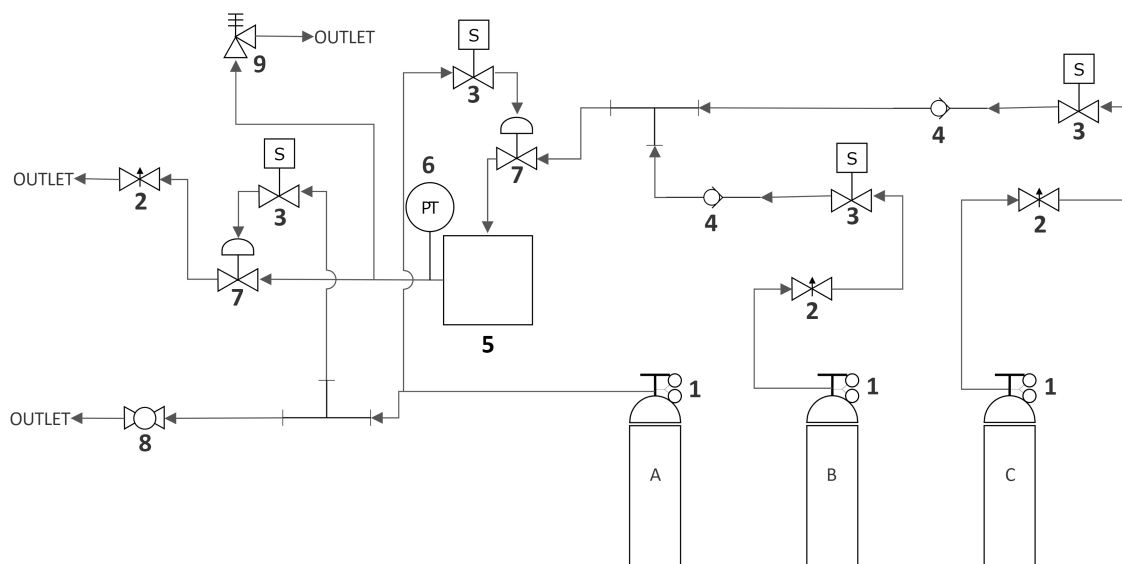


Figure 4.2: Piping and Instrumentation Diagram. 1, Gas Cylinder; 2, Needle Valve; 3, Solenoid Control Valve; 4, Check Valve; 5, Pressure Chamber; 6, Pressure Transducer; 7, Pneumatic Control Valve; 8, Ball Valve; 9, Pressure Relief Valve.

the chamber was filled with gas from just one cylinder, such as pure nitrogen or air, then the solenoid valve remained open. If the chamber was filled with a gas mixture, the solenoid valves controlled which cylinder was filling the chamber. A specific gas mixture in the chamber was achieved by setting each gas bottle regulator to the desired partial pressure for each gas component of the mixture. Then the chamber was filled by opening the solenoid valves one at a time. Once the chamber reached the maximum pressure for the experiment, the upstream pneumatic valve was closed which sealed the chamber and fixed the gas mixture fractions for the duration of the experiment. To account for the small leak rate through the solenoids, a directional check valve was installed close to the exit of each solenoid valve. This check valve prevented gas in one fill line from moving upstream through a solenoid valve and contaminating the fill line of the other gas. There would still be a small leak rate

downstream through a solenoid valve if the partial pressures set by the gas bottle regulators differed significantly. However, this leak rate had little to no effect on the overall mixture fraction in the chamber because pneumatic valve did not allow any leaking downstream into the chamber.

Needle valves were installed upstream and downstream of the pressure chamber to reduce the flowrate as the chamber was filled and emptied. A pressure relief valve was included in the system and set to a relief pressure of 86 atm, which is above the maximum experiment pressure but below the hydrostatic test pressure. Remote operation of the gas transfer system in Figure 4.2 was made possible by the solenoid valves, which were controlled by electric current supplied by a switch box in the adjacent control room. Solenoid valves controlled the fill lines from the gas cylinders, as discussed above, as well as the pilot lines to the pneumatically activated valves. So the solenoids give the user complete control over the operation of the pressure chamber. The Standard Operating Procedure for this High Pressure Raman Spectroscopy Experiment is included in Appendix B.

The gas pressure in the pressure chamber was measured with an Omega PX309-1KGV pressure transducer with an accuracy of $\pm 0.25\%$ of the measurement value (combined linearity, hysteresis, and repeatability). The temperature in the chamber was measured with a Type-K thermocouple located near the center of the chamber. Security cameras were used to visually monitor the experiment remotely.

The laser source for the spontaneous Raman scattering measurements was a frequency doubled Nd:YAG laser (532 nm) with a pulse-energy of 6 mJ and a repetition rate of 100 Hz. The spontaneous Raman signal was collected in the forward scattering configuration, as shown in Figure 4.3. Forward scattering is advantageous

for this experiment because this configuration maximizes the collection volume along the beam path within the pressure chamber, which is at constant conditions. The laser was focused into the pressure chamber using an AR coated, plano-convex lens with a focal length of 300 mm. Two dichroic mirrors with a reflectivity of 99.9% at 532 nm were used to filter the laser beam after it passed through the chamber while allowing the forward scattering Raman signal to be transmitted. The Raman signal was collected using a 62 mm diameter Nikon lens, located downstream of the dichroic mirrors. The collected light was focused into an f/1.8 imaging spectrograph from Kaiser Optical Systems, equipped with an additional holographic notch filter to remove any remaining laser light, and a high dispersion holographic transmission grating (HDG-607). The system has an average linear dispersion of $0.94 \text{ cm}^{-1}/\text{pixel}$ when used in conjunction with a PI-MAX 3 ICCD camera from Princeton Instruments that has $26 \mu\text{m}$ pixels. The spectrometer entrance slit size for all experiments was $25 \mu\text{m}$ to give the best spectral resolution (approximately 2.5 cm^{-1}) of the recorded Raman spectra.

4.2 Procedure

4.2.1 Experimental

The nitrogen ro-vibrational Stokes spontaneous Raman spectrum was recorded over a range of pressures up to a maximum pressure of 70 atm for three gas mixtures: 100% nitrogen, 100% dry air, and 20% nitrogen + 80% argon. The gases, supplied by Praxair, had a guaranteed purity of at least 99.998% and a maximum water concentration of 3 ppm by volume. The nitrogen-argon gas mixture was made by combining nitrogen and argon in the pressure chamber at the appropriate partial pressures. The spontaneous Raman spectra were all recorded in the same mixture

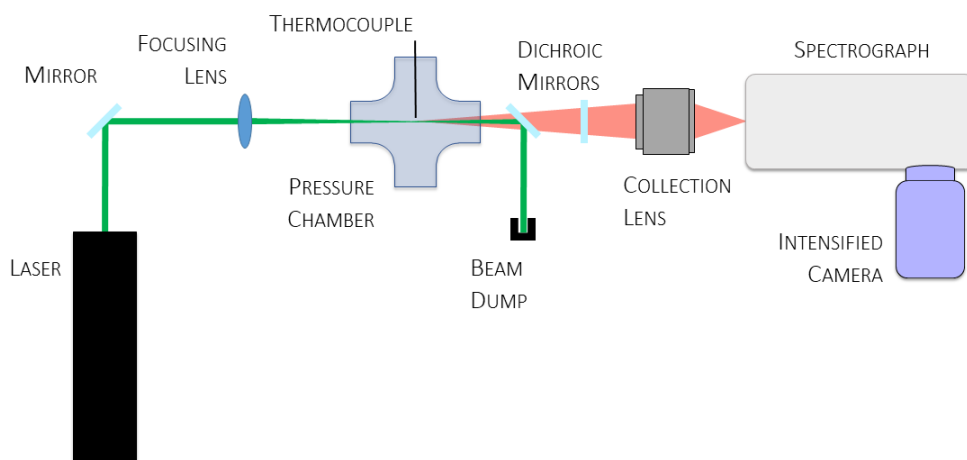


Figure 4.3: Schematic diagram of the forward scattering experiment.

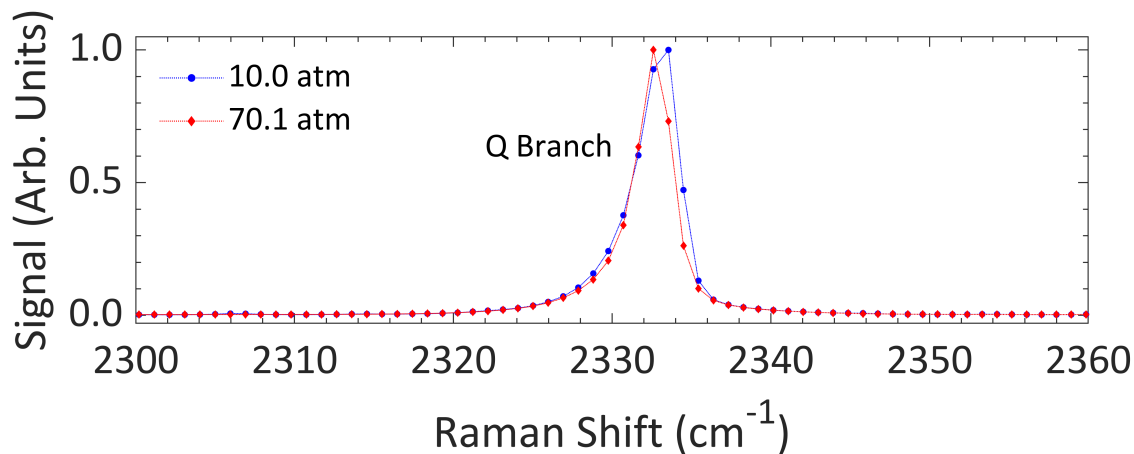
beginning with the highest pressure to ensure that the gas composition was identical for all spectra. The gas temperature in the pressure chamber was 300 ± 1 K for all experiments as recorded by a type K thermocouple inserted via a feed through with the thermocouple junction located above the laser beam near the center of the cell. For the pure nitrogen mixture, the Raman signal was collected from 36,000 laser pulses (216 J total laser fluence), and for the other two mixtures, the Raman signal was collected from 54,000 (324 J total laser fluence) laser pulses. The intensified camera was gated around each laser pulse, and the CCD was exposed to several laser pulses, collecting the Raman signal on chip, before periodically reading out the signal to integrate it in software. The number of laser pulses integrated on the CCD before read out varied from 90 to 2700 pulses, depending on the signal-to-noise ratio, which scales linearly with the partial pressure of nitrogen. Figure 4.4 shows

a comparison between nitrogen Raman spectra collected in pure nitrogen at 10 atm and 70 atm. Figure 4.4a shows that at 70 atm, the Q branch has narrowed slightly due to line mixing (so-called pressure narrowing) effects [50, 58, 61, 68, 73] while Figure 4.4b shows that the O and S branch lines show significant pressure broadening. The Q branch of the rare nitrogen isotopologue $^{15}\text{N}^{14}\text{N}$, which constitutes 0.725% of naturally occurring N_2 , becomes more pronounced in the 70 atm spectrum because it also narrows with increasing density while the nearby O branch lines broaden. Note that line mixing or pressure narrowing effects are expected to be more significant in the spectrum of $^{15}\text{N}^{14}\text{N}$ because it is a heteronuclear diatomic and hence transitions between even and odd rotational states are not prohibited by nuclear spin symmetry restrictions. Figure 4.4 demonstrates that the isotropic component of the spectrum, which dominates the Q branch, behaves differently than the anisotropic O and S branches with increasing density.

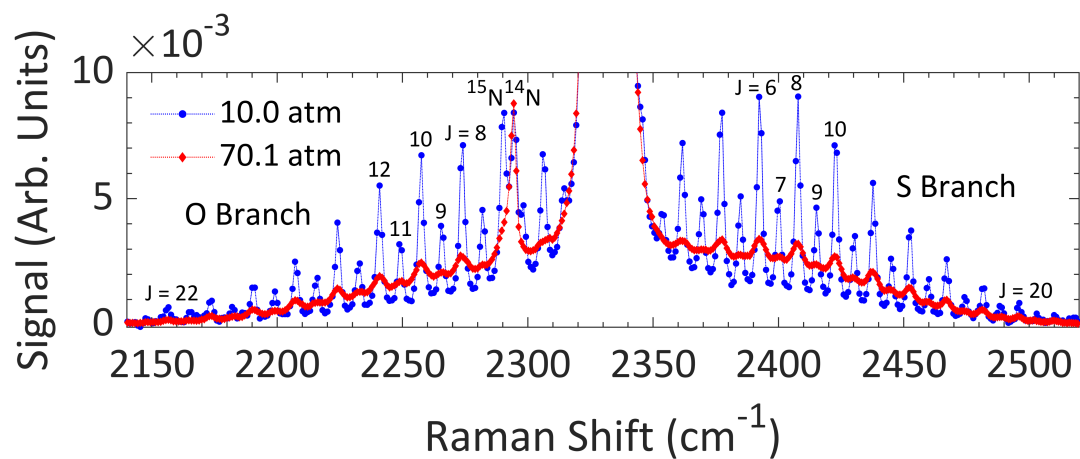
4.2.2 Data Analysis

To analyze the line broadening of the anisotropic component of the spectrum the O and S branches were fit for linewidths using a high-fidelity spontaneous Raman scattering simulation code developed at The University of Texas at Austin for ro-vibrational Stokes scattering from nitrogen [51] and also briefly described in Chapter 2. The model does not include line mixing and systematic departures of the observed spectra from the model are interpreted as indications of line mixing effects.

The lineshape function (F_{eff}) used when simulating and fitting observed spectra was taken to be a convolution of an instrument lineshape function (F_{inst}) and a molecular line shape function (F_{mol}). The instrument lineshape was assumed to be a convolution of a trapezoid function $T(\lambda; b, t)$ and a Lorentzian $L(\lambda; \Delta\lambda_{inst})$, so



(a)



(b)

Figure 4.4: Comparison between nitrogen Raman spectra recorded in pure nitrogen at 10 atm and 70.1 atm. (a) Recorded spectra in the Q branch region scaled to unit maximum intensity. (b) Spectra over an extended frequency range with vertical scale magnified 100 times to show rotational structure from O and S branches of the dominant $^{14}\text{N}_2$ isotopologue and the Q branch of the $^{15}\text{N}^{14}\text{N}$ isotopologue.

$F_{inst}(\lambda; b, t, \Delta\lambda_{inst}) = T(\lambda; b, t) * L(\lambda; \Delta\lambda_{inst})$. Here b, t correspond to the trapezoid base and tip halfwidths respectively, and $\Delta\lambda_{inst}$ is the instrument Lorentz halfwidth (half width at half maximum). Fits to a neon lamp spectrum were used to determine the instrument lineshape parameters, assuming that the linewidths of the atomic lines were negligible. The molecular lineshape was assumed to be a Lorentzian because Doppler broadening at room temperature is negligible relative to collision broadening for the pressure ranges studied experimentally (10 atm to 70 atm), i.e. $F_{mol} = L(\lambda; \Delta\lambda_{mol})$. Because the convolution process is associative, and the convolution of two Lorentzians is another Lorentzian whose halfwidth is the sum of the individual halfwidths, the effective recorded lineshape is simulated as

$$\begin{aligned}
F_{eff}(\lambda; b, t, \Delta\lambda_{eff}) &= F_{inst}(\lambda; b, t, \Delta\lambda_{inst}) \\
&= T(\lambda; b, t) * L(\lambda; \Delta\lambda_{inst}) * L(\lambda; \Delta\lambda_{mol}) \\
&= T(\lambda; b, t) * L(\lambda; \Delta\lambda_{inst} + \Delta\lambda_{mol}) \\
&= T(\lambda; b, t) * L(\lambda; \Delta\lambda_{eff})
\end{aligned} \tag{4.1}$$

Therefore, the recorded O and S branch lines were fit for the effective Lorentzian halfwidth using a Levenberg-Marquardt algorithm to minimize the square error, using the experimentally determined trapezoid parameters, and the known experimental temperature. As noted above, this simulated spontaneous Raman spectral model does not include the effects of line-mixing, which is certainly significant for the isotropic scattering component in the Q branch, and for which we see evidence in the recorded spectra, even though the Q branch is not well resolved (Figure 4.4a). Therefore, the experimental data was cropped to mask the Q branch and the fit was only conducted on the portion of the spectrum where the purely anisotropic contribution dominates. Thus only the O and S branches were fit for linewidths. We know on theoretical grounds that the anisotropic lines are decoupled from the isotropic lines [73, 51].

The mixing of the anisotropic spectrum simultaneously couples lines in the O, Q, and S branches, but mixing in the anisotropic component was not included in the model. Thus this model assumes that the anisotropic contribution to the Q branch is also unmixed, i.e. it is computed as a superposition of unmixed lines. The validity of this approximation is not directly tested because the portion of the spectrum in the Q branch region is excluded during the fit. If this assumption is invalid we might expect to find small systematic distortions in the fit residual which should be the purely isotropic portion of the scattering signal. The distortion would be small because the isotropic tensor scattering component is much stronger than the anisotropic scattering.

Because the line broadening is dependent on rotational quantum number, each line has a unique Lorentzian width. However, the linewidths of the branches can be related to each other by assigning M values to the lines as follows [73]:

$$\begin{aligned}
 M &= J - 1 \text{ (O branch),} \\
 M &= J \text{ (Q branch),} \\
 M &= J + 1 \text{ (S branch),}
 \end{aligned}
 \tag{4.2}$$

for all positive integer M values. So a unique Lorentzian width can be assigned for every M value according to the formulation of Equation (4.2). For example, in our fits the width of the O(11) line is constrained to be the same as that of the S(9) line ($M = 10$ for both).

4.3 Pressure Broadening in the Anisotropic Component

Figure 4.5 shows representative fits to the O and S branches for Lorentzian widths over the pressure range studied experimentally. Solid circles are the experi-

mental data and the line is the corresponding fitted spectrum. The residual error in the fit is plotted at the bottom of each figure. Note that each spectrum is scaled as in Figure 4.4, so that the peak of the strong isotropic Q branch is at unity. Thus the peak intensity of the O and S branch transitions is less than 1% of the peak Raman signal intensity. The simulation model for the fits in Figure 4.5 only contains contributions from the anisotropic scattering.

Figure 4.6a shows the rms of the residual errors for the fits to all pressures and gas mixtures on the left axis. The right axis of Figure 4.6a shows the mean signal-to-noise ratio for every pressure, calculated as the mean intensity of the O and S branch data points used in the fit divided by the rms of the residual error. In Figure 4.6b the same data are plotted as a function of nitrogen partial pressure. The fits match the experimental data well over the entire pressure range. If line mixing effects were significant at high pressures we would expect to see increasing residual error at high pressure because of systematic departures of the experimental spectra from the model spectrum that neglects line mixing. However Figure 4.6 shows that the rms of the residual errors decreases continuously with increasing pressure for all three mixtures indicating that the model neglecting line mixing effects is satisfactory for the O and S branches for the entire pressure range investigated. The rms of the residual errors in the fits is less than 5% of the mean O and S branch intensity for the spectrum recorded in pure nitrogen at 22 atm and less than 3% at 49 atm.

The mean signal-to-noise ratio is also plotted in Figure 4.6 for 3 mixtures. The mean signal-to-noise (SNR) ratio is calculated as the mean intensity of the O and S branch data points used in the fit divided by the rms of the residual errors. The rms error decreases and the SNR increases with pressure because of the increased density of

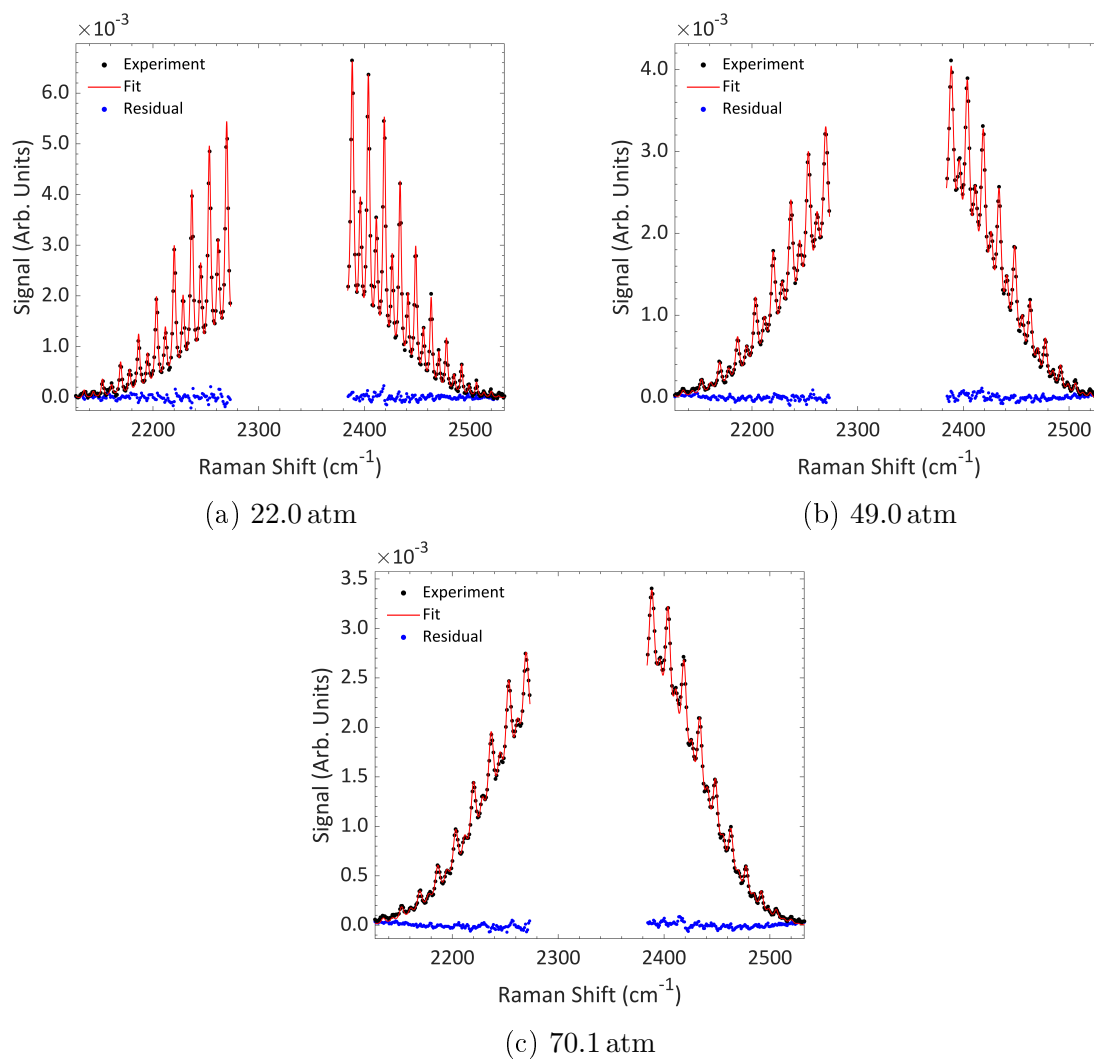


Figure 4.5: Fits to anisotropic component of nitrogen Raman spectra recorded in 100% nitrogen.

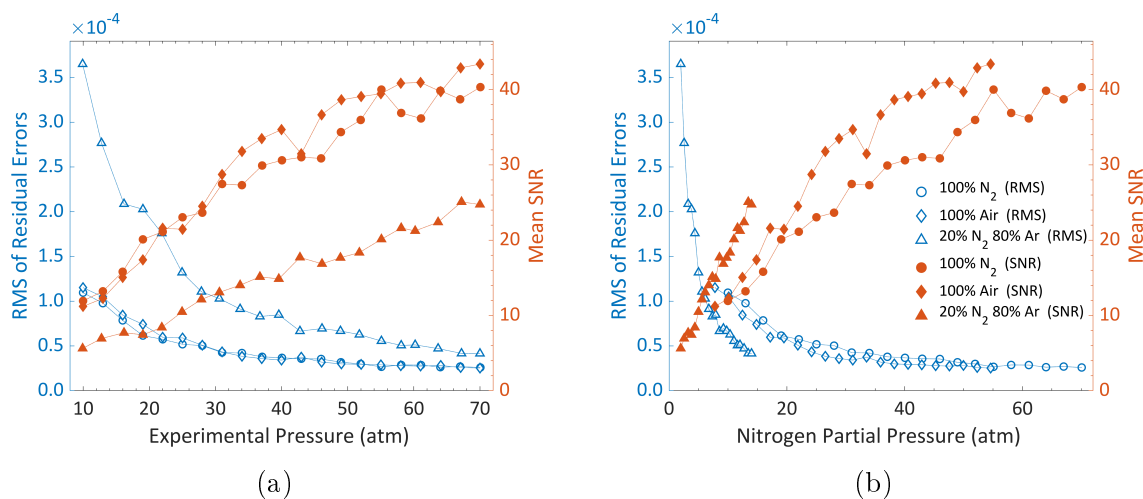


Figure 4.6: (a) The root mean square of the residual errors for the fits to anisotropic Raman spectra of nitrogen (left axis) and the mean signal-to-noise ratio (right axis) plotted as a function of the total pressure. (b) Same data plotted as a function of nitrogen partial pressure. The symbols shown in the legend also apply to (a)

N₂ in the probe volume for fixed mixture composition. The rms of the residual errors in fits to the nitrogen Raman spectra recorded in the 20-80 nitrogen-argon mixture is larger than the other gas mixtures, which can be explained by a poorer signal-to-noise ratio due to the reduced density of nitrogen in the measurement volume. Figure 4.6b compares the rms of the residual errors and SNR of the measurements for the different gas compositions at the same nitrogen partial pressure. Two factors affect the observed difference in the rms error at the same partial pressure: (1) the total laser fluence, i.e. the number of laser pulses, for the recorded spectrum, and (2) the line broadening. Comparing the Ar-N₂ measurements with the air measurements that were made with the same total laser fluence (54,000 laser pulses), we see that the measurements in Ar-N₂ data have lower rms and higher SNR than air at the same nitrogen partial pressure. This is because the pressure broadening of N₂ in Ar mixtures is smaller than the pressure broadening of N₂ in air (see Table 4.1

below) so the recorded lines are more clearly defined and lifted above the readout and shot noise resulting in lower rms and higher SNR. Comparing the pure N₂ and N₂ in air results, we see two competing effects. The air broadening is higher than in pure N₂ (see Table 4.1 below), which would tend to increase the rms error and reduce SNR, but the higher total laser fluence used in the air experiments (54,000 laser pulses vs 36,000 laser pulses) raises the signal above the noise and reduces rms residual error and increases SNR. The net results of these two competing effects is a slight reduction of rms error and increased SNR for the N₂ in air data.

In summary, Figure 4.6 shows that the unmixed line model for the anisotropic spectrum successfully matches the experimental data at the highest pressures, indicating that there are no significant line mixing effects in the O and S branches up to 70 atm to within the precision and spectral resolution of our measurements and fitting procedure.

For M values less than 7 (O(8), S(6)), fitted Lorentzian widths could not be obtained with a model that contains only anisotropic lines because the isotropic scattering contribution is significant at these Raman shifts. Figure 4.7 shows the fitted Lorentzian widths plotted versus pressure for the available M values.

If there are no line mixing effects, then the Lorentzian widths should increase linearly with pressure and when this linear trend is extrapolated to zero pressure, then the Lorentzian linewidths should be identical for every M and equal to the instrument contribution to the Lorentzian linewidth. Figure 4.7 shows linear regression fits to the Lorentzian widths for every M at pressures of 22 atm and above for the pure nitrogen and air mixtures and at pressures of 34 atm and above for the 20-80 nitrogen-argon mixture. These limits are shown by the dashed vertical lines in Figure 4.7. We

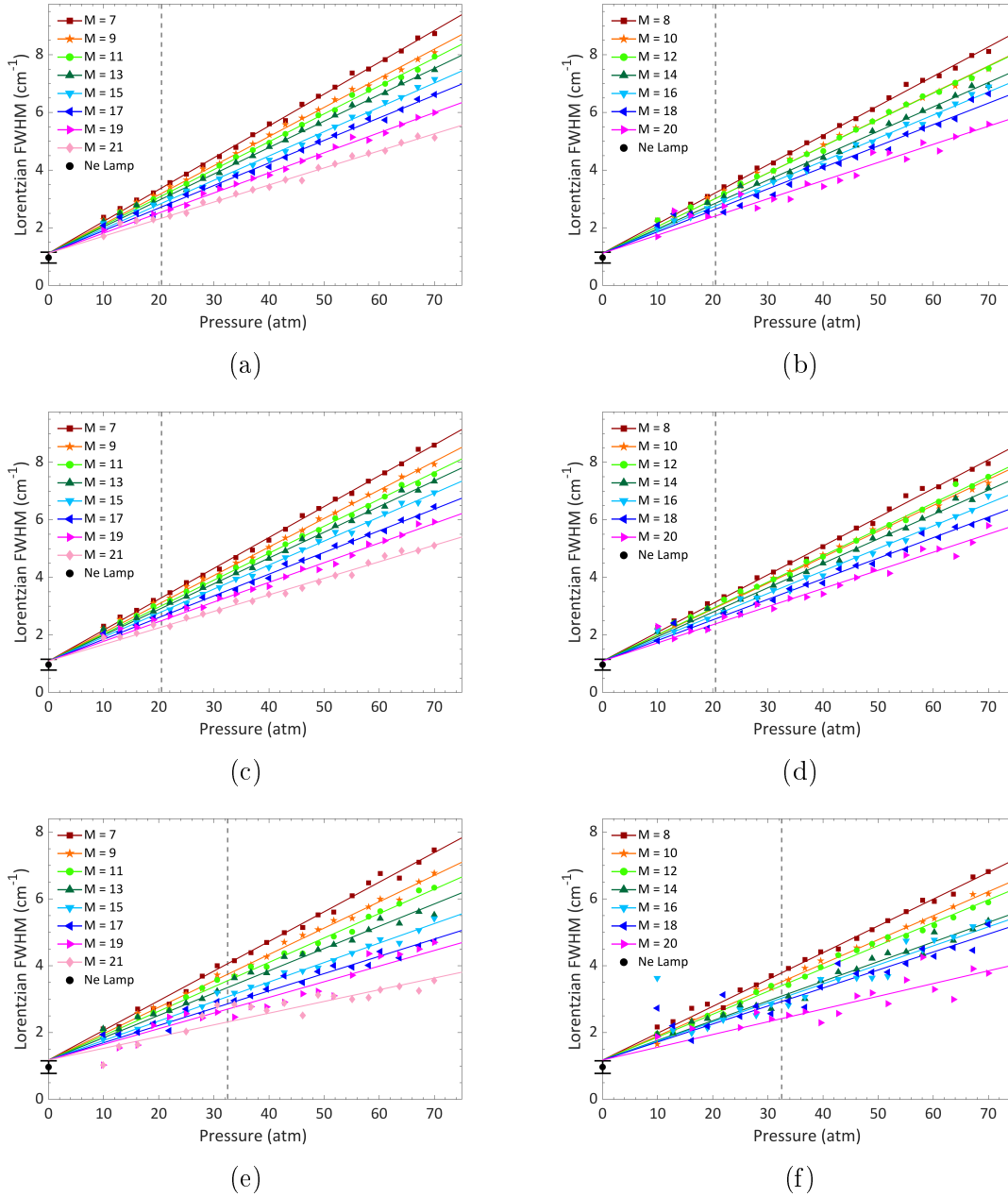


Figure 4.7: Lorentzian widths obtained from fits to anisotropic nitrogen Raman spectra recorded in (a) 100% N₂, (b) 100% air, and (c) 20% N₂ + 80% Ar. A linear regression is applied to the results for every M , with a common intercept at 0 atm. A vertical dashed line bounds the minimum experiment pressure used for the linear regression. The intercept represents the instrument contribution to the Lorentzian width, and it is compared to the Lorentzian width obtained from fits to neon lamp spectral lines.

restricted the fits to data in this range because the residual error in the fits was small ($\text{SNR} > 20$) for recorded spectra in both pure nitrogen and air. For the 20-80 nitrogen-argon mixture, a higher rms of residual errors had to be tolerated; the fits included in the linear regressions for the nitrogen-argon mixture had $\text{SNR} > 14$. Each linear regression has a unique slope parameter but they were all constrained to have a common intercept at zero pressure. This is consistent with our model for inferred Lorentzian halfwidth,

$$\lim_{p \rightarrow 0} \Delta\lambda_{eff} = \Delta\lambda_{inst}, \quad (4.3)$$

since the contribution of pressure broadening vanishes as the pressure drops to zero. As can be seen from Figure 4.7 the measurements agree quite well with this model. For every gas mixture, the zero pressure limit of the Lorentzian fullwidths ($1.1 \pm 0.2 \text{ cm}^{-1}$, $1.1 \pm 0.2 \text{ cm}^{-1}$, $1.2 \pm 0.6 \text{ cm}^{-1}$ for 100 % nitrogen, 100 % air, and 20 % nitrogen + 80 % argon respectively) is in reasonably good agreement with the instrument Lorentzian fullwidth ($1.0 \pm 0.2 \text{ cm}^{-1}$) obtained from fits to 6 neon spectral lines recorded using a neon lamp. Doppler broadening is neglected from this analysis because the Doppler half width at half maximum for forward scattering at room temperature is $5.5 \times 10^{-2} \text{ cm}^{-1}$, which is negligible compared to either the instrument or the collision broadened linewidth. Figure 4.8 shows fits to neon spectral lines which were used to determine the instrument parameters. The residual error in these fits is also plotted in Figure 4.8.

For the anisotropic data recorded at pressures below 22 atm, the fitted Lorentzian widths diverge from the linear regressions shown in Figure 4.7. The poorer fit at lower pressures can be explained by the reduced signal-to-noise ratio due to lower spontaneous Raman signal which, in our experiments, scales linearly with pressure. For

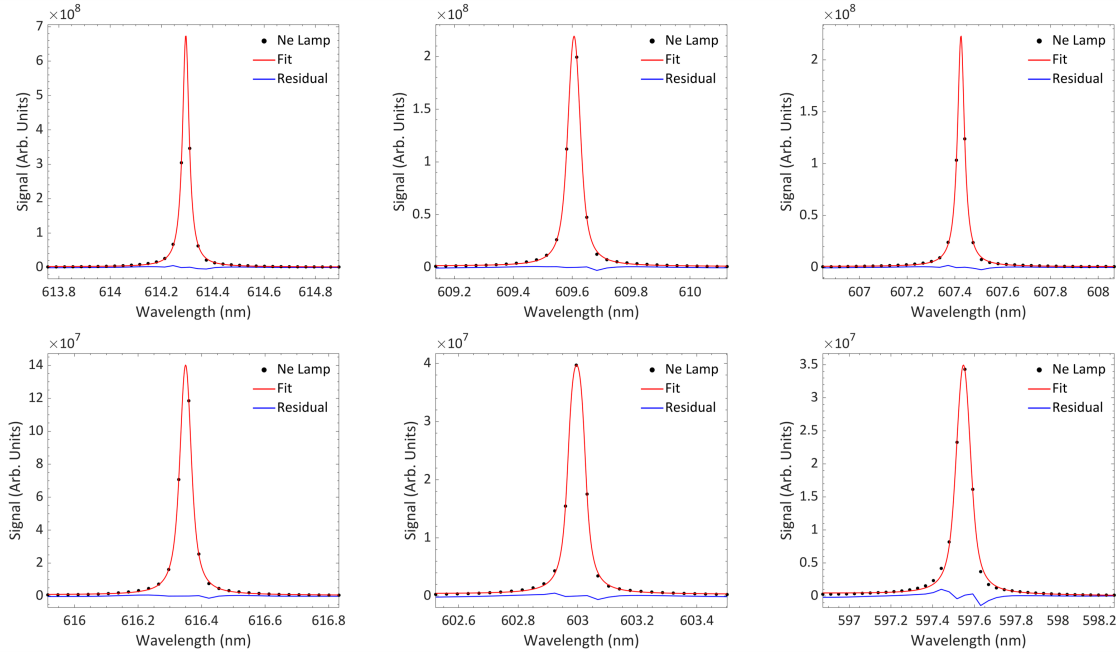


Figure 4.8: Fits to 6 neon spectral lines recorded using a neon lamp. These fits were used to determine the instrument lineshape parameters.

experiments at pressures lower than 22 atm, the data are more noisy and just a small amount of noise in the spectrum corrupts the measurements of linewidths of the weak anisotropic lines that are typically only 1% of the peak Raman signal intensity.

The slopes of the linear regressions in Figure 4.7 represent the line broadening coefficient for the given M value. The Lorentzian widths measured in nm are converted to equivalent broadening coefficients in wavenumbers using $|\Delta\omega|/\omega = \Delta\lambda/\lambda$ and noting that $\omega[\text{cm}^{-1}] = 10^7/\lambda[\text{nm}]$. Figure 4.9a shows a comparison of these nitrogen self-broadening line broadening coefficients to those used to generate the modified exponential gap (MEG) model [61] commonly used to simulate CARS spectra. It should be noted that the anisotropic contribution to CARS spectra is very weak because the CARS matrix elements go as the square of the susceptibility. Thus a 1% anisotropic contribution to the spontaneous Raman signal is a 0.01% contribution to

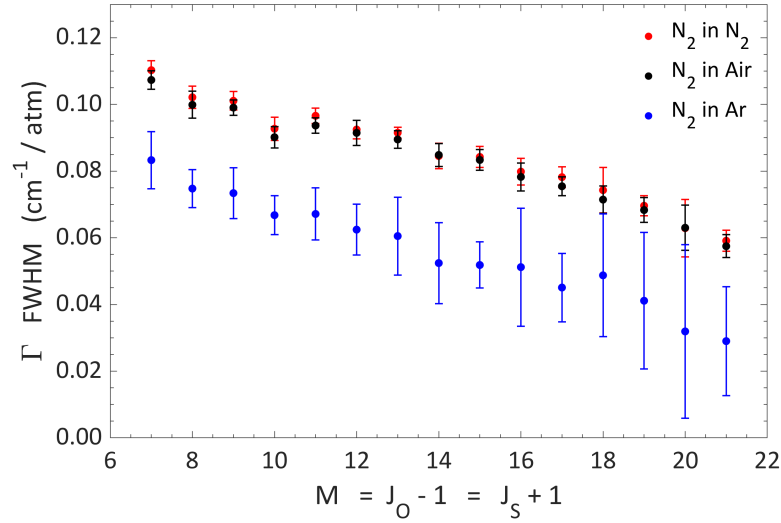
the CARS signal.

The N₂-Ar broadening coefficients were computed from the mixture broadening coefficients using our self-broadening data and inverting the standard mixture rule,

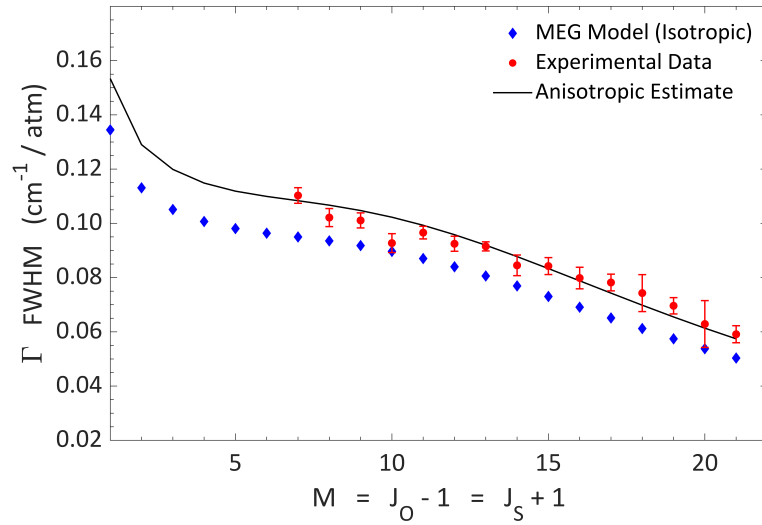
$$\Gamma_{\text{N}_2\text{-mix}}(M) = \chi_{\text{Ar}}\Gamma_{\text{N}_2\text{-Ar}}(M) + \chi_{\text{N}_2}\Gamma_{\text{N}_2\text{-N}_2}(M), \quad (4.4)$$

where χ_j is the mole fraction of species j . The uncertainty in $\Gamma_{\text{N}_2\text{-Ar}}$ was estimated from the uncertainties of $\Gamma_{\text{N}_2\text{-mix}}$ and $\Gamma_{\text{N}_2\text{-N}_2}$ assuming that the errors in the two measurements were uncorrelated and the uncertainty in mixture composition was negligible relative to those uncertainties. The MEG model line broadening coefficients in Figure 4.9a were calculated at 300 K using the m -MEG parameters found in [68]. The error bars in Figure 4.9 represent the 95 % confidence interval, calculated from the two-tailed Student's t -distribution, for the estimate of the slope of the linear regression for each M value [91]. This error estimate is largest for the 20 % nitrogen + 80 % argon case. This is expected because of the lower SNR and poorer quality fits of these recorded spectra as reflected in Figure 4.6.

The black line in Figure 4.9a represents the estimated anisotropic line broadening coefficient at every M value. These estimates were computed by calculating the mean ratio between the MEG model line broadening coefficients determined from these experiments. Figure 4.9a shows that the line broadening coefficients for the anisotropic component of spontaneous Raman scattering from nitrogen is larger than the isotropic MEG model broadening coefficients by 14 ± 5 % in pure nitrogen. Air broadening coefficients are very similar to the self-broadening coefficients but were found to be about 2.5 % smaller on average with a standard deviation of 1.1 % with no detectable systematic variation in M for this ratio. The N₂-Ar broadening coefficients are 25 % lower than the corresponding self-broadening coefficients at $M = 7$, and drop



(a)



(b)

Figure 4.9: (a) Comparison between experimental nitrogen self-broadening line broadening coefficients from anisotropic linewidth fits and theoretical MEG model calculations and (b) a comparison of experimental anisotropic line broadening coefficients for nitrogen in nitrogen, nitrogen in air, and nitrogen in argon. The black line in (a) represents the estimated nitrogen self-broadening anisotropic line broadening coefficients at every M value, which is the mean ratio between the experimental line broadening coefficients and the MEG model coefficients, applied to every M value.

to about 50 % at $M = 21$. The relative magnitude of Ar vs N_2 (self)-broadening coefficients for these anisotropic Raman lines is similar to the relative broadening efficiency of Ar and N_2 for CO infrared P and R branch transitions where the ratio is 0.78 at $M = 7$ and decays more slowly to 0.74 at $M = 21$ [92, 93]. Similarly, the relative efficiency of Ar and N_2 for broadening transitions in the ν_1 fundamental band of HCN at $3\ \mu\text{m}$ is approximately 0.54 ± 0.02 in the range $M = 7 - 18$ [93].

Table 4.1: Experimental nitrogen anisotropic line broadening coefficients, FWHM ($\text{cm}^{-1}/\text{atm}$)

M	N_2 self-broadening	N_2 in air	N_2 in argon
7	0.110 ± 0.003	0.107 ± 0.003	0.083 ± 0.009
8	0.102 ± 0.003	0.100 ± 0.004	0.075 ± 0.006
9	0.101 ± 0.003	0.099 ± 0.002	0.073 ± 0.008
10	0.093 ± 0.003	0.090 ± 0.003	0.067 ± 0.006
11	0.097 ± 0.002	0.094 ± 0.002	0.067 ± 0.008
12	0.092 ± 0.003	0.091 ± 0.004	0.062 ± 0.008
13	0.092 ± 0.002	0.089 ± 0.003	0.061 ± 0.012
14	0.085 ± 0.004	0.085 ± 0.003	0.052 ± 0.012
15	0.084 ± 0.003	0.083 ± 0.003	0.052 ± 0.007
16	0.080 ± 0.004	0.078 ± 0.004	0.051 ± 0.018
17	0.078 ± 0.003	0.075 ± 0.003	0.045 ± 0.010
18	0.074 ± 0.007	0.071 ± 0.004	0.049 ± 0.018
19	0.070 ± 0.003	0.068 ± 0.004	0.041 ± 0.021
20	0.063 ± 0.009	0.063 ± 0.007	0.032 ± 0.026
21	0.059 ± 0.003	0.057 ± 0.003	0.029 ± 0.016

The broadening of the anisotropic lines may also be inferred from purely ro-

tational CARS measurements. Miller et al. [77] and Kliewer et al. [94] have inferred linewidths using the CARS signal decay rate in hybrid fs/ps RCARS. The linewidths reported in [77] vary somewhat irregularly with pressure, and an attempt to fit their inferred linewidths to a linear pressure dependence gave what appeared to be an unreasonably high estimate of the error in the broadening coefficient Γ . Hence we compute an inferred self-broadening coefficient by simply dividing their measured linewidths at 20 atm by the corresponding pressures, and comparing these results with our measurements in Figure 4.10. The uncertainties for the Miller et al. data shown in Figure 4.10 correspond to the uncertainties in linewidth that they report. On Figure 4.10 we also plot the broadening coefficients reported by Kliewer et al. [94]. The error bars shown on Figure 4.10 correspond to the 5% uncertainty they quote. While the uncertainty in the measurements in [77] are large, it is clear that the linewidths reported in [94] are significantly lower than our measured linewidths and appear to agree better with the MEG model calculations of the isotropic Q branch linewidths. While the anisotropic ro-vibrational O and S branch lines we measure also have a vibrational dephasing contribution that is not present in the pure rotational CARS spectra, one would not expect this contribution to be significant. We are presently unable to explain the discrepancy.

In conclusion, this chapter has presented high-resolution room temperature measurements of the anisotropic component of spontaneous Raman scattering from nitrogen for pressures up to 70.1 atm of 100% nitrogen, 100% dry air, and 20% + 80% argon. The recorded O and S branch lines were fit for Lorentzian widths, which were used for linear regressions to determine line broadening coefficients. For all three gas mixtures, the zero pressure limit of the linear regressions were found to be in good agreement with the Lorentzian width determined from a neon lamp, which

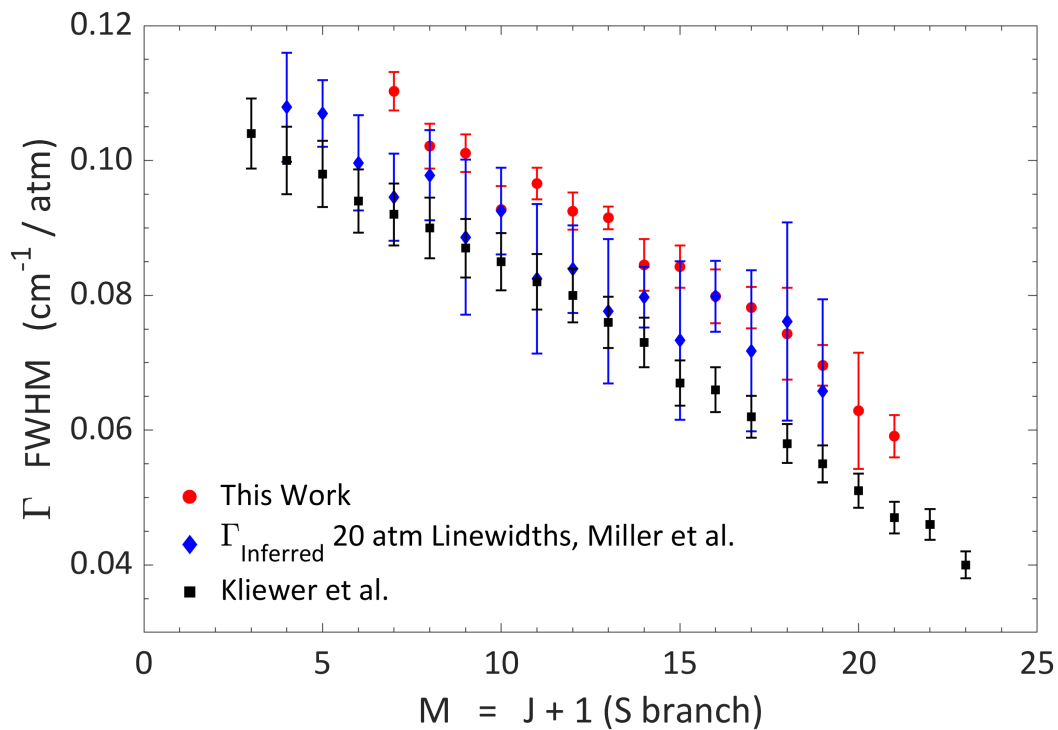


Figure 4.10: Comparison of anisotropic ro-vibrational self-broadening coefficients for N_2 measured in this work with S branch linewidths inferred from time domain measurements using hybrid fs/ps of purely rotational transition using RCARS from Miller et al. and Kliewer et al. [77, 94].

is consistent with our understanding of the effective lineshape. The anisotropic line broadening coefficients were found to be larger than the MEG model line broadening coefficients for pure nitrogen and air respectively, but smaller for nitrogen broadened by argon. The unmixed line model matched the experimental anisotropic spectra for all pressures, indicating that line mixing effects are not significant in the O and S branches of spontaneous Raman scattering at pressures up to 70 atm at room temperature.

Chapter 5

High Pressure Modeling of the Q Branch

This chapter examines line mixing in the Q branch, focusing in particular on the anisotropic tensor component of the spontaneous Raman Q branch. The experimental results presented in Chapter 4 focused on the O and S branches, which are purely anisotropic. These experiments did show evidence of line mixing effects in the Q branch, which exhibited no detectable broadening with increasing pressure and instead narrowed slightly at the highest experimental pressures, as seen in Figure 4.4a. However, because the Q branch is dominated by isotropic scattering, these experiments did not clearly establish whether there is line mixing in the anisotropic component of the Q branch at pressures relevant to gas turbine engines. This is an important question when considering the achievable accuracy of spontaneous Raman thermometry in high pressure gases. The line mixing effect is a transfer of integrated intensity between spectral features; the spectrum can no longer be considered as the sum of individual contributions from lines with distinct vibration-rotation transitions [73]. Because thermometry is accomplished by relating relative intensities to relative state populations through a Boltzmann factor, Raman scattering models must

Portions of this chapter previously appeared in the following publication:

Haller, T. W. and Varghese, P. L., “Measurements of pressure broadening of N₂ in the anisotropic tensor component of spontaneous Raman spectra,” *Combustion and Flame*, vol. 224, pp. 166–176, 2021. DOI: [10.1016/j.combustflame.2020.11.045](https://doi.org/10.1016/j.combustflame.2020.11.045).

The dissertator contributed to this publication through design and conduct of the research, data analysis and interpretation, and writing of the manuscript.

include line mixing effects to achieve accurate temperature measurements when these mixing effects are significant. While these mixing effects are clearly significant in the isotropic component of the Q branch [61, 56, 68, 59], the significance of these line mixing effects in the anisotropic component is less understood. Assuming the anisotropic Q branch mixes like the isotropic Q branch may be a modeling error that results in erroneous temperature measurements when implementing spontaneous Raman thermometry in high pressure gases. This chapter investigates the influence of line mixing in the anisotropic Q branch and the impact of this assumption on the accuracy of spontaneous Raman thermometry. Most of the results and discussion in this chapter previously appeared in [90].

5.1 Line Mixing in the Q Branch

The results presented in Chapter 4 demonstrate that line mixing effects can be neglected in the modeling of the O and S branches up to pressures of 70.1 atm at room temperature. The O and S branches consist entirely of anisotropic scattering, but the Q branch has both an isotropic and anisotropic component. It is well established that line mixing effects must be included in the modeling of the isotropic component of the Q branch at pressures well below 70 atm [61, 65, 56, 57, 68, 59]. However, it is much less clear as to whether line mixing effects should also be included in the modeling of the anisotropic component of the Q branch. The theory indicates that the relaxation cross-sections that describe the transfer of integrated intensity between spectral lines are different for isotropic Raman scattering and anisotropic Raman scattering [72, 73, 74]. Because of the contributions of rotational reorientation and rotational dephasing collisions [73], mixing of the anisotropic lines couples transitions in all three branches (O, Q, and S). Therefore, theoretically we would not expect the line mixing effects

in the anisotropic Q branch to be identical to the mixing in the isotropic Q branch. While we do expect the unmixed line approximation to break down in the Q branch at lower density than the O and S branches because the Q branch lines are much more closely spaced, it is not clear that it can be assumed that the anisotropic Q branch lines mix like the isotropic Q branch lines.

5.1.1 Isotropic Simulations

Because the unmixed anisotropic Q branch line positions are identical to the unmixed isotropic Q branch line positions [1], the isotropic component must be simulated to study the anisotropic Q branch component (unless the isotropic component can be removed from the spectrum experimentally). As discussed in Chapter 4, no broadening of the Q branch was detected in the high pressure experimental spectra. This is definitive evidence of line mixing effects, specifically pressure narrowing, which can be demonstrated by comparing simulated spectra with and without the inclusion of line mixing. Because the Q branch is dominated by the isotropic contribution, these simulations will only display the isotropic component of spontaneous Raman scattering.

Figure 5.1a shows simulated isotropic spectra without line mixing effects, only pressure broadening, and Figure 5.1b shows these spectra with the vertical scale expanded by a factor of 100. These simulated spectra were generated using the MEG model line broadening coefficients shown in Figure 4.9a. The temperature for these simulations was 300 K. An instrument lineshape function consisting of a convolution of a trapezoid function and a Lorentzian function was applied to these simulated spectra, with the lineshape parameters set to match the values corresponding to the high pressure experiments described in Chapter 4. Figure 5.1 shows that without line

mixing, as the pressure increases, the isotropic Q branch broadens significantly, which is clearly not what we observe in the experimental spectra shown in Figure 4.4a. Note that all of the simulated spectra shown in Figure 5.1 are normalized so that the area under each spectrum is unity. Therefore, the peak heights decrease with increasing pressure due to the pressure broadening. The simulated isotropic spectra shown in Figure 5.1 do not at all resemble the observed experimental spectra. The complete lack of this broadening behavior in the Q branch of the high pressure experimental spectra indicates that the simulations of the isotropic component which do not line mixing are inadequate over this range of pressures at room temperature.

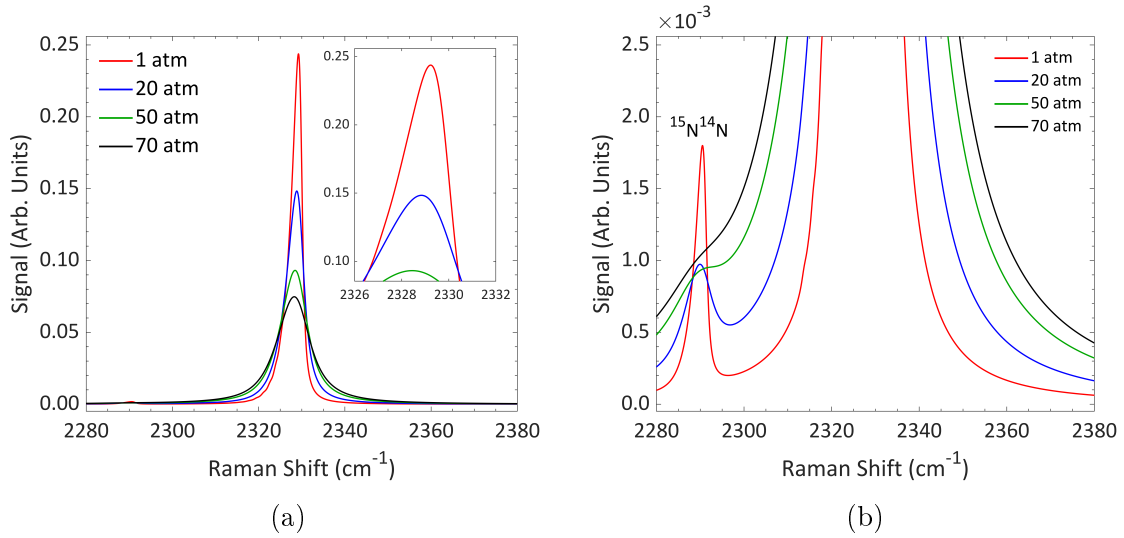


Figure 5.1: Simulations of the isotropic component of spontaneous Raman scattering from nitrogen at 300 K without line mixing.

Line mixing effects can be included in these simulations of the isotropic component through a matrix whose elements reflect the collisional coupling of the rovibrational states [73, 65, 61]. The MEG model was used for the calculation of these matrix elements using the *m*-MEG parameters found in [68]. Figure 5.2a shows simu-

lated isotropic spectra with line mixing included, and Figure 5.2b shows these spectra with the vertical scale expanded by a factor of 100. The temperature for these simulations was again 300 K. The same instrument lineshape function was applied to these spectra. These simulated isotropic spectra with line mixing shown in Figure 5.2 were generated over an extended pressure range to further illustrate the influence of line mixing effects at high pressures.

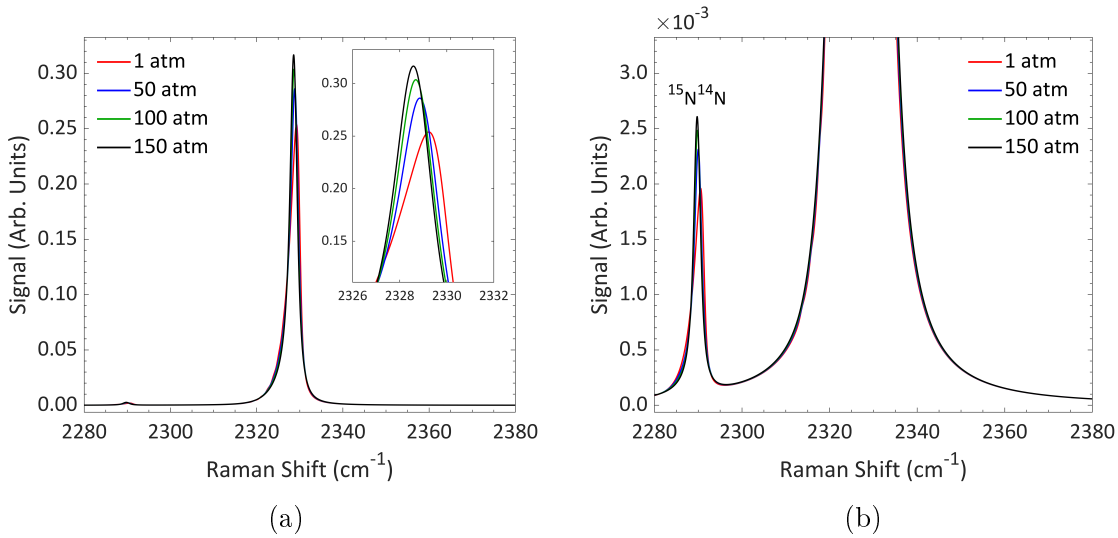


Figure 5.2: Simulations of the isotropic component of spontaneous Raman scattering from nitrogen at 300 K with line mixing.

Figure 5.2 shows that with line mixing included in the simulation, the isotropic Q branch does not broaden with increasing pressure. Instead, the isotropic Q branch narrows slightly. Note that all of the simulated spectra shown in Figure 5.2 are normalized so that the area under each spectrum is unity. Therefore, the peak heights of the simulated spectra increase with increasing pressure due to the pressure narrowing associated with line mixing. Line shifting can also be observed in Figure 5.2a, as the peaks of the simulated isotropic spectra shift to slightly lower Raman shifts with

increasing pressure. The Q branch of the high pressure experimental spectra shown in Figure 4.4a more closely resemble the simulated spectra shown in Figure 5.2 as compared to the simulated spectra that do not include line mixing effects shown in Figure 5.1. Therefore, the high pressure experimental spectra do clearly show evidence of line mixing effects in the Q branch even though the spectral resolution of the high pressure experiments was not sufficient to fully resolve the narrowing and shifting of the Q branch.

While the changes to the simulated isotropic spectra with increasing pressure in Figure 5.2 may appear subtle, the influence of line mixing on the isotropic spontaneous Raman spectrum is profound. This is illustrated in Figure 5.3a, which compares simulated isotropic spectra with and without line mixing at 300 K and 70 atm. Figure 5.3b shows these spectra with the vertical scale expanded by a factor of 100. Both spectra shown in Figure 5.3 are normalized so that the area under each spectrum is unity. The significant differences between these simulated spectra demonstrate why it is important to determine whether line mixing effects should be included in modeling of the anisotropic component of the Q branch of spontaneous Raman scattering.

5.1.2 Anisotropic Q branch

We cannot directly assess the significance of line mixing effects in the anisotropic component of the Q branch from experimental data because the strong isotropic contribution to the Q branch overlaps the anisotropic contribution. An indirect assessment can be made by subtracting a model anisotropic contribution that neglects line mixing effects from experimental data and comparing the difference to a simulated isotropic contribution with line mixing effects. If the two agree then we can infer that the anisotropic component was modeled satisfactorily. This is illustrated in Fig-

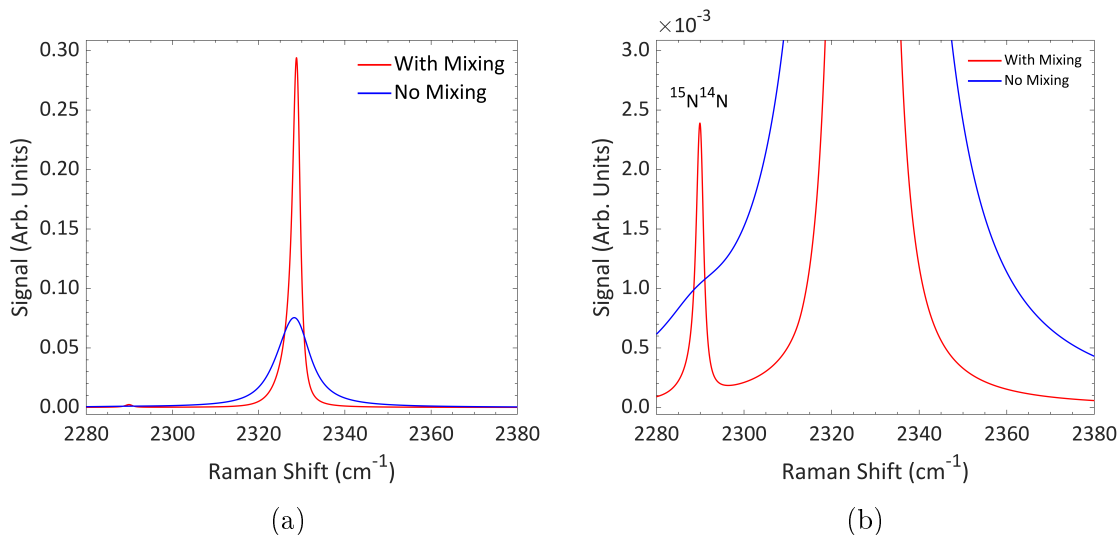


Figure 5.3: Simulations of the isotropic component of spontaneous Raman scattering from nitrogen at 300 K and 70 atm with and without line mixing.

ures 5.4 a-d which shows data at 37.1 atm (Figure 5.4 a,b) and 70.1 atm (Figure 5.4 c,d). A complete anisotropic simulation requires line broadening coefficients for all M . The estimated nitrogen self-broadening anisotropic line broadening coefficients shown in Figure 4.9a were used to calculate anisotropic linewidths for $M \leq 6$. The anisotropic contribution to the Q branch lines were broadened with the J-dependent anisotropic linewidths shown in Figure 5.4a and using $M = J$ for the Q branch according to Equation 4.2. Combining these estimated anisotropic linewidths with the fitted anisotropic linewidths allows us to simulate the entire anisotropic spectrum in the unmixed line approximation shown as blue lines in Figures 5.4 a-d. This simulated anisotropic spectrum was subtracted from the experimental data to estimate the residual purely isotropic spectrum. These are shown as the solid symbols in Figures 5.4 a-d. The red lines in these figures are the mixed isotropic simulation at the corresponding pressures (37.1 atm and 70.1 atm respectively). The isotropic simula-

tion included line mixing effects and was generated using the MEG model [61, 65] with the m -MEG parameters found in [68].

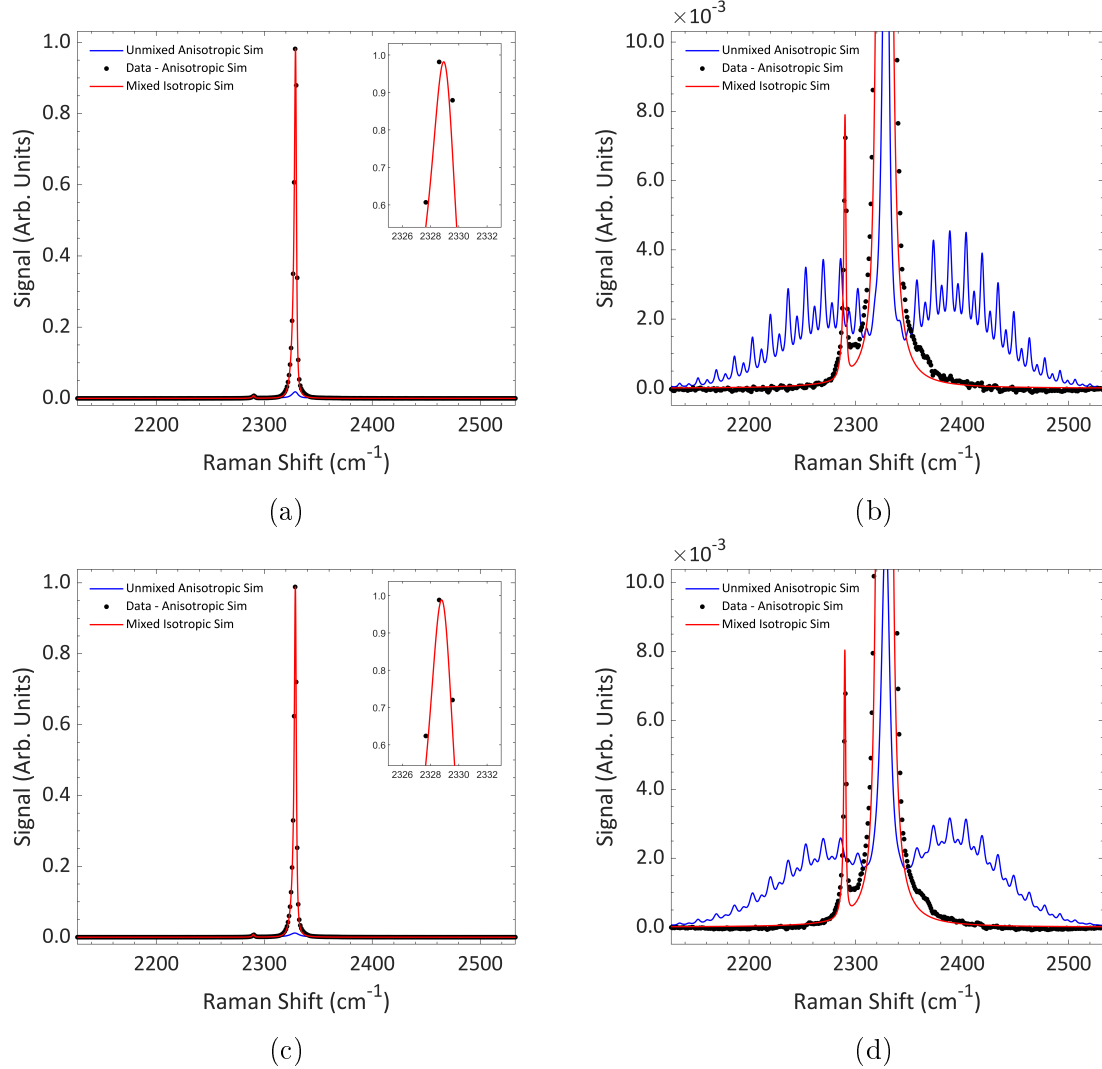


Figure 5.4: Comparison between experimental isotropic spectra and a mixed isotropic simulation generated using the MEG model at (a,b) 37.1 atm and (c,d) 70.1 atmosphere. The vertical scale is expanded by 100 in (b,d).

Figures 5.4a and 5.4c show good overall agreement between the inferred isotropic spectrum and the simulation. Figures 5.4b and 5.4d, show the same data with the

vertical scale expanded by a factor of 100. Although both Figures 5.4b and 5.4d show small systematic differences between experimental data with the anisotropic contribution subtracted and the computed isotropic contribution near the base of the Q branch feature, the differences are less than 0.1% and do not increase with pressure as they would if they were a manifestation of line mixing. From this we conclude that line mixing effects seem to be nearly negligible even in the Q branch of the anisotropic spectrum up to pressures of 70 atm at room temperature.

5.2 Effect on High Pressure Thermometry

Most simulations of line mixing effects at high pressures or densities assume that the anisotropic Q branch lines mix like the isotropic lines at high pressure. As shown in Section 5.1, there is evidence that this assumption is invalid. The significance of this assumption must be evaluated in the context of spontaneous Raman thermometry in high pressure gases. Given that the strength of the anisotropic Q branch lines are only about 1% the strength of the isotropic Q branch lines, any systematic error in spontaneous Raman thermometry temperature measurements resulting from this assumption may be negligible compared to the overall uncertainty in a particular application. However, if this systematic error is not negligible, then simulations of high pressure spontaneous Raman spectra should not include the anisotropic Q branch lines in line mixing calculations and instead treat them like the O and S branch lines. Therefore, it is necessary to investigate the influence of this modeling error on temperatures inferred from fitting experimental Raman spectra to a model that is slightly inaccurate.

The ideal approach to quantitatively investigate the significance of this mod-

eling error is to use the different models to compare inferred temperatures from experimental spontaneous Raman spectra recorded in high temperature, high pressure gases. Due to limitations of the experimental setup described in Chapter 4, we do not have high temperature high pressure experimental spontaneous Raman spectra available. The 5 atm flame temperature spectra discussed in Chapter 3 were recorded in gases at sub-atmospheric density and hence are not likely to test line mixing effects. However, we can generate a simulated spontaneous Raman spectrum at high temperature and high pressure, and then infer a temperature from this simulated spectrum using a slightly inaccurate model that assumes the Q branch anisotropic lines mix like the isotropic lines. This approach will give a quantitative estimate of this modeling error.

A spontaneous Raman spectrum was simulated at 1800 K and 70 atm. For this simulated spectrum, the data points were generated at an average spectral density of $0.94 \text{ cm}^{-1}/\text{pixel}$, which matches the experimental spectra in Chapter 4. An instrument lineshape function consisting of a convolution of a trapezoid function and a Lorentzian function was applied to this simulated spectrum. The values of the parameters used for this instrument lineshape function were set to match the values for the experimental spectra. Line mixing effects were included only in the isotropic part; the anisotropic component was broadened but not mixed for all three branches (O, Q, and S). The collisional broadening coefficients at high temperature were computed using the temperature scaling given by the MEG model linewidths [67, 68]. The same temperature scaling was applied to the anisotropic linewidths in Figure 4.9 So this simulated Raman spectrum was generated to represent what we expect from a high temperature, high pressure experimental Raman spectrum. This simulated spectrum is shown as the black circles in Figure 5.5a. The spectrum is shown on an expanded

vertical scale in Figure 5.5b. In Figures 5.5c and 5.5d, a small amount of shot noise and random readout noise has been added to the simulated spectrum to make it more representative of an experimental spectrum.

Hot band contributions (Raman scattering from $v = 1, 2, \dots$) are significant at flame temperatures and can be seen in Figure 5.5. For these calculations, we assume that the linewidths of the hot band transitions are the same as the corresponding transitions from the ground state. The relative intensity of the Q branches can be used for thermometry even if the weak O and S branches are obscured by noise, as shown in Figures 5.5c and 5.5d.

Temperatures were inferred from the simulated spectrum using a model that assumes that the O and S branch transitions (purely anisotropic) are broadened and have no line mixing, but both the isotropic and anisotropic contributions to the Q branch transitions are broadened and mixed identically. A library of model spectra was generated as a function of temperature. Computing the sum of the squares of the residual error, a temperature was inferred from the simulated spectrum by determining which model spectrum gives the smallest residual. The sum of the squares was computed over the spectral interval from 2150 cm to 2400 cm⁻¹ (indicated by the dashed vertical lines on Figure 5.5). These results are insensitive to the precise spectral interval chosen provided it contains the region containing the Q branch of the fundamental and the hot bands.

The sum of the squared residual error is plotted versus model temperature in Figure 5.6a for the noise-free simulated spectrum and in Figure 5.6b for the simulated spectrum with added noise. The "best fit" spectrum using the slightly incorrect model was found to infer a temperature of 1810 K, which is an error of about 0.6%. This

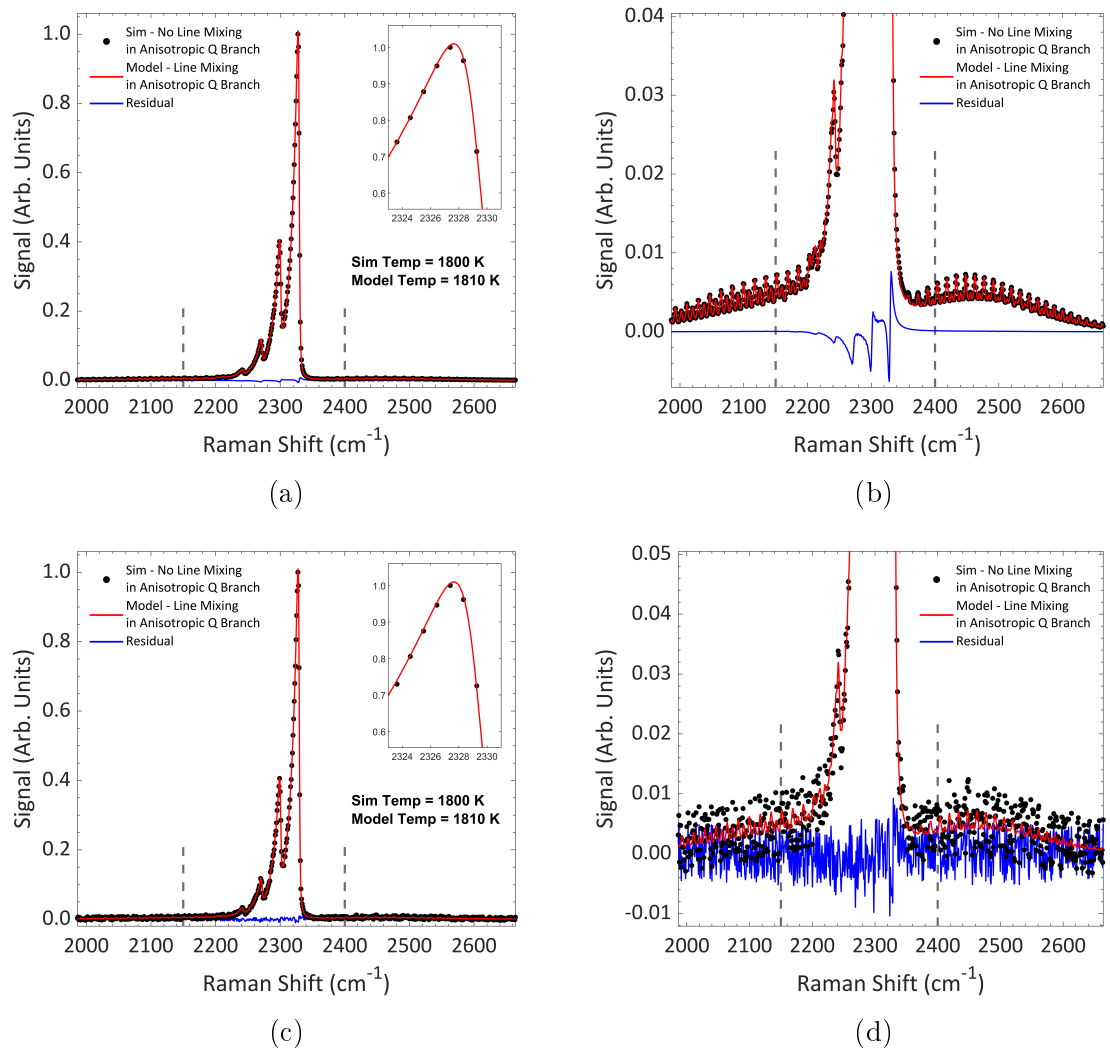


Figure 5.5: Simulated high temperature and pressure (1800 K, 70 atm) Raman spectrum of nitrogen with anisotropic contribution unmixed and the isotropic Q branch mixed. In (c,d) a small amount of shot noise and random readout noise has been added to the simulated experimental spectrum. The simulated spectrum is compared to a model spectrum which assumes that the anisotropic Q branch lines are mixed exactly like the isotropic lines. The dashed vertical lines indicate the frequency range over which the sum of the squared residual is used to infer the best match between simulated data and a model spectrum.

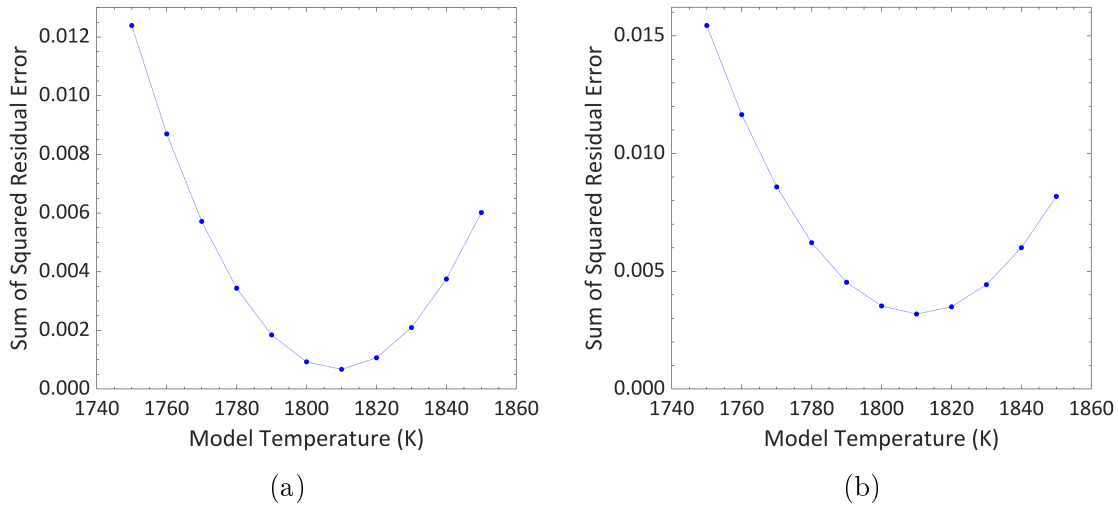


Figure 5.6: Variation of the sum of the squared residual error with temperature when using a library of model spectra that assume the anisotropic Q branch lines broaden and mix like the isotropic Q branch lines. (a) Without noise added to the simulated spectrum, corresponding to Figures 5.5a and 5.5b. (b) With noise added to the simulated spectrum, corresponding to Figures 5.5c and 5.5d.

was the inferred temperature for both the noise-free spectrum and the spectrum with added noise. Figure 5.6 shows that the minimum of the sum of the squared residual error occurred for the 1810 K model temperature in both cases. If this same procedure is repeated at a pressure of 300 atm at 1800 K, the resulting best fit model temperature is 1820 K, which is an error of about 1.1%. Again, the addition of noise to the simulated spectrum did not change this result.

While this inferred systematic error due to model error is probably negligible in most applications, a couple of caveats should be noted. First, these calculations were done using nitrogen broadening data. For measurements in flames or post-combustion gases where there is significant broadening by water vapor and carbon dioxide, the effects of the model error may be a little more significant. For example, the line broadening coefficients of N_2 by water vapor are larger than the self-broadening co-

efficients and do not drop significantly with increasing rotational quantum number [95] (compare with Figure 4.9). However, the broadening coefficients do not differ by orders of magnitude so the above calculations indicate that model error could introduce a systematic bias of at most a few percent in temperature measurements in flames. Second, if another species is used for flame thermometry that has a stronger anisotropic contributions to the spontaneous Raman spectrum than nitrogen, then the error will also be increased.

The bias can be removed by using spectral models that broaden and mix the anisotropic Q branch lines independently of the isotropic component. The high pressure experiments show that line mixing does not occur in the O and S branches at pressures as high as 70 atm at room temperature. Additionally, there is evidence that line mixing is also not significant in the anisotropic Q branch over this range of pressure. So the anisotropic spectrum can be modeled to reasonable precision as the sum of independently broadened overlapping spectral lines. Since density, not pressure is the key parameter driving line mixing, at flame temperatures line mixing of the anisotropic component of the nitrogen spontaneous Raman spectrum is only likely to be significant at pressures above 400 atm. We conclude that line mixing effects do not have to be included in the modeling of the anisotropic component for accurate spontaneous Raman thermometry in gas turbine engines.

5.2.1 Consequences for Elevated Pressure Thermometry

The results of the high pressure spontaneous Raman scattering experiments merit reexamination of the elevated pressure experiments discussed in Chapter 3. The model used to fit these elevated pressure spectra for temperature applied the same lineshape function to every spectral line in the simulated spectrum. Every isotropic

and anisotropic line was assumed to have the same Lorentzian halfwidth. This model neglects two density driven effects: the dependence of molecular linewidths on rotational quantum number and line mixing. The high pressure experimental results demonstrate that these effects can have a significant impact on the spontaneous Raman spectrum. Therefore, the consequences of using this simplified model for thermometry need to be considered.

Applying the same lineshape function to the entire spectrum will affect the accuracy of the temperature measurement only if the experimental spectral resolution is sufficient to detect the dependence of molecular linewidths on rotational quantum number and line mixing at the experimental conditions. The elevated pressure experiments presented in Chapter 3 were recorded with a spectrograph equipped with a 100 μm slit, whereas the high pressure experiments were recorded with a 25 μm slit. Because of this, the contribution of the instrument to the lineshape function was significantly larger for the elevated pressure experiments, which reduces the spectral resolution.

The elevated pressure experiments presented in Chapter 3 did not have sufficient spectral resolution to detect the dependence of molecular linewidths on rotational quantum number or line mixing effects. Consider the experimental spectrum recorded in a partially premixed flame at 5 atm, which is shown in Figure 3.9, along with the fit and corresponding residual error. The inferred temperature was 2008 K. The model used for this fit applied the same lineshape function across the entire spectrum and did not include line mixing. However, this model appears to represent the experimental spectrum quite well; the maximum residual error is 1% of the peak value. In the O and S branches, the residual error is small and relatively uniform;

the residual does not vary with rotational quantum number. This indicates that neglecting the dependence of molecular linewidths on rotational quantum number did not affect this temperature fit. The quality of the fit in the Q branch also looks to be quite good, but line mixing of the isotropic Q branch lines could potentially cause a significant error in the temperature measurement.

To investigate the sensitivity of the elevated pressure experiments to line mixing, we can compare two simulations of the isotropic Q branch at the experimental pressure and temperature, with and without line mixing. By convolving these simulated spectra with an instrument lineshape function that is identical to the instrument function of the elevated pressure experiments, the difference between these simulated spectra will illustrate the sensitivity of these experiments to line mixing. Anisotropic lines do not need to be included in these simulations because as discussed above, line mixing effects should not to be included in the modeling of the anisotropic component of the spontaneous Raman spectrum.

Figure 5.7 shows a comparison of two simulations of the isotropic Q branch, with and without line mixing, at 2008 K and 5 atm. Both of these simulated spectra have been convolved with the instrument lineshape function of the elevated pressure experiments. The spectrum without line mixing was modeled with the same molecular Lorentzian width as the fit to the experimental spectrum recorded in a flame at 5 atm, applied to every isotropic Q branch line. So, the simulated spectrum without line mixing in Figure 5.7 represents the isotropic component of the fit shown in Figure 3.9. The MEG model was used to simulate the spectrum with line mixing in Figure 5.7. Because the 5 atm experimental spectrum was recorded close to the flame front, perturbing species such as CO_2 and H_2O were present in the measure-

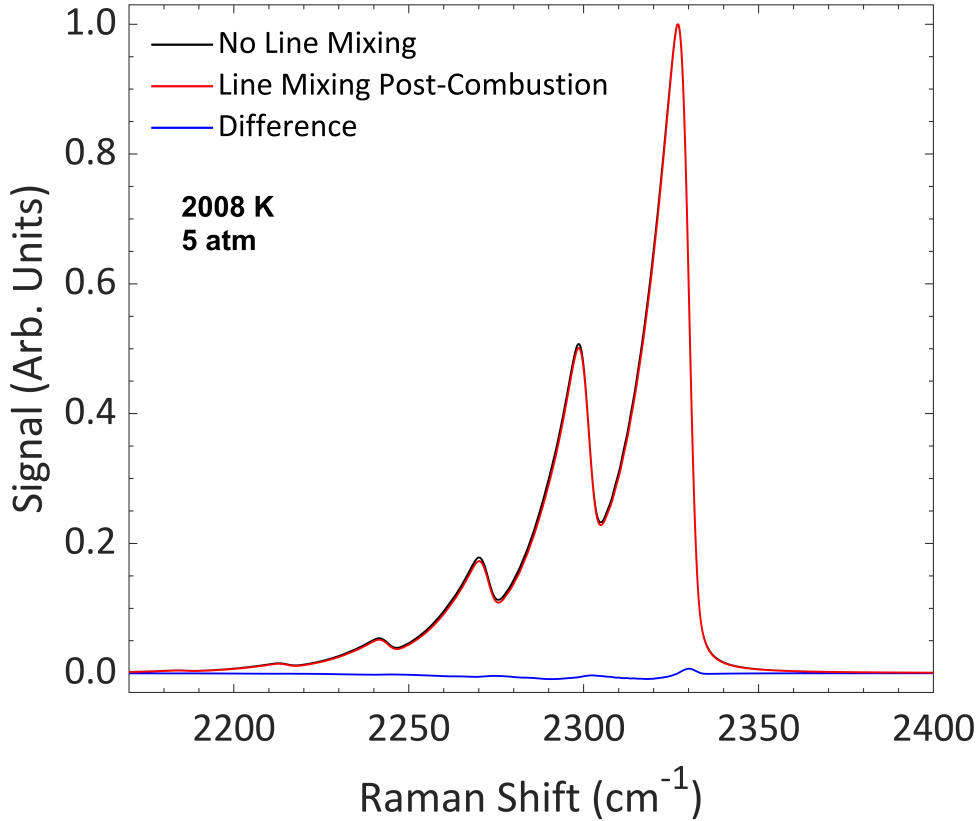


Figure 5.7: Simulations of the isotropic component of the nitrogen spontaneous Raman spectrum at 5 atm and 2008 K, with and without line mixing. The instrument lineshape function from the experimental Raman spectrum recorded in a 5 atm flame has been applied to these simulations. Because of this relatively broad instrument function, differences between these simulations are nearly undetectable.

ment volume. To account for the presence these species, three sets of MEG model parameters were used in the line mixing calculations, one each for $\text{N}_2\text{-N}_2$, $\text{N}_2\text{-CO}_2$, and $\text{N}_2\text{-H}_2\text{O}$. The *m*-MEG parameters found in [68] were used for $\text{N}_2\text{-N}_2$, and the parameters for $\text{N}_2\text{-CO}_2$ and $\text{N}_2\text{-H}_2\text{O}$ were taken from [96]. These MEG model calculations were combined based on the equilibrium mole fractions of N_2 , CO_2 , and H_2O (0.708, 0.085, and 0.207 respectively). These mole fractions were calculated for

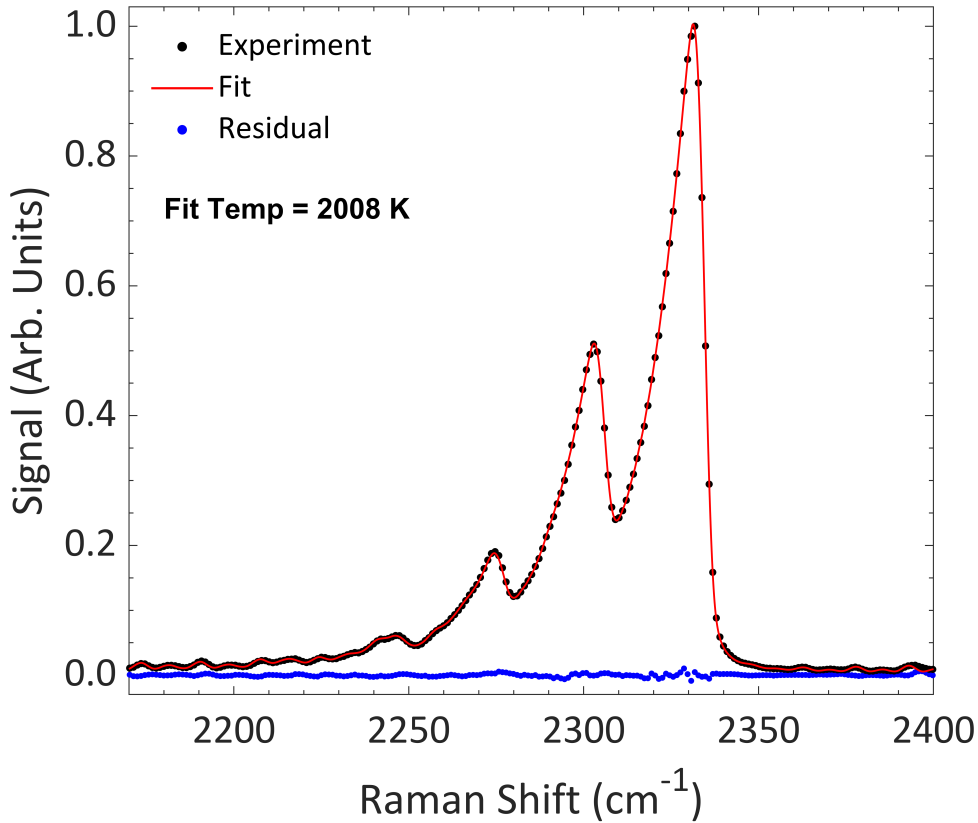


Figure 5.8: Temperature fit to nitrogen Raman spectrum recorded in a partially premixed flame at 5 atm, resulting in an inferred temperature of 2008 K. The model used for this fit did not include line mixing and applied the same lineshape function to every spectral line.

a flame with a stoichiometric fuel-air mixture and a fuel consisting of 70 % CH₄ and 30 % H₂ by volume, which was the fuel mixture for the partially premixed flame in these elevated pressure experiments. Therefore, the simulated spectrum with line mixing in Figure 5.7 represents the isotropic component of the nitrogen spontaneous Raman spectrum in a 5 atm flame, convolved with the instrument lineshape function of the elevated pressure experiments. Recall the excellent fit of the model to the data shown in Figure 3.9 and repeated in Figure 5.8 for convenient comparison.

The two simulations with and without line mixing shown in Figure 5.7 are virtually indistinguishable, and the differences between these simulated spectra are very small. The maximum difference is 0.9% of the peak value. These spectra are noise free simulations, and with just a tiny amount of shot and read-out noise these spectra would become indistinguishable. I conclude that experiments with this instrument resolution were not sensitive to line mixing effects, and excluding line mixing calculations from the spectral model did not reduce the accuracy of the temperature measurement for these experiments.

Chapter 6

Conclusions

The work presented in this dissertation has investigated spontaneous Raman thermometry in high pressure gases. The motivation for this work was the application to gas turbine engines, which are susceptible to turbine blade failure if hot-spots are present in the post-combustion flow. Accurate temperature measurements of the pre-turbine temperature profile are crucial to the design process. Spontaneous Raman thermometry can provide nonintrusive, remote measurements of temperature with high spatial resolution. However, the high pressure environment found in gas turbine engines complicates this spectroscopic technique. As gas density increases, the collision frequency increases, which increases the pressure broadening and causes strongly overlapped spectral lines to mix. The overall objective of this work was to examine the influence of these collision-induced effects on the ro-vibrational spontaneous Raman spectrum and determine the impact on the accuracy of this temperature measurement technique, with the goal of extending spontaneous Raman thermometry to high pressure environments.

Spontaneous Raman spectra were first recorded in an elevated pressure combustion chamber. This work demonstrated the ability to measure a steep temperature gradient in a closed, combustion chamber at pressures up to 5 atm using ro-vibrational spontaneous Raman scattering. For the relatively broad entrance slit on the spectrometer (and corresponding lower spectral resolution), subtle evidence of pressure

broadening was detectable at 5 atm and room temperature, but at flame temperature, no pressure broadening was detected. The elevated pressure environment did not adversely affect our ability to simulate and fit the spontaneous Raman spectrum from nitrogen. The uncertainty for spontaneous Raman thermometry at atmospheric pressure was estimated to be ± 15 K by performing temperature measurements on a reference burner.

To significantly increase the maximum pressure in which we could record spontaneous Raman spectra, a high pressure chamber with good optical access was constructed. This pressure chamber has a maximum operating pressure of about 70 atm, 3 windows, and can be remotely filled with a specified gas mixture, but this chamber was only designed for measurements at room temperature. High-resolution, room temperature spontaneous Raman spectra of nitrogen were recorded in this pressure chamber at pressures up to 70.1 atm for three gas mixtures: 100 % nitrogen, 100 % dry air, and 20 % nitrogen + 80 % argon. The recorded O and S branch lines were fit for Lorentzian widths, which were used for linear regressions to determine line broadening coefficients for the anisotropic tensor component of ro-vibrational spontaneous Raman scattering. For all three gas mixtures, the zero pressure limit of the linear regressions were found to be in good agreement with the instrument Lorentzian width determined from a neon lamp, which is consistent with our understanding of the effective lineshape. The anisotropic line broadening coefficients were found to be larger than the MEG model line broadening coefficients for pure nitrogen and air respectively, but smaller for nitrogen broadened by argon.

The experimental high pressure spectra were also used to investigate line mixing in ro-vibrational spontaneous Raman scattering. The isotropic component of the

spectrum showed definitive evidence of line mixing, so the MEG model was used to simulate the isotropic component with line mixing. The unmixed line model matched the experimental anisotropic spectra for all pressures, indicating that line mixing effects are not significant in the O and S branches of spontaneous Raman scattering at pressures up to 70 atm at room temperature. However, it was less clear if the anisotropic Q branch lines exhibited line mixing because the strong isotropic contribution to the Q branch overlaps the anisotropic contribution. It is expected that the isolated line approximation will break down in the Q branch at lower pressures than for the O and S branches because the lines are much more closely spaced. Therefore, an indirect assessment of line mixing in the anisotropic Q branch was made by subtracting a model anisotropic contribution that neglects line mixing effects from experimental data and comparing the difference to a simulated isotropic contribution with line mixing effects. The results indicate that, within the spectral resolution of these measurements, line mixing effects were not perceptible for the anisotropic Q branch lines for pressures up to 70 atm at room temperature. Assuming that the anisotropic contribution to the Q-branch is mixed like the isotropic part will result in small systematic overestimation of the order of a few percent in the temperature inferred by spontaneous Raman thermometry in high pressure flames, and the error increases with pressure. The bias can be removed by modeling the anisotropic spectrum independently of the isotropic part as the sum of individual spectral lines.

In conclusion, this work has demonstrated that the high pressure environment of gas turbine engines does not prohibit spontaneous Raman thermometry. Rotational quantum number dependent pressure broadening needs to be incorporated into simulations of the anisotropic component of ro-vibrational spontaneous Raman scattering for high pressure gases. Anisotropic line broadening coefficients have been measured

for nitrogen and presented in this dissertation. The lineshape of the isotropic component of spontaneous Raman scattering has been shown to be well represented by the MEG model over the range of pressures studied. Therefore, spontaneous Raman thermometry is in fact capable of providing accurate measurements of temperature in high pressure gases.

6.1 Future Work

Given the conclusions discussed above, it is reasonable to recommend spontaneous Raman thermometry for temperature measurements in a high pressure gas turbine test rig. However, challenges associated with this application may require further studies of spontaneous Raman scattering. The high pressure Raman spectra presented in this dissertation were restricted to room temperature due to the limitations of the high pressure chamber. Experimental spontaneous Raman spectra recorded in high pressure, high temperature gases would be a valuable resource to further study and adapt spontaneous Raman simulations for high pressure gases. Pressure chambers with good optical access that are capable of withstanding high temperatures are challenging to design and expensive to construct. Often two sets of custom windows are needed to meet these criteria, one window for the pressure stress and one actively cooled window for the thermal stress. Unfortunately, a pressure chamber of this design was beyond the time and financial constraints of this work.

The work presented in this dissertation was also limited to spontaneous Raman scattering from nitrogen. Depending on the application, Raman scattering from other molecular species, such as oxygen or carbon dioxide, may be more beneficial. If a species used for thermometry has a stronger anisotropic contribution to the spon-

taneous Raman spectrum than nitrogen, then characterizing the pressure broadening and line mixing of the anisotropic component becomes more important for accurate temperature measurements. Additionally, the presence of other molecular species is likely to impact the line broadening coefficients of nitrogen. For example, water vapor and carbon dioxide could have a significant effect in a combustion experiment. Even with linewidth measurements of nitrogen broadened by carbon dioxide and nitrogen broadened by water vapor, this could pose a challenge if the gas composition is unknown or unsteady. However, this challenge could potentially be overcome with simultaneous measurements of gas composition and temperature, for example by simultaneously recording low-dispersion and high-dispersion Raman spectra.

A recommended avenue for future work that closely relates to the work in this dissertation concerns the inclusion of line mixing in simulations of the anisotropic component of spontaneous Raman scattering. For the isotropic component, the matrix of cross sections for a change in rotational state due to collisions simplifies when vibrational dephasing is neglected. However, for the anisotropic component, the matrix of cross sections for a change in rotational state due to collisions is much more complicated because it is a function of rotational reorientation and rotational dephasing, both of which are expected to be dependent on rotational state. Thus the existing scaling laws, such as the MEG model, that are specific to the isotropic component are not directly applicable to the anisotropic component. Expressions for the functional dependence of rotational reorientation and rotational dephasing on rotational state are not currently available. Quasiclassical trajectory calculations could provide answers for the open questions concerning rotational reorientation and rotational dephasing, which would subsequently enable the development of line mixing models for the anisotropic component of ro-vibrational spontaneous Raman scattering.

Appendices

Appendix A

Calculation of Line Mixed Raman Spectra

This appendix derives the equation necessary to calculate a ro-vibrational spontaneous Raman spectrum with line mixing efficiently, following the general procedure described by Koszykowski et al. [65] for CARS. When the impact approximation holds, the spectral intensity as a function of frequency, $I(\omega)$, can be related to collisions through a general expression [73, 61, 85, 86] as

$$I(\omega) = \text{Im} [c \mathbf{d} \cdot \mathbf{G}(\omega)^{-1} \cdot \mathbf{P} \cdot \mathbf{d}] \quad (\text{A.1})$$

where c is a scalar constant, \mathbf{d} is a vector containing the square root of the polarizability matrix elements for every rotational level that is significantly populated in a given vibrational level, \mathbf{P} is a diagonal matrix of the population distribution, and \mathbf{G} is the G matrix, which is defined as

$$\mathbf{G}(\omega) = -\omega \mathbf{I} + \boldsymbol{\omega}_0 + i\rho \langle \mathbf{v} \cdot \boldsymbol{\sigma} \rangle \quad (\text{A.2})$$

where \mathbf{I} is the identity matrix, $\boldsymbol{\omega}_0$ is a diagonal matrix of transition frequencies, ρ is the gas density, and the term $\rho \langle \mathbf{v} \cdot \boldsymbol{\sigma} \rangle$ is the velocity-averaged cross section matrix. By defining a matrix \mathbf{K} as

$$\mathbf{K} = \mathbf{G}(\omega) + \omega \mathbf{I} , \quad (\text{A.3})$$

then \mathbf{K} can be expressed as

$$\mathbf{K} = \boldsymbol{\omega}_0 + i\rho \langle \mathbf{v} \cdot \boldsymbol{\sigma} \rangle . \quad (\text{A.4})$$

The matrix \mathbf{K} will be constant for all spectral frequencies in a given vibrational level in a single ro-vibrational Raman spectrum. Let λ_n be the n th eigenvalue of matrix \mathbf{K} and $\mathbf{\Lambda}$ be a diagonal matrix with elements λ_n . Take \mathbf{A} to be the matrix of the eigenvectors of \mathbf{K} , which can be used to diagonalize the inverse of matrix \mathbf{K} by the following operation:

$$\mathbf{A}^{-1}\mathbf{K}^{-1}\mathbf{A} = \mathbf{\Lambda}^{-1} . \quad (\text{A.5})$$

Substituting for \mathbf{K} using Equation A.3 and rearranging the terms gives the following result:

$$\mathbf{A}^{-1}(\mathbf{G}(\omega) + \omega\mathbf{I})^{-1}\mathbf{A} = \mathbf{\Lambda}^{-1} \quad (\text{A.6})$$

$$\mathbf{A}^{-1}\mathbf{G}(\omega)^{-1}\mathbf{A} + \mathbf{A}^{-1}\omega^{-1}\mathbf{I}\mathbf{A} = \mathbf{\Lambda}^{-1} \quad (\text{A.7})$$

$$\mathbf{A}^{-1}\mathbf{G}(\omega)^{-1}\mathbf{A} + \omega^{-1} = \mathbf{\Lambda}^{-1} \quad (\text{A.8})$$

$$\mathbf{A}^{-1}\mathbf{G}(\omega)^{-1}\mathbf{A} = -\omega^{-1} + \mathbf{\Lambda}^{-1} \quad (\text{A.9})$$

Equation A.9 can be utilized to calculate a Raman spectrum without performing an inversion of the G matrix for every spectral frequency of interest. First write Equation A.1 as

$$I(\omega) = \text{Im} [c \mathbf{d} \mathbf{A} \mathbf{A}^{-1} \mathbf{G}(\omega)^{-1} \mathbf{A} \mathbf{A}^{-1} \mathbf{P} \mathbf{d}] , \quad (\text{A.10})$$

then apply Equation A.9 to get:

$$I(\omega) = \text{Im} [c \mathbf{d} \mathbf{A} (-\omega + \mathbf{\Lambda})^{-1} \mathbf{A}^{-1} \mathbf{P} \mathbf{d}] . \quad (\text{A.11})$$

Equation A.11 can then be rearranged to match the form in Koszykowski et al. [65]:

$$I(\omega) = \text{Im} \left[c \sum_n \frac{[(\mathbf{d} \mathbf{A}) \cdot (\mathbf{A}^{-1} \mathbf{P} \mathbf{d})]_n}{-\omega + \lambda_n} \right] \quad (\text{A.12})$$

where the index n in the numerator refers to the n th element of the vector resulting from the dot product between vectors (\mathbf{dA}) and $(\mathbf{A}^{-1}\mathbf{Pd})$. For completeness, to generate the ro-vibrational Raman spectrum, Equation A.12 must be summed over all vibrational levels as shown here:

$$I(\omega) = c \sum_v \sum_n \text{Im} \left[\frac{[(\mathbf{dA}) \cdot (\mathbf{A}^{-1}\mathbf{Pd})]_n}{-\omega + \lambda_n} \right]. \quad (\text{A.13})$$

Equation A.13 is the final result. This equation was used to calculate the line mixed ro-vibrational spontaneous Raman spectra presented in this dissertation. Because the matrix \mathbf{K} is a function of the transition frequencies, ω_0 , the matrix \mathbf{K} will be different for every vibrational level. Therefore, the eigenvector matrix, \mathbf{A} , and the eigenvalues, λ_n , must be recalculated for every vibrational level. The diagonal matrix of the population distribution, \mathbf{P} , also changes with vibrational level.

It should be noted that in Equation A.13, λ_n , which represents the n th eigenvalue of matrix \mathbf{K} , is complex. Therefore, it may be preferred to rearrange Equation A.13 so that the imaginary component is the numerator, making it easier to isolate the real and imaginary terms. The following steps are merely algebraic manipulations of Equation A.13 to more easily visualize the real and imaginary components of Equation A.13. The eigenvalue, λ_n , has a real and imaginary component:

$$\lambda_n = \lambda_{n\Re} + i\lambda_{n\Im} \quad (\text{A.14})$$

where $\lambda_{n\Re}$ and $\lambda_{n\Im}$ are the real and imaginary components of λ_n respectively. Substituting, Equation A.13 becomes

$$I(\omega) = c \sum_v \sum_n \text{Im} \left[\frac{[(\mathbf{dA}) \cdot (\mathbf{A}^{-1}\mathbf{Pd})]_n}{-\omega + (\lambda_{n\Re} + i\lambda_{n\Im})} \right] \quad (\text{A.15})$$

which can then be multiplied by the complex conjugate of the denominator, as shown here:

$$I(\omega) = c \sum_v \sum_n \text{Im} \left[\frac{[(\mathbf{d}\mathbf{A}) \cdot (\mathbf{A}^{-1}\mathbf{P}\mathbf{d})]_n [(-\omega + \lambda_{n\Re}) - i\lambda_{n\Im}]}{[(-\omega + \lambda_{n\Re}) + i\lambda_{n\Im}] [(-\omega + \lambda_{n\Re}) - i\lambda_{n\Im}]} \right], \quad (\text{A.16})$$

which simplifies to

$$I(\omega) = c \sum_v \sum_n \text{Im} \left[\frac{[(\mathbf{d}\mathbf{A}) \cdot (\mathbf{A}^{-1}\mathbf{P}\mathbf{d})]_n [(-\omega + \lambda_{n\Re}) - i\lambda_{n\Im}]}{(\omega - \lambda_{n\Re})^2 + \lambda_{n\Im}^2} \right]. \quad (\text{A.17})$$

Equation A.17 is algebraically equivalent to Equation A.13. Note that \mathbf{A} and \mathbf{A}^{-1} are complex so that the imaginary part cannot be obtained by inspection. However, it can be shown that in the low pressure limit one gets the sum of Lorentzian lineshapes centered at $\lambda_{n\Re}$ with halfwidths of $\lambda_{n\Im}$.

Appendix B

Standard Operating Procedure

Plasma & Combustion Diagnostics Laboratory - ASE 5.118

High Pressure Raman Spectroscopy Experiment

5.31.2020

B.1 Purpose

This Standard Operating Procedure (SOP) outlines requirements to be considered by an authorized user of the High Pressure Raman Spectroscopy Experiment and describes the normal operation of the experiment and specific considerations for pandemic response.

B.2 Personnel

Authorized Personnel: The High Pressure Raman Spectroscopy Experiment may be operated only by authorized personnel who are fully cognizant of all safety issues involved in the operation of all required devices. These personnel are to ensure that the laser is only operated in the manner laid out in this document. To become an authorized user, one must:

1. Complete online OH304 Laser Safety Training.
2. Read and fully understand the SOP.

3. Receive hands-on training on the High Pressure Raman Spectroscopy Experiment by an authorized user.

Unauthorized Personnel: No unauthorized personnel may enter ASE 5.118 during laser operation unless accompanied by an authorized user. All visitors must be briefed on proper safety protocol and must wear appropriate laser protective eyewear located on the premises.

Pandemic Considerations: Due to pandemic response, all personnel entering the lab must follow latest guidelines from The University of Texas at Austin for safely conducting research on campus. Personnel must read and fully understand the Research Restart Plan outlined by the Office of the Vice President for Research and monitor for updates. As an added safety measure, ASE 5.118 will be designated single occupancy when running the high pressure experiment because one cannot maintain adequate social distance in the control room when the chamber is pressurized.

B.3 Hazards

B.3.1 Laser

The Nd:YAG laser is a Class 4 laser. Severe eye damage (including blindness) and skin damage can result from direct beam and specular reflections. Eye damage can also result from diffuse reflections.

B.3.2 Electrical

Electrical shock or electrocution could result from direct contact with high voltage.

B.3.3 Pressure

Several hazards are associated with pressure with the common primary hazard being high pressure contained in the cylinder. Caution is needed to ensure that systems and apparatus used with compressed gas cylinders are not over-pressurized, which could lead to forceful rupture and flying fragments.

B.4 Hazard Controls

B.4.1 Laser

1. Only authorized personnel will operate lasers.
2. The laboratory doors will be closed, locked, and "Laser In Use" warning light will be illuminated.
3. Unauthorized personnel will be only allowed entry to the laboratory during laser operation with the supervision of an authorized user under the terms specified in Section B.2.
4. Laser eye protection (LEP) for sufficient protection against 532 nm is available and is located on the optical table nearest the lab entrance. Laser eye protection is required to be worn for all beam alignments/beam manipulations or anytime there is an open beam that exceeds the maximum permissible value. NOTE: LEP is wavelength specific and proper selection is critical.
5. Specular and diffuse reflections will be controlled using beam stops, beam barriers, beam housings and enclosures. All these control methods must be in place during normal operation.

6. No jewelry or other reflective materials are to be worn while working with the laser, especially on the hands and neck.
7. Personnel in the laser lab should avoid bending over, sitting, or otherwise putting their eyes at the level of the beam path while the laser is in operation.
8. Perform physical surveys to determine if there are stray beams specular or diffuse emanating from each laser and its optics, and then document the beam surveys noting the location of stray beams and the measures taken to control them.
9. If the beam path must be changed significantly by relocating the laser or optics, all users must be notified of the change.
10. The same precautions that are taken for safe operation of the laser must also be followed when adjusting any of the optics in use with the apparatus.
11. When a new principal researcher/experimenter takes over use of the laser system, the new user must conduct a survey for unwanted stray or diffuse beams. Appropriate tools such as IR sensitive cards or IR viewer shall be used for locating the possibility of IR light.
12. Experimental end stations should be treated the same as the laser system with regards to the preceding safety procedures.

B.4.2 Electrical

1. Enclosures for protection against the high voltages of the laser power supply or laser head should never be removed unless by an authorized service technician

or strictly following the safety procedures outlined in the safety and operations manual provided by the manufacturer.

2. Only qualified personnel may perform all internal maintenance to the laser.
3. Every portion of the electrical system, including the printed circuit cards, should be assumed to be at dangerous voltage level.

B.4.3 Pressure

1. Understand the dangers of pressurized systems; physical and health hazards of the particular gas in use, and proper installation, specifications, and use of fittings, valves, regulators, and other ancillary equipment. Use only equipment and apparatus that are designed for use in pressurized conditions and that are rated for the approximate maximum pressure, and designed for the specific gas in use.
2. Do not use a compressed gas cylinder unless the cylinder is clearly marked or labeled with the cylinder's content. Never rely on the color of the cylinder to identify its contents.
3. Do not remove the cylinder valve cap until the cylinder has been secured at the point of use. Securing means to use a rack, cage, strap or chain securely affixed to an immovable object. If a strap or chain is used it should be positioned above the midpoint but below the shoulder of the cylinder.
4. Replace valve caps when cylinders are not in use or before moving.
5. All compressed gas cylinders must be used with a regulator that is designed for

the gas and pressures involved. Two stage regulators are generally recommended for laboratory operations.

6. Always close the cylinder valve of an apparently empty cylinder before disconnecting the regulator; and when the cylinder is not in use. Do not leave pressure on the regulator when the cylinder is not in use.
7. Safely vent compressed gases to a dedicated fume exhaust or snorkel.
8. Perform hydrostatic pressure test of pressure chamber at 1.5x the maximum operating pressure of the experiment.
 - (a) Maximum Operating Pressure: 1000 psi
 - (b) Hydrostatic Test Pressure: 1500 psi
9. Pressure relief valve (PRV) place in the system set below the lowest rated pressure of all system components including pressure chamber, sight windows, tubing, valves, etc.
 - (a) PRV Set Pressure: 1250 psi

B.5 Normal Operation

1. Turn on exterior "Laser In Use" warning light and ensure laboratory doors are closed.
2. Close laser shield curtains.
3. Plug in the pressure transducer and thermocouple. Verify that both are working properly and reading room conditions.

4. Plug in the lab security cameras, internal lab router, and network switch.
5. Connect to the video feed from the lab security cameras from within the interior control room and verify that the video feed is working properly. Reset the cameras if the feed is lagging.
6. Plug in the solenoid valves.
7. Plug in the valve control panels in the interior control room.
8. Open the pilot line air cylinder that provides compressed gas to the pneumatically actuated valves and set the regulator to a pressure of approximately 75 psi. Do not exceed a pressure of 125 psi on this regulator.
9. Cycle all control valves from the interior control room. Energizing solenoid valves on fill lines should produce an audible "click" and de-energizing the solenoid control valve on the pneumatic pilot line should produce an audible "whoosh" of the air being released from the pneumatically actuated valve exit line. This verifies that valve control is working properly.
10. Verify that the exhaust snorkel is centered above the termination of the pressure chamber exit line. Also verify that the exhaust snorkel is fully open.
11. Fully close needle valves on pressure chamber fill lines (qty 2) and exit line (qty 1). Do not overtighten or the valve seat will be damaged. Then re-open each valve by 1/8 turn. All needle valves should be minimally open.
12. Uncover all the optics and check that all optics appear to be in the proper position and dust-free. Also verify that laser shields are in place.

13. Ensure overhead room lights are turned off; turn on and connect to intensified camera. From this step utilize flashlight to maneuver around experiment.
14. Turn on the laser power control unit. This starts the laser cooling water pump.
15. Check that the chamber pressure exit valve is set to the open position (solenoid power off).
16. Open the test gas cylinders. Set the test gas cylinder regulators to the desired experiment chamber pressure. This will pressurize the fill line up to the solenoid valves but will not pressurize the chamber.
17. Turn on the laser flash lamp, Q switch, and open the laser shutter.
18. Enter the interior control room and fully close the door. Do not leave this room if there is any pressurized gas in the pressure chamber.
19. Open a phone line to a designated individual, not present in the lab, who can be alert to an emergency or incapacitation of the authorized user present in the lab during the filling of the chamber. The designated individual will be Dr. Varghese.
20. Open (Energize) the solenoid control valve on the pilot line of the pressure chamber exit line normally-open, pneumatically actuated control valve. Resulting pilot line pressure will close the exit line valve.
21. Fill the pressure chamber by opening (energizing) one or both solenoid control valves on the required fill lines. After conditions in the pressure chamber have equilibrated, close (de-energize) the fill line valves.

22. Close the phone line when the chamber has been safely filled.
23. Collect the experimental data.
24. Empty the pressure chamber of all pressurized gas before leaving the interior control room.
25. Close the test gas cylinders.
26. Re-Enter the interior control room and fully close the door. Vent the gas in the pressure chamber fill lines by keeping the chamber exit line valve in the open position (solenoid control valve on pilot line de-energized) and opening the fill line solenoid control valves. Wait until fill lines are fully vented and the pressure chamber returns to room conditions. Close (de-energize) fill line solenoid control valves.
27. Close the laser shutter and turn off the laser Q switch and flash lamps.
28. Turn off the intensified camera and turn on the room lights.
29. Close the pilot line air cylinder. Empty the remaining compressed air in the pilot line by opening the ball valve release. Close the ball valve release when line has been vented.
30. Close all gas bottle regulators.
31. Turn off the laser power control unit, which turns off the laser cooling water pump. It is important to not do this immediately after the laser Q switch and flash lamps have been turned off, so that the laser head has had time to cool with the cooling water still running. Generally advisable to wait approximately

15 minutes to allow the laser to cool before turning off the laser power control unit.

32. Cover all the optics.
33. Unplug the solenoid valves.
34. Unplug the valve control panels in the interior control room.
35. Unplug the lab security cameras, internal lab router, and network switch.
36. Unplug the pressure transducer and thermocouple.
37. Open the laser shield curtains and turn off the exterior "Laser In Use" warning light.

References

- [1] Long, D. A., *The Raman Effect: A Unified Treatment of the Theory of Raman Scattering by Molecules*. Chichester, UK: John Wiley & Sons, 2002.
- [2] Linne, M. A., *Spectroscopic Measurement*. Academic Press, 2002.
- [3] Hill, P. and Peterson, C., *Mechanics and Thermodynamics of Propulsion*, 2nd. Pearson, 1992.
- [4] Bathie, W. W., *Fundamentals of Gas Turbines*, 2nd. John Wiley & Sons, 1996.
- [5] Saravanamuttoo, H. I. H., Rogers, G. F. C., Cohen, H., Straznicky, P. V., and Nix, A. C., *Gas Turbine Theory*, 7th. Pearson, 2017.
- [6] Han, J.-C., “Fundamental gas turbine heat transfer,” *Journal of Thermal Science and Engineering Applications*, vol. 5, no. 2, pp. 021007–1, 2013. DOI: 10.1115/1.4023826.
- [7] Eckert, E. R. G., “Analysis of film cooling and full-coverage film cooling of gas turbine blades,” *Journal of Engineering for Gas Turbines and Power*, vol. 106, no. 1, pp. 206–213, 1984. DOI: 10.1115/1.3239536.
- [8] Bogard, D. G. and Thole, K. A., “Gas turbine film cooling,” *Journal of Propulsion and Power*, vol. 22, no. 2, 2006. DOI: 10.2514/1.18034.
- [9] Sunden, B. and Xie, G., “Gas turbine blade tip heat transfer and cooling: A literature survey,” *Heat Transfer Engineering*, vol. 31, no. 7, pp. 527–554, 2010. DOI: 10.1080/01457630903425320.
- [10] Colban, W. F., Thole, K. A., and Zess, G., “Combustor turbine interface studies — part 1: Endwall effectiveness measurements,” *Journal of Turbomachinery*, vol. 125, no. 2, pp. 193–202, 2003. DOI: 10.1115/1.1561811.
- [11] Colban, W. F., Lethander, A. T., Thole, K. A., and Zess, G., “Combustor turbine interface studies — part 2: Flow and thermal field measurements,” *Journal of Turbomachinery*, vol. 125, no. 2, pp. 203–209, 2003. DOI: 10.1115/1.1561812.
- [12] Kerr, C. and Ivey, P., “An overview of the measurement errors associated with gas turbine aeroengine pyrometer systems,” *Measurement Science and Technology*, vol. 13, no. 6, pp. 873–881, 2002. DOI: 10.1088/0957-0233/13/6/307.
- [13] Han, J.-C. and Rallabandi, A. P., “Turbine blade film cooling using PSP technique,” *Frontiers in Heat and Mass Transfer*, vol. 1, p. 013001, 2010. DOI: 10.5098/hmt.v1.1.3001.

- [14] Shiau, C.-C., Chen, A. F., Han, J.-C., Azad, S., and Lee, C.-P., “Full-scale turbine vane endwall film-cooling effectiveness distribution using pressure-sensitive paint technique,” *Journal of Turbomachinery*, vol. 138, no. 5, p. 051002, 2016. DOI: 10.1115/1.4032166.
- [15] Wang, G., Bonilla, C., and Kalitan, D., “Gas temperature field measurement using thin-filament pyrometry,” *Proceedings of ASME Turbo Expo 2014*, ser. GT2014-25909, 2014. DOI: 10.1115/GT2014-25909.
- [16] Ma, B., Wang, G., Magnotti, G., Barlow, R. S., and Long, M. B., “Intensity-ratio and color-ratio thin-filament pyrometry: Uncertainties and accuracy,” *Combustion and Flame*, vol. 161, no. 4, pp. 908–918, 2014. DOI: 10.1016/j.combustflame.2013.10.014.
- [17] Eckbreth, A., *Laser Diagnostics for Combustion Temperature and Species*, 2nd. Kent, UK: Gordon and Breach Publishers, 1988.
- [18] Bolshov, M. A., Kuritsyn, Y. A., and Romanovskii, Y. V., “Tunable diode laser spectroscopy as a technique for combustion diagnostics,” *Spectrochimica Acta Part B*, vol. 106, pp. 45–66, 2015. DOI: 10.1016/j.sab.2015.01.010.
- [19] Cai, W. and Kaminski, C. F., “Tomographic absorption spectroscopy for the study of gas dynamics and reactive flows,” *Progress in Energy and Combustion Science*, vol. 59, pp. 1–31, 2017. DOI: 10.1016/j.pecs.2016.11.002.
- [20] Goldenstein, C. S., Spearrin, R. M., Jeffries, J. B., and Hanson, R. K., “Infrared laser-absorption sensing for combustion gases,” *Progress in Energy and Combustion Science*, vol. 60, pp. 132–176, 2017. DOI: 10.1016/j.pecs.2016.12.002.
- [21] Seitzman, J. M., Hanson, R. K., DeBarber, P. A., and Hess, C. F., “Application of quantitative two-line OH planar laser-induced fluorescence for temporally resolved planar thermometry in reacting flows,” *Applied Optics*, vol. 33, no. 18, pp. 4000–4012, 1994. DOI: 10.1364/AO.33.004000.
- [22] Daily, J. W., “Laser induced fluorescence spectroscopy in flames,” *Progress in Energy and Combustion Science*, vol. 23, no. 2, pp. 133–199, 1997. DOI: 10.1016/S0360-1285(97)00008-7.
- [23] Thurber, M. C. and Hanson, R. K., “Simultaneous imaging of temperature and mole fraction using acetone planar laser-induced fluorescence,” *Experiments in Fluids*, vol. 30, pp. 93–101, 2001. DOI: 10.1007/s003480000142.
- [24] Omrane, A., Petersson, P., Aldén, M., and Linne, M. A., “Simultaneous 2D flow velocity and gas temperature measurements using thermographic phosphors,” *Applied Physics B*, vol. 92, no. 1, pp. 99–102, 2008. DOI: 10.1007/s00340-008-3051-1.
- [25] Abram, C., Fond, B., and Beyrau, F., “Temperature measurement techniques for gas and liquid flows using thermographic phosphor tracer particles,” *Progress in Energy and Combustion Science*, vol. 64, pp. 93–156, 2018. DOI: 10.1016/j.pecs.2017.09.001.

- [26] Witkowski, D. and Rothamer, D. A., “Scattering referenced aerosol phosphor thermometry,” *Measurement Science and Technology*, vol. 30, no. 4, p. 044003, 2019. DOI: 10.1088/1361-6501/ab04cb.
- [27] Miles, R. B., Lempert, W. R., and Forkey, J. N., “Laser Rayleigh scattering,” *Measurement Science and Technology*, vol. 12, no. 5, R33–R51, 2001. DOI: 10.1088/0957-0233/12/5/201.
- [28] Wang, G.-H., Clemens, N. T., Varghese, P. L., and Barlow, R. S., “Turbulent time scales in a nonpremixed turbulent jet flame by using high-repetition rate thermometry,” *Combustion and Flame*, vol. 152, no. 3, pp. 317–335, 2008. DOI: 10.1016/j.combustflame.2007.08.010.
- [29] Barlow, R. S., Wang, G.-H., Anselmo-Filho, P., Sweeney, M. S., and Hochgreb, S., “Application of Raman/Rayleigh/LIF diagnostics in turbulent stratified flames,” *Proceedings of the Combustion Institute*, vol. 32, no. 1, pp. 945–953, 2009. DOI: 10.1016/j.proci.2008.06.070.
- [30] Papageorge, M. J., McManus, T. A., Fuest, F., and Sutton, J. A., “Recent advances in high-speed planar Rayleigh scattering in turbulent jets and flames: Increased record lengths, acquisition rates, and image quality,” *Applied Physics B*, vol. 115, pp. 197–213, 2014. DOI: 10.1007/s00340-013-5591-2.
- [31] Reising, H. H., KC, U., Clemens, N. T., and Varghese, P. L., “Measurement of mixing-induced thermal non-equilibrium in a supersonic shear layer using spontaneous Raman scattering,” *Physics of Fluids*, vol. 29, no. 7, p. 07601, 2017. DOI: 10.1063/1.4991754.
- [32] Kojima, J. and Nguyen, Q.-V., “Single-shot rotational Raman thermometry for turbulent flames using a low-resolution bandwidth technique,” *Measurement Science and Technology*, vol. 19, no. 1, p. 015406, 2008. DOI: 10.1088/0957-0233/19/1/015406.
- [33] Eckbreth, A. C. and Hall, R. J., “CARS thermometry in a sooting flame,” *Combustion and Flame*, vol. 36, pp. 87–98, 1979. DOI: 10.1016/0010-2180(79)90048-8.
- [34] Bengtsson, P.-E., Martinsson, L., Aldén, M., and Kröll, S., “Rotational CARS thermometry in sooting flames,” *Combustion Science and Technology*, vol. 81, no. 1-3, pp. 129–140, 1992. DOI: 10.1080/00102209208951797.
- [35] Kearney, S. P., Frederickson, K., and Grasser, T. W., “Dual-pump coherent anti-Stokes Raman scattering thermometry in a sooting turbulent pool fire,” *Proceedings of the Combustion Institute*, vol. 32, no. 1, pp. 871–878, 2009. DOI: 10.1016/j.proci.2008.06.148.
- [36] Roy, S., Gord, J. R., and Patnaik, A. K., “Recent advances in coherent anti-Stokes Raman scattering spectroscopy: Fundamental developments and applications in reacting flows,” *Progress in Energy and Combustion Science*, vol. 36, no. 2, pp. 280–306, 2010. DOI: 10.1016/j.pecs.2009.11.001.

- [37] Klierer, C. J., Gao, Y., Seeger, T., Kiefer, J., Patterson, B. D., and Settersten, T. B., “Picosecond time-resolved pure-rotational coherent anti-Stokes Raman spectroscopy in sooting flames,” *Proceedings of the Combustion Institute*, vol. 33, no. 1, pp. 831–838, 2011. DOI: 10.1016/j.proci.2010.05.067.
- [38] Kearney, S. P., “Hybrid fs/ps rotational CARS temperature and oxygen measurements in the product gases of canonical flat flames,” *Combustion and Flame*, vol. 162, no. 5, 1748–1758, 2015. DOI: 10.1016/j.combustflame.2014.11.036.
- [39] Miller, J. D., Slipchenko, M. N., Mance, J. G., Roy, S., and Gord, J. R., “1-kHz two-dimensional coherent anti-Stokes Raman scattering (2D-CARS) for gas-phase thermometry,” *Optical Express*, vol. 24, no. 22, pp. 24 971–24 979, 2016. DOI: 10.1364/OE.24.024971.
- [40] Richardson, D., Roy, S., Gord, J., and Kearney, S. P., “Two-beam femtosecond rotational CARS for one-dimensional thermometry in a turbulent, sooting jet flame,” *55th AIAA Aerospace Sciences Meeting*, 2017. DOI: 10.2514/6.2017-0031.
- [41] Kojima, J. and Nguyen, Q.-V., “Measurement and simulation of spontaneous Raman scattering in high-pressure fuel-rich H₂-air flames,” *Measurement Science and Technology*, vol. 15, no. 3, pp. 565–580, 2004. DOI: 10.1088/0957-0233/15/3/009.
- [42] Duan, X. R., Meier, W., Weigand, P., and Lehmann, B., “Phase-resolved laser Raman scattering and laser Doppler velocimetry applied to periodic instabilities in a gas turbine model combustor,” *Applied Physics B*, vol. 80, 389–396, 2005. DOI: 10.1007/s00340-004-1722-0.
- [43] Wehr, L., Meier, W., Kutne, P., and Hassa, C., “Single-pulse 1D laser Raman scattering applied in a gas turbine model combustor at elevated pressure,” *Proceedings of the Combustion Institute*, vol. 31, no. 2, pp. 3099–3106, 2007. DOI: 10.1016/j.proci.2006.07.148.
- [44] Meier, W., Weigand, P., Duan, X. R., and Giezendanner-Thoben, R., “Detailed characterization of the dynamics of thermoacoustic pulsations in a lean premixed swirl flame,” *Combustion and Flame*, vol. 150, no. 1-2, pp. 2–26, 2007. DOI: 10.1016/j.combustflame.2007.04.002.
- [45] Thariyan, M. P., Bhuiyan, A. H., Meyer, S. E., Naik, S. V., Gore, J. P., and Lucht, R. P., “Dual-pump coherent anti-Stokes Raman scattering system for temperature and species measurements in an optically accessible high-pressure gas turbine combustor facility,” *Measurement Science and Technology*, vol. 22, no. 1, p. 015301, 2011. DOI: 10.1088/0957-0233/22/1/015301.
- [46] Boxx, I., Arndt, C., Carter, C. D., and Meier, W., “High-speed laser diagnostics for the study of flame dynamics in a lean premixed gas turbine model combustor,” *Experiments in Fluids*, vol. 52, 555–567, 2012. DOI: 10.1007/s00348-010-1022-x.

- [47] Stopper, U., Meier, W., Sadanandan, R., Stöhr, M., Aigner, M., and Bulat, G., “Experimental study of industrial gas turbine flames including quantification of pressure influence on flow field, fuel/air premixing and flame shape,” *Combustion and Flame*, vol. 160, no. 10, pp. 2103–2118, 2013. DOI: 10.1016/j.combustflame.2013.04.005.
- [48] Arndt, C. M., Severin, M., Dem, C., Stöhr, M., Steinberg, A. M., and Meier, W., “Experimental analysis of thermo-acoustic instabilities in a generic gas turbine combustor by phase-correlated PIV, chemiluminescence, and laser Raman scattering measurements,” *Experiments in Fluids*, vol. 56, p. 69, 2015. DOI: 10.1007/s00348-015-1929-3.
- [49] Scherman, M., Santagata, R., Faleni, J. P., Bresson, M. O. A., Attal-tretout, B., and Krumme, A., “Spontaneous rotational Raman thermometry for air flow characterization in a turbomachine test rig,” *Journal of Raman Spectroscopy*, vol. 50, no. 9, pp. 1276–1282, 2019. DOI: 10.1002/jrs.5712.
- [50] Hartmann, J.-M., Boulet, C., and Robert, D., *Collisional Effects on Molecular Spectra*. Elsevier B.V., 2008.
- [51] KC, U. and Varghese, P. L., “Accurate temperature measurements in flames with high spatial resolution using Stokes Raman scattering from nitrogen in a multiple-pass cell,” *Applied Optics*, vol. 52, no. 20, pp. 5007–5021, 2013. DOI: 10.1364/AO.52.005007.
- [52] Reising, H. H., “Application of spontaneous Raman scattering for measurements of thermal non-equilibrium in high-speed mixing and combustion,” Ph.D. dissertation, The University of Texas at Austin, 2017.
- [53] Winters, C., Kearney, S., Wagner, J., Haller, T., and Varghese, P., “Burst-mode spontaneous Raman thermometry in a flat flame,” *AIAA Scitech Forum*, ser. 2020-0518, 2020. DOI: 10.2514/6.2020-0518.
- [54] Winters, C., Haller, T., Kearney, S., Varghese, P., Lynch, K., Daniel, K., and Wagner, J., “Pulse-burst spontaneous Raman thermometry of unsteady wave phenomena in a shock tube,” *Optics Letters*, vol. 46, no. 9, pp. 2160–2163, 2021. DOI: 10.1364/OL.420484.
- [55] Jiang, N., Hsu, P. S., Mance, J. G., Wu, Y., Gragston, M., Zhang, Z., Miller, J. D., Gord, J. R., and Roy, S., “High-speed 2D Raman imaging at elevated pressures,” *Optics Letters*, vol. 42, no. 18, pp. 3678–3681, 2017. DOI: 10.1364/OL.42.003678.
- [56] May, A. D., Stryland, J. C., and Varghese, G., “Collisional narrowing of the vibrational Raman band of nitrogen and carbon monoxide,” *Canadian Journal of Physics*, vol. 48, no. 19, pp. 2331–2335, 1970. DOI: 10.1139/p70-290.

- [57] Gu, Y., Zhou, Y., Tang, H., Rothe, E. W., and Reck, G. P., "Pressure dependence of vibrational Raman scattering of narrow-band 248-nm, laser light by H_2 , N_2 , O_2 , CO_2 , CH_4 , C_2H_6 , and C_3H_8 as high as 97 bar," *Applied Physics B*, vol. 71, no. 6, pp. 865–871, 2000. DOI: 10.1007/s003400000412.
- [58] Lavorel, B., Oksengor, B., Fabre, D., Saint-Loup, R., and Berger, H., "Stimulated Raman spectroscopy of the Q branch of nitrogen at high pressure: Collisional narrowing and shifting in the 150-6800 bar range at room temperature," *Molecular Physics*, vol. 75, no. 2, pp. 397–413, 1992. DOI: 10.1080/00268979200100311.
- [59] Millot, G., Roche, C., Saint-Loup, R., Chaux, R., Berger, H., and Santos, J., "Collisional narrowing and shifting in the Raman Q-branch of oxygen at high density," *Chemical Physics*, vol. 173, no. 3, pp. 505–512, 1993. DOI: 10.1016/0301-0104(93)80164-5.
- [60] Millot, G., Lavorel, B., and Fanjoux, G., "Pressure broadening, shift, and interference effect for a multiplet line in the rovibrational anisotropic stimulated Raman spectrum of molecular oxygen," *Journal of Molecular Spectroscopy*, vol. 176, no. 1, pp. 211–218, 1996. DOI: 10.1006/jmsp.1996.0078.
- [61] Koszykowski, M. L., Rahn, L. A., Palmer, R. E., and Coltrin, M. E., "Theoretical and experimental studies of high-resolution inverse Raman spectra of N_2 at 1-10 atm," *The Journal of Physical Chemistry*, vol. 91, no. 1, pp. 41–46, 1987. DOI: 10.1021/j100285a012.
- [62] Dreier, T., Schiff, G., and Suvernev, A. A., "Collisional effects in Q branch coherent anti-Stokes Raman spectra of N_2 and O_2 at high pressure and high temperature," *The Journal of Chemical Physics*, vol. 100, no. 9, pp. 6275–6289, 1994. DOI: 10.1063/1.467090.
- [63] Rolland, P., Pouligny, B., Morin, E., Menil, A., and Dejean, J. P., "High resolution CARS spectroscopy of molecular nitrogen up to 1000 bar," *Molecular Physics*, vol. 81, no. 1, pp. 31–42, 1994. DOI: 10.1080/00268979400100031.
- [64] Ridder, M., Suvernev, A. A., and Dreier, T., "Collision effects in nitrogen and methane coherent anti-Stokes Raman isotropic Q-branch spectra at high densities," *The Journal of Chemical Physics*, vol. 105, no. 9, pp. 3376–3386, 1996. DOI: 10.1063/1.472223.
- [65] Koszykowski, M. L., Farrow, R. L., and Palmer, R. E., "Calculation of collisionally narrowed coherent anti-Stokes Raman spectroscopy spectra," *Optics Letters*, vol. 10, no. 10, pp. 479–480, 1985. DOI: 10.1364/OL.10.000478.
- [66] Rahn, L. A. and Palmer, R. E., "Studies of nitrogen self-broadening at high temperature with inverse Raman spectroscopy," *Journal of the Optical Society of America B*, vol. 3, no. 9, pp. 1164–1169, 1986. DOI: 10.1364/JOSAB.3.001164.

- [67] Farrow, R. L., Trebino, R., and Palmer, R. E., “High-resolution CARS measurements of temperature profiles and pressure in a tungsten lamp,” *Applied Optics*, vol. 26, no. 2, pp. 331–335, 1987. DOI: 10.1364/AO.26.000331.
- [68] Lavorel, B., Guillot, L., Bonamy, J., and Robert, D., “Collisional Raman linewidths of nitrogen at high temperature (1700-2400 K),” *Optics Letters*, vol. 20, no. 10, pp. 1189–1191, 1995. DOI: 10.1364/OL.20.001189.
- [69] Buldyreva, J. V. and Bonamy, L., “Non-markovian energy-corrected sudden model for the rototranslational spectrum of N₂,” *Physical Review A*, vol. 60, no. 1, pp. 370–376, 1999. DOI: 10.1103/PhysRevA.60.370.
- [70] Bonamy, L. and Buldyreva, J. V., “Non-Markovian far-wing rotational Raman spectrum from translational modeling,” *Physical Review A*, vol. 63, no. 1, p. 012715, 2000. DOI: 10.1103/PhysRevA.63.012715.
- [71] Buldyreva, J., Racht, F., and Chrysos, M., “Nitrogen isotropic Raman Q-branch profile in an extended frequency range,” *Physical Review A*, vol. 64, no. 5, p. 052708, 2001. DOI: 10.1103/PhysRevA.64.052708.
- [72] Gordon, R. G., “Molecular Motion in Infrared and Raman Spectra,” *The Journal of Chemical Physics*, vol. 43, no. 4, pp. 1307–1312, 1965. DOI: 10.1063/1.1696920.
- [73] Gordon, R. G., “Semiclassical Theory of Spectra and Relaxation in Molecular Gases,” *The Journal of Chemical Physics*, vol. 45, no. 5, pp. 1649–1655, 1966. DOI: 10.1063/1.1727808.
- [74] Bonamy, L., Bonamy, J., Robert, D., Temkin, S., Millot, G., and Lavorel, B., “Line coupling in anisotropic Raman branches,” *The Journal of Chemical Physics*, vol. 101, no. 9, pp. 7350–7356, 1994. DOI: 10.1063/1.468293.
- [75] Reising, H. H., Haller, T. W., Clemens, N. T., Varghese, P. L., Fiévet, R., and Raman, V., “Spontaneous Raman scattering temperature measurements and large eddy simulations of vibrational non-equilibrium in high-speed jet flames,” *32nd AIAA Aerodynamic Measurement Technology and Ground Testing Conference*, ser. 2016-3550, 2016. DOI: 10.2514/6.2016-3550.
- [76] Martinsson, L., Bengtsson, P.-E., Aldén, M., Kröll, S., and Bonamy, J., “A test of different rotational raman linewidths models: Accuracy of rotational coherent anti-Stokes Raman scattering thermometry in nitrogen from 295 to 1850 K,” *The Journal of Chemical Physics*, vol. 99, no. 4, pp. 2466–2477, 1993. DOI: 10.1063/1.466197.
- [77] Miller, J. D., Roy, S., Gord, J. R., and Meyer, T. R., “Communication: Time-domain measurement of high-pressure N₂ and O₂ self-broadened linewidths using hybrid femtosecond/picosecond coherent anti-Stokes Raman scattering,” *The Journal of Chemical Physics*, vol. 135, no. 20, p. 201014, 2011. DOI: 10.1063/1.3665932.

- [78] KC, U., “Development of a multiple-pass Raman spectrometer for flame diagnostics,” Ph.D. dissertation, The University of Texas at Austin, 2013.
- [79] Buldakov, M. A., Cherepanov, V. N., Korolev, B. V., and Matrosov, I. I., “Role of intramolecular interactions in Raman spectra of N₂ and O₂ molecules,” *Journal of Molecular Spectroscopy*, vol. 217, no. 1, pp. 1–8, 2003. DOI: 10.1016/S0022-2852(02)00012-7.
- [80] Buldakov, M. A., Ippolitov, I. I., Korolev, B. V., Matrosov, I. I., Cheglov, A. E., Cherepanov, V. N., Makushkin, Y. S., and Ulenikov, O. N., “Vibration rotation Raman spectroscopy of gas media,” *Spectrochimica Acta Part A: Molecular and Biomolecular Spectroscopy*, vol. 52, no. 8, pp. 995–1007, 1996. DOI: 10.1016/0584-8539(95)01631-7.
- [81] Laher, R. R. and Gilmore, F. R., “Improved fits for the vibrational and rotational constants of many states of nitrogen and oxygen,” *Journal of Physical and Chemical Reference Data*, vol. 20, no. 4, pp. 685–712, 1991. DOI: 10.1063/1.555892.
- [82] Bendtsen, J., “High-resolution Fourier transform Raman spectra of the fundamental bands of ¹⁴N¹⁵N and ¹⁵N₂,” *Journal of Raman Spectroscopy*, vol. 32, no. 12, pp. 989–995, 2001. DOI: 10.1002/jrs.785.
- [83] Herzberg, G., *Molecular Spectra and Molecular Structure I. Spectra of Diatomic Molecules*, 2nd. D. Van Nostrand Company, 1950.
- [84] Reising, H. H., KC, U., Voelkel, S., Clemens, N. T., Raman, V., Varghese, P. L., and Koo, H., “Vibrational non-equilibrium effects in supersonic jet mixing,” *52nd AIAA Aerospace Sciences Meeting*, ser. 2014-0231, 2014. DOI: 10.2514/6.2014-0231.
- [85] Gordon, R. G. and McGinnis, R. P., “Line shapes in molecular spectra,” *The Journal of Chemical Physics*, vol. 49, no. 5, pp. 2455–2456, 1968. DOI: 10.1063/1.1670429.
- [86] Gordon, R. G. and McGinnis, R. P., “Intermolecular potentials and infrared spectra,” *The Journal of Chemical Physics*, vol. 55, no. 10, pp. 4898–4906, 1971. DOI: 10.1063/1.1675597.
- [87] Haller, T. W., Reising, H. H., Clemens, N. T., and Varghese, P. L., “High-pressure spontaneous Raman scattering based temperature measurements,” *33rd AIAA Aerodynamic Measurement Technology and Ground Testing Conference*, ser. 2017-3898, 2017. DOI: 10.2514/6.2017-3898.
- [88] Ranjan, R., “Flame-flow interaction during premixed and stratified swirl flame flashback in an annular swirl combustor,” Ph.D. dissertation, The University of Texas at Austin, 2018.

- [89] Driscoll, J. J., Sick, V., Schrader, P. E., and Farrow, R. L., “Measurements of NO distributions and fluorescence lifetimes in a non-premixed counterflow CH₄/air flame using picosecond time-resolved laser-induced fluorescence,” *Proceedings of the Combustion Institute*, vol. 29, no. 2, pp. 2719–2726, 2002. DOI: 10.1016/S1540-7489(02)80331-5.
- [90] Haller, T. W. and Varghese, P. L., “Measurements of pressure broadening of N₂ in the anisotropic tensor component of spontaneous Raman spectra,” *Combustion and Flame*, vol. 224, pp. 166–176, 2021. DOI: 10.1016/j.combustflame.2020.11.045.
- [91] Dunn, P. F., *Measurement and Data Analysis for Engineering and Science*, 2nd. Boca Raton, FL, US: CRC Press, Taylor and Francis Group, 2010.
- [92] Varghese, P. L. and Hanson, R. K., “Tunable infrared diode laser measurements of line strengths and collision widths of ¹²C¹⁶O at room temperature,” *Journal of Quantitative Spectroscopy and Radiative Transfer*, vol. 24, no. 6, pp. 479–489, 1980. DOI: 10.1016/0022-4073(80)90017-5.
- [93] Varghese, P. L. and Hanson, R. K., “Tunable infrared diode laser measurements of spectral parameters of HCN at room temperature,” *Journal of Quantitative Spectroscopy and Radiative Transfer*, vol. 31, no. 6, pp. 545–559, 1984. DOI: 10.1016/0022-4073(84)90060-8.
- [94] Kliewer, C. J., Bohlin, A., Nordström, E., Patterson, B. D., Bengtsson, P.-E., and Settersten, T. B., “Time-domain measurements of S-branch N₂-N₂ Raman linewidths using picosecond pure rotational coherent anti-Stokes Raman spectroscopy,” *Applied Physics B*, vol. 108, no. 2, pp. 419–426, 2012. DOI: 10.1007/s00340-012-5037-2.
- [95] Bonamy, J., Robert, D., Harmann, J. M., Gonze, M. L., Saint-Loup, R., and Berger, H., “Line broadening, line shifting, and line coupling effects on N₂-H₂O stimulated Raman spectra,” *The Journal of Chemical Physics*, vol. 91, no. 10, pp. 5916–5925, 1989. DOI: 10.1063/1.457461.
- [96] Bonamy, J., Bonamy, L., Robert, D., Gonze, M. L., Millot, G., Lavorel, B., and Berger, H., “Rotational relaxation of nitrogen in ternary mixtures N₂-CO₂-H₂O: Consequences in coherent anti-Stokes Raman spectroscopy thermometry,” *The Journal of Chemical Physics*, vol. 94, no. 10, pp. 6584–6589, 1991. DOI: 10.1063/1.460285.